2010-ENAM-0046

École doctorale n° 432 : Sciences des Métiers de l'Ingénieur

Doctorat ParisTech

T H È S E

pour obtenir le grade de docteur délivré par

l'École Nationale Supérieure d'Arts et Métiers

Spécialité " Mécanique - Matériaux "

présentée et soutenue publiquement par

Camilo Andrés CRUZ BERNAL

le 03 Décembre 2010

Modelling of Rheological Properties of Carbon Nanotube Suspensions

Directeur de thèse : **Gilles REGNIER**
Co-encadrement de la thèse : **Francisco CHINESTA**

Jury

M. Philippe CASSAGNAU, Professeur, CNRS-INSA-UCB, Université Lyon 1	Président
M. Malcolm MACKLEY, Professeur, Dept. of Chemical Engineering, University of Cambridge	Rapporteur
M. Roland KEUNINGS, Professeur, ICTEAM, Université Catholique de Louvain	Rapporteur
M. Jorge MEDINA, Professeur, Dept. Ingeniería Mecánica, Universidad de los Andes	Examinateur
M. Francisco CHINESTA, Professeur, EADS Corp. Inter. Chair, Ecole Centrale de Nantes	Examinateur
M. Gilles REGNIER, Professeur, PIMM, Arts et Métiers ParisTech	Examinateur

T H È S E

Arts et Métiers ParisTech - Centre de Paris
Laboratoire de Procédés et Ingénierie en Mécanique et Matériaux PIMM

Acknowledgements

In first place I would like to specially thank my supervisors Prof. Gilles REGNIER (Arts et Métiers ParisTech) and Prof. Francisco CHINESTA (Ecole Centrale de Nantes). I express my gratitude to Gilles for his unconditional support, enriching advices and kindly guidance. I keep with me his valuable method of reducing to the simplest concepts when tackling with complex problems. I would like to thank Paco for his continuous support, amazing dynamism and unquestionable commitment to the scientific research. Such passion constituted an endless inspiring light during all my thesis work. Gilles and Paco have exceeded their teaching functions, they are friends for me.

I am quite grateful to Dr. Anson MA (Rice University) for his kind exchange of ideas, information and advices that was absolutely important to validate the modelling carried out in my thesis. I would like to recognize his scientific excellence and the overpowering passion for research. I would like to acknowledge very specially Dr. Lounes ILLOUL (Arts et Métiers ParisTech) for the invaluable assistance that he provided me for programming the parallel computation routines. I have to say that without his help probably I would not have finished my thesis in time.

It is a deep honour for me that Prof. Malcolm MACKLEY (University of Cambridge) and Prof. Roland KEUNINGS (Université Catholique de Louvain) would have accepted to examine my dissertation. I would like also to express my gratitude to Prof. Philippe CASSAGNAU (Université de Lyon 1) and Prof. Jorge MEDINA (Universidad de Los Andes) for accepting to be members of my thesis's jury. I specially thank Prof. Jorge MEDINA because a big part of my present achievements are due to the thrust that he amiably put on me. Special thanks are addressed to Ministère de l'Enseignement Supérieur et de la Recherche and Arts et Métiers ParisTech for providing my financial support throughout the three years of doctoral studies.

I would like to say thank you to my family at PIMM: Odile, Paulo, Giovanna, Nada, Goska, Monir, Albert, Emmanuel, Bruno, Salah, Aurélie and all the rest of members of the lab that gave me plenty of reasons for coming to work. I specially thank my family at Cité Universitaire de Paris: Carolina, Clara, Mariana, Luiz and all the nice people that I crossed during my stay in Maison des Arts et Métiers, they made of last three years one of the most beautiful chapters in my life.

A huge and growing up thank you to my Little Miss Sunshine for her lovely support during the decisive stage of my thesis work. And finally an immeasurable gratitude is devoted to my parents and all my family in Colombia for their unconditional support and endless love. They are my motor and the main reason for keep walking.

Contents

Symbols and Notation

Micro-mechanical Model Parameters

n	Number of beads	
a	Rod length	
d	Diameter of rod-like slender system	
L	Contour length, $L = 2l = (n-1)a$	
l_p	Quiescent persistent length	
R	Effective aspect ratio, $R = l/d$	
M	Mass of Brownian particle; mass of bead	
ϕ	Internal-energy potential	
H	Hookean-spring constant	
K_b	Bending rigidity constant	
$\boldsymbol{\zeta}$	Bead friction tensor	
ζ	Bead friction coefficient, $\boldsymbol{\zeta} = \zeta\,\boldsymbol{\delta}$	
ς	Specific bead friction coefficient, $\zeta = M\varsigma$	
D	Diffusion coefficient, $D = k_B T/\zeta$	
c	Number of concentration	

Time Constants

λ_H	For Hookean-spring	Eq. (2.3)
λ_j	For jth mode in Rouse chain	Eq. (2.51)
$\tilde{\lambda}_j$	For jth mode in Zimm chain	Eq. (2.63)
τ_1	*Trimer*'s main relaxation time	Eq. (2.96)
λ_n	For a multi-bead rigid-rod with n beads	Eq. (2.97)
λ_{bead}	Bead diffusion time, $\lambda_{bead} = \zeta a^2/k_B T$	

Hydrodynamic Interaction

$\boldsymbol{\Omega}_{ij}$	Oseen-Burgers hydrodynamic interaction tensor	Eq. (2.18)
$\mathbf{HI}_{ij}$	Zimm hydrodynamic interaction tensor	Eq. (2.59)
h^*	Hydrodynamic interaction parameter	Eq. (2.60)

Configuration in Micro-mechanical Models

r	End-to-end distance	Eq. (2.1)
$\mathbf{r}_i$	Position of bead i with respect to origin	see §2.4.1
$\mathbf{r}_c$	Position of centre of mass	Eq. (2.14)
$\mathbf{R}_v$	Position of bead v with respect to the centre of mass	see §2.4.3

$\mathbf{Q}_i$	Connector vector between beads $i+1$ and i	Eq. (2.15)
$\tilde{\mathbf{A}}_{ij}$	Modified Rouse matrix with Eigen-values $\tilde{a}_j$	Eq. (2.64)
$\mathbf{u}_j$	Unit vector collinear with rod j	Eq. (2.66)
θ_i	Positive angle of rod i with respect the x-axis in the xy-plane	
$\Delta\theta_{i,j}$	Equilibrium internal angle between $\mathbf{u_i}$ and $\mathbf{u_j}$: $\Delta\theta^0_{i,j} = \theta^0_i - \theta^0_j$	
$\mathbf{Z}_i$	Rotation matrix in the xy-plane through an angle $-\Delta\theta^0_{i,i-1}$	

Forces

$\mathbf{F}_i^{(h)}$	Hydrodynamic drag force on bead i	Eq. (2.16)
$\mathbf{F}_j^{(c)}$	Connector force on bead j along spring j	Eq. (2.20)
$\mathbf{F}_i^{(\phi)}$	Intra-molecular force on bead i	Eqs. (2.20) and (2.70)
$\mathbf{F}_i^{(b)}$	Brownian force on bead i	Eqs. (2.25) and (2.26)
$\mathbf{F}_i^{(e)}$	Sum of external forces on bead i	
$\mathbf{F}_i^{(\lambda)}$	Constraint force on bead i	Eq. (2.67)
λ_j	Lagrange multiplier of tension on bead j along rod j	Eq. (2.67)
$\mathbf{F}_i^{(b)'}$	Geometrical-projected Brownian force on bead i	Eq. (2.77)
$\mathbf{F}_i^{(m)}$	Potential metric force on bead i	see §2.5.2

Fluid Dynamics

$\mathbf{v}$	Fluid velocity	
$\mathbf{v}'$	Variation of the velocity field due to hydrodynamic interaction	
$\boldsymbol{\kappa}$	Fluid velocity gradient, $\boldsymbol{\kappa} = \nabla\mathbf{v}$	
$\boldsymbol{\tau}$	Total shear-stress tensor	Eq. (2.39)
$\dot{\boldsymbol{\gamma}}$	Homogeneous rate-of-strain tensor, $\dot{\boldsymbol{\gamma}} = \boldsymbol{\kappa} + \boldsymbol{\kappa}^T$	
$\dot{\gamma}$	Shear rate	
ω	Angular frequency	
T	Period of a dynamic oscillation function	

Rheological Variables

η	Shear viscosity	
G'	Storage modulus	
G''	Loss modulus	
δ	Phase-angle in a dynamic-mechanical test	
$G(t)$	Relaxation modulus	

Brownian Dynamics (BD) Quantities

N	Number of micro-mechanical models in a BD system	
$\mathbf{W_t}$	Multi-dimensional Wiener Process	see §2.2.1
Δt	Length of the integration time step	
$\mathcal{D}$	Space dimensionality of the simulation	
υ	Order of convergence of the integration scheme	
ϵ	Numerical tolerance error	

Mathematical Symbols

δ_{ij}	Kronecker delta

$\boldsymbol{\delta}$	Unit tensor

Miscellaneous

T	Absolute temperature
k_B	Boltzmann constant
φ	Volume fraction

Subscripts and Superscripts

p	suspending particle; sub-section of bead-rod chain
s	solvent
eq	equilibrium state
th	theoretical reference

Introduction

Today, without any doubt nanotechnology is a hot spot in scientific research. Exponential growth of indexed scientific publications devoted to nano-science from the end of the eighties is a proof. Importance of the nanoscale in the technology can be summarized in some words of the Nobel Physics laureate (1998) Horst Störmer, who mentioned that nanoscale is the first step where we can assemble something useful. Belonging to this widespread nano-world, carbon nanotubes (CNTs) are an illustration, as well as graphene, whose discovery has recently meant the Physics Nobel Prize in 2010. In fact, a CNT is a cylindrical structure constituted essentially by rolled-up graphene sheets with diameters going from 0.4 nm to several nanometres and lengths up to some fractions of millimeter [1]. This particular structure confers to CNTs an extraordinary compromise between mechanical, thermal and electrical properties.

Pristine CNTs exhibit very strong tube-tube Van der Waals forces that produce their natural agglomeration in bundles. In consequence, solubilisation of CNTs as individual entities is difficult and remains the main obstacle to develop their industrial applications [2]. To solve this problem, chemical modification of the tube side-wall by covalent functionalization has been one of the most extended attempts to enhance the dispersion of CNTs [3].

A large range of the applications of CNTs requires a transformation processing in liquid phase. For such reason, CNTs are usually suspended into a Newtonian fluid or a viscoelastic matrix (for instance, a melted polymer). Control and optimization of those transforming processes, based on the flow of such suspensions, need a deep comprehension of their rheology [4]. On the other hand, characterisation of CNT-based suspensions, which is found very difficult due to high variety of factors determining their physical properties, is strongly supported on the rheological behaviour of those complex fluids [5]. Hence, it is imperative that rheology of CNT suspensions is deeply studied in order to have a consistent development of the CNT-based technological applications. However, it has been recently pointed out as very surprising the little development of the rheological science devoted to the CNT suspensions [6]. This thesis constitutes a contribution to close some gaps in the understanding of the physical phenomena behind the rheological behaviour exhibited by CNT suspensions.

Experimental rheology data on CNT suspensions is extensive, a large range of viscoelastic phenomena have been observed and quantified from the dilute regime to the concentrated one. Nevertheless, due to the inconsistent nature of CNTs (diversity in lengths,

diameters, chiralities, impurities, defects, surface-treatments) and the variety of factors controlling the physico-chemical interactions with a given suspending medium, rheological data of CNT suspensions are quite difficult to reproduce and, even, sometimes contradictory results can be found between different researchers [5]. Hence, research on the physical basis behind the rheological response of a CNT suspension based exclusively on experimental facts is a very difficult task. In that context, computational rheology appears as powerful tool, firstly, for filtering the increasing database on rheological characterisation of CNT suspensions and, secondly, for validating the physical hypothesis explaining the dynamic behaviour of CNT suspensions. For instance, the dynamics of an individual CNT within a suspending medium currently lacks of unified physical explanation. This work uses a Brownian dynamics (BD) approach with the purpose of elucidate the physical phanomena behind the rheological behaviour of dilute CNT suspensions.

The modelling in this thesis is applied to the shear-rheological behaviour in the linear regime of surface-treated single-walled CNTs (SWNTs) dilute suspensions within a Newtonian solvent. This framework is not restrictive; on the contrary it looks for tackling directly the intrinsic dynamic mechanical behaviour of a CNT, which is the natural base for explaining the rheological responses of more complex CNT suspensions. On the other hand, this modelling framework is not fortuitous; in fact, it is strongly inspired by the polymer kinetic theory, whose cornerstone models were initially developed to explain the dynamic behaviour of linear polymer chains in dilute solution.

Particular interest in the fluid dynamics of SWNT suspensions is also well ground. For instance, SWNTs are considered as a perfect constituent material for obtaining very strong and ultra light electro-mechanical components based on nano-filaments [7, 8], carbon fibres [9] and transparent films [10]. Additionally, SWNTs have a great biomedical potential as an effective gene and drug delivery system through cell membranes [11, 12].

This document is organized in three main chapters. Chapter 1 contains the introduction material of this research work. An overview about the structure, the properties and the applications of CNTs is presented in the opening section (§1.1). Next section 1.2 deals with CNT suspensions. An analysis on the key factors controlling the physical properties of CNT suspensions (suspending medium, filler aspect ratio, concentration regime, dispersion state and surface-treatment of CNTs) is established in the light of the recent publications. Subsequently, a summary of the state-of-the-art in rheology of CNT suspensions is given in §1.3 covering all the concentration regimes. Key findings on the rheological behaviour of CNT suspensions are distinguished in function of the concentration; going from the dilute to the highly concentrated regime. Particularly, §1.3.2 is devoted to a detailed review of the literature concerning the experimental characterisation and modelling approaches in shear-rheology of diluted suspensions of treated SWNTs within a Newtonian solvent, which actually constitutes the framework of the modelling developed in this dissetation. Special attention is paid to the linear viscoelastic responses under dynamic and relaxation test functions, because at present there is not consensus explaining the physical origin of those rheological responses. In other words, looking for a unified physical basis explaining the

rheological signatures obtained in small-amplitude oscillatory deformation tests and small shear-strain step tests constitutes the main motivation of this thesis.

After the scope of the modelling is defined, Chapter 2 illustrates extensively the BD modelling approach, which constitutes the numerical methodology used in this work. Choice of the BD approach is in phase with the several analogies made between the rheological behaviour of CNT suspensions and that one of rigid rod-like polymer solutions [13, 14]. BD simulations have demonstrated to be useful for developing and enriching the micro-mechanical models proposed to mimic the structure of polymer molecules in the framework of kinetic theory. For the previous reason, the BD approach is more than suitable for testing the dynamic response of a coarse-grained physical model intended to mimic the structure of an individual SWNT. In sections 2.1 and 2.2 a close relation between the kinetic theory, intended to explain the rheology of complex fluids, and the stochastic approach is established. The general principles behind the BD technique and the arguments justifying the use of the stochastic approach, in spite of the computational cost associated with, are discussed. Readers will find in §2.3 more concrete descriptions of the BD algorithms employed throughout this thesis for simulating a small-amplitude oscillatory deformation test and a small shear-strain step test, in the framework of linear viscoelasticity. In the last two sections of the chapter (§2.4 and §2.5), a deep examination about the implementation of a BD simulation in linear viscoelasticity of diluted suspensions is tackled at the light of the classical bead-rod-spring models encountered in computational rheology. Kinematic formulations, integration schemes and expressions to calculate the stress tensor are revised for several representative models: Rouse and Zimm theories, freely-jointed multi-bead-rod models and semi-flexible filaments. In §2.4 and §2.5, the implemented BD technique is, on the one hand, validated in front of the analytical or exact numerical solutions known for some classical kinetic theory models; and, on the other hand, is control-set thanks to the analysis of the main numerical issues involved in a BD simulation.

Finally, Chapter 3 establishes the point of convergence of the two first chapters and, at the same time, constitutes a compilation of all the original contributions obtained in this research work to the field of the numerical simulation of the rheological properties of SWNTs suspensions. Based on a meticulous analysis of the structure of the SWNTs and the experimental evidence about their dynamic behaviour in solution, an equivalent micro-mechanical model intended to mimic the dynamics of a SWNT in dilute suspension is proposed in the initial section §3.1. This physical model is supported basically on two facts: the existence of topological defects in the graphitic-like walls that are intrinsically associated with some CNT structural instabilities and bent junctions [15, 16] and, the bendable nature of SWNTs, which has been demonstrated to play a fundamental role on their dynamic behaviour in liquids [17]. In the subsequent sections, from 3.2 to 3.4, with the aim of evaluate the consistence of the proposed micro-mechanical model, the BD framework developed in the second chapter is employed to simulate the linear viscoelastic response of the SWNT-model in dilute solution under dynamic and relaxation test functions. Comparisons with the available experimental data of SWNT dilute suspensions

are satisfactory and promising.

Conclusions, remaining challenges and perspectives of this research work are summarized in a separated concluding chapter.

In addition, an extended abstract of this dissertation in French language can be found in Appendix B.

Chapter 1

Carbon Nanotubes, Suspensions, and Rheology

1.1 Carbon Nanotubes

1.1.1 Structure

Carbon nanotubes (CNTs) constitute an allotropic form of carbon. In CNTs the four valance electrons of each carbon atom are *localized* in three hybrid orbitals $2sp^2$ and one orbital $2p$. Due to this electronic configuration carbon atoms are covalently bonded ($\sim$119 kcal mol^{-1} [18]) in one plan forming a hexagonal honeycomb-like lattice. A single-walled carbon nanotube (SWNT) can be figured out by rolling-up one graphite-like lattice and closing it to form a cylindrical structure, often closed at each end by a fullerene-like cap. On the other hand, a multi-walled carbon nanotube (MWNT) can be imagined as several SWNTs stacked one inside the other as Russian puppets [19].

Since the beginning of the 70s, the existence of carbon filament structures with diameters of the order of nanometers was known [20]. However, it was only until the beginning of the 90s that those structures were observed and recognized as a new allotropic form of carbon. In 1991 Iijima observed by transmission electron microscopy (TEM) a deposit of MWNTs, each of one was formed by 2 to 50 concentric cylinders with a central tube diameter between 2.2 nm and 4.8 nm and an inter-tube distance of 0.34 nm [21]. Length of MWNTs is about several hundreds of nanometers, but millimetre-long MWNTs have been reported [1]. Sometimes, MWNTs are not constituted by perfectly parallel graphitic walls and other kinds of stacking are possible: for instance, bamboo and conic caps. SWNTs were observed two years after the first image of MWNTs [22, 23]. SWNT diameters have been reported between 0.4 nm and 5.0 nm [19].

CNT structure is also determined by helicity. For each individual nanotube, helicity is given by the rolling-up vector of the graphitic lattice. This rolling-up vector defines three kinds of conformations: zigzag, armchair and chiral [24]. According to the helicity, CNT can be electrically semi-conducting or metallic-like.

CNTs are usually assembled in aligned bundles following a hexagonal stacking. Normally each bundle is formed by 10 to 15 CNTs, whose diameters and helicities are not necessarily the same. In the same way, bundles can be associated between them to form bigger structures [19].

1.1.2 Properties

Interest in CNTs lies in the compromise between their unique structure and their impressive physical properties. In the last decades, classical measurement methods have been progressively readapted to the nano-scale in order to estimate experimentally the properties of CNTs. Prediction of CNT properties by computer-assisted modelling has been employed to adjust those experimental methods. For that reason is not surprising that the actual database of CNT properties is referred to experimental and modelling sources.

First estimations on CNT properties were obtained by molecular dynamics (MD). Force-field [25, 26], bond order [27, 28, 29], Lennard-Jones [30, 31] and local density approximation [32] have been the empirical bonding potential models employed in the MD simulations predicting properties of CNTs.

Tensile stiffness in CNTs is relatively high due to the cylindrical-packed molecular structure and the strong covalent bonding C-C. On the other hand, possibility of re-hybridation of the most outer orbitals of the carbon atoms in the graphitic lattice confers to CNTs a high bending flexibility. According to the MD estimations compiled by [24] the Young modulus of CNTs can vary between 0.6 TPa and 5.5 TPa. Dispersion in the MD predictions is mainly attributed to the choice of the bonding potential and the definition of the geometry. Experimental measurements of the Young modulus are coherent with theoretical predictions, but data are also wide dispersed. Dispersion in this case is explained by the variability in experimental methodologies, CNT diameters and synthesis processes [19]. CNT's Young modulus has been measured by micro-Raman spectroscopy, classical tensile tests, atomic force microscopy (AFM) and scanning electronic microscopy (SEM). It has been shown also that the electric arc produced CNTs are almost two-fold stiffer than those produced by hydrocarbon decomposition [33]. Experimental Young modulus has been found between 0.3 TPa and 3.6 TPa for SWNTs [34, 35, 36] and between 0.3 TPa and 2.4 TPa for MWNTs [34, 37, 33].

Experimental measurements of the tensile strength of CNTs have demonstrated indirectly the existence of structural defects because the measured values are quite lower than the theoretical predictions for a perfect CNT. Experimental evidence also showed a high correlation between defects concentration and synthesis process. Even if tensile strength of CNTs is not as high as the theoretical expectations, it is not negligible because it is 10-100 times higher than the strongest steel. Measured values of tensile strength for SWNTs have been found between 13 GPa and 55 GPa [35, 38, 39]. MWNTs have showed experimental tensile strengths from 2 GPa to 63 GPa [37, 40]. On the other hand, MD simulations taking into account the presence of defects in the CNT structure have predicted slightly

higher tensile strengths: from 93 GPa to 150 GPa [41, 42].

Additional to their good mechanical performance, CNTs have exceptional electrical properties. Helicity is the physical factor controlling the nature of the electrical conductivity in CNTs: going from semi-conducting to metallic [43]. Electrical current densities of about 109 A cm^{-2} have been measured in metallic CNTs, 1000 times higher than copper for example [44, 45]. Given the high electrical conductivity, CNTs exhibit also excellent field-emission properties. For example, a field-emission threshold between 4 V μm^{-1} and 7 V μm^{-1} is required to reach a stable current of 10 mA cm^{-2} by tunnel effect in a SWNT [46].

Due to the high density of free electrons and the high aspect ratio of CNTs, this material experiments ballistic conduction along its axis. This fact is reflected in a high thermal conductivity; for instance, 3500 W m^{-1} K^{-1} for a SWNT [47].

1.1.3 Applications

The unique structure of CNTs and the varied properties of this new material have inspired a large range of applications going from the electronics to the medical field. Given their adjustable electrical properties, CNTs are envisaged as one of the new materials required to reduce the size of electronic circuits. CNTs can be imagined as a simple transmission element (quantum wire) or as component of more complex electrical devices [48]; for instance, diodes [49], single-electron transistors [50], field-effect transistors [51], logic gates [52] and even memories [53, 54]. Field-emission properties have been used to conceive emission sources for different applications: electronic microscopes [55], luminescent devices [56], flat-panel displays [57] and portable X-ray tubes [58]. High aspect ratios combined with an elevated mechanical strength make of CNTs an ideal candidate for producing nano-probes for near-field microscopes as, for example, atomic force and scanning tunnelling microscopes [59]. High resolution detectors for different gaseous molecules have been designed taking advantage of the diminution of the electrical conductivity in a CNT caused by the adsorption of volatile molecules on its outer-wall [60, 61]. Thanks to the feasibility of chemically modify their surface, CNTs have been imagined as efficient drug and gene delivery systems [62, 63]. Nevertheless, a discussion remains open in order to determine if CNTs are completely innocuous or not [64].

Due to the ability of tailoring the physical properties of CNTs there is a growing interest in develop CNT-based composites. Research community has particularly focused on polymer matrix nano-composites. However, some attempts have been made to obtain CNT-based composites with metallic and ceramic matrices. Because of the expected high strength properties, spinning of CNT-based fibers have received special attention [65, 9, 66]; nevertheless, there are several open-challenges in order to improve the manufacturing process and the final rope properties. High mechanical performance CNT-based composites have been developed and characterised, for instance: poly(methyl methacrylate)/MWNT [67], polystyrene/SWNT [68], polycarbonate/MWNT [69, 70, 71],

epoxy/MWNT [72, 73, 74, 75], polyimide/MWNT [76], latex/MWNT [77], poly(propylene fumarate)/SWNT [78], poly(ethylene oxide)/MWNT [79], melanine-formaldehyde/MWNT [80], polyetherimide/MWNT [81], ethylene vinyl acetate/MWNT [82]. Load transfer between matrix and CNT appears to be the critical factor controlling the mechanical performance of the CNT-based composites. Thanks to the high electrical conductivity, CNTs are being used as electrostatic dissipating filler in automotive plastics parts [83]. CNTs have been incorpored also in polymer matrix in order to improve their flame-retardant properties [84, 5, 82].

A large range of the previously mentioned applications of CNTs requires a transformation processing in liquid phase. For such reason, CNTs are usually suspended into a Newtonian fluid or a viscoelastic matrix (e.g. melted polymer). Control of those transforming processes needs a deep understanding of the rheology of CNT suspensions [4].

1.2 Key Variables in CNT Suspensions

Disperse CNTs into a liquid media is frequently a required step for their processing and the implementation of a large range of their applications. Even more, purification and chemical modification of CNTs usually happen in solution. In consequence, the amount of conceivable CNT applications is as large as the variety of CNT suspensions. It is the author belief that a formal approach to the rheology of CNT suspensions requires first a deep understanding of the key variables controlling their properties.

1.2.1 Suspending Medium

Suspension properties are dictated by the physicochemical interactions between the suspending medium and the CNTs. Usually, suspending medium is chosen preferably in function of the envisaged application, but CNTs are very difficult to solubilise and often suspending medium is selected specifically for dispersing the CNTs. In fact, pristine CNTs tend to form bundles, due to the strong cohesive energy between tubes (> 0.5 eV nm^{-1}) coming from Van der Waals forces, and solvents are called to overcome those attracting inter-tube forces [85]. For instance, pristine SWNTs have been dissolved at high concentrations up to 10 wt.% in a strong acid mixture (sulphuric acid, SO_3, chlorosulfonic acid and triflic acid) in order to facilitate the manufacture of macroscopic CNT-based fibres. SWNTs are highly solubilised thanks to the acid-driven protonation of the nanotube wall that counteracts the tube-tube Van der Waals interactions [14, 13]. An analogue electrical stabilization mechanism was suggested to explain the uniform distribution of chemical vapour deposition (CVD)-grown MWNTs within a bisphenol-A resin [72].

Another approach suggests the addition of a coupling agent promoting an effective wetting between solvent and CNTs. For example, polymer wrapping by poly-electrolyte dispersants has been employed to stabilize oxidized-surface CVD-grown MWNT in aqueous slurries [86] and surfactant-stabilization, assisted by low-power high frequency sonication,

has been used to exfoliate SWNTs in water [87]. However, addition of surfactants in CNT suspensions has been found uninteresting because the obtained filler loadings are low, the intrinsic CNT properties can be degraded and usually surfactants require to be separated from the final composite in an additional downstream operation [5].

In terms of polymer/CNT composites, it has been demonstrated by force-field-based molecular-mechanics calculations that the binding energies and frictional forces between CNTs and a varied range of polymer matrices have only a limited influence in determining the interface strength. Apparently, the mechanical transfer in the CNT/polymer interface strongly depends on the helical conformation of the polymer chain around the nanotube [88].

On the other hand, flow behaviour of a given suspension strongly depends on the rheological character of the suspending medium (Newtonian liquid or viscoelastic matrix) and, in consequence, control and optimization of the processes involving CNT suspensions are largely influenced by the choice of the solvent.

1.2.2 Filler Aspect Ratio

Intrinsically, aspect ratio of an individual CNT is given by the number of constitutive walls, a priori SWNTs exhibit higher aspect ratios than MWNTs.

Synthesis processes have also a direct impact on the aspect ratio of individual CNTs. Defects during CNT growth often lead to shorten the effective nanotube length. CNTs synthesised in gas-phase, by CVD or catalytic growth from carbon monoxide, account fewer defects and are usually longer than CNTs produced by laser ablation or arc-discharge processes [89]. On the other hand, dimensions of CNTs can be controlled by the parameters of the synthesis process. For example, diameter, length and alignment of CVD-grown MWNTs have been controlled by varying the temperature, the catalyst concentration and the reaction time in a CVD reaction furnace with adjustable catalyst-to-carbon ratio injection system [90, 91]. In other example case, adjusting the thickness of the catalyst layer, CNT diameter has been effectively controlled during a plasma-enhanced CVD process [92].

Purification, mixing operations and surface-oxidation processes have also showed to cause damages on the nanotube structure, reflected directly in a shortening of the individual CNTs. Control of the length reduction has been achieved when dispersing CNTs with high shear flow processors for example [93]. CNTs dispersed by ultrasound have also showed an increment of defects [94] and long sonication times have resulted in intensive shortening [95]. On the other hand, controlled shortening of MWNT has been reported by chemical treatment with bromine [96]. Recently, it was suggested that MWNT length reduction can be predicted by controlling temperature and reaction time of the surface-modification by acid treatment [97].

In suspensions, effective filler aspect ratio is function of the dispersion state and the concentration regime that dictate if CNTs are found as isolated tubes, bundles, agglomerates, networks or more frequently a mixture of the previously mentioned states. Using

scattering methods it has been demonstrated that CNTs in suspension are present in varied morphologies as isolated rod-like tubes, ropes, bundles, fractal networks of CNT ropes, agglomerates [98, 99] and, in consequence, a wide range of effective aspect ratios can be deployed.

1.2.3 Concentration Regime

Diverse concentration regimes can be obtained in CNT suspensions in function of the effective aspect ratio and the volumetric content of the filler. Given the high aspect ratio and elevated tensile rigidity, CNTs have been extensively tackled as classical rigid rods when they are in suspension. In fact, different rigid-rod theories have been employed to discuss and analyse the physical properties of CNT suspensions and CNT/polymer composites [95, 100]. For example, based on the tube model of Doi and Edwards, it is possible to define three concentration regimes for a suspension of randomly oriented rigid rod-like fibres within a viscous medium: dilute, semi-dilute (or semi-concentrated) and concentrated [101]. In that context, supposing a slender fibre of length $2l$, diameter d and effective filler aspect ratio $R = l/d$, diluteness condition is given when $\varphi < R^{-2}$, where φ is the volume fraction of fibres. In dilute suspensions, the dynamics of each rod is totally independent from the others, in other words, no physical interaction between suspended rods is supposed. A suspension is said semi-dilute (or semi-concentrated) when the rotation of rods is hindered by the presence of other rods in the system; the respective concentration range is given by $R^{-2} < \varphi < R^{-1}$. At higher concentrations, suspension is considered concentrated, where liquid crystal phases can be developed. At this state, rotation and translation of each rod is inhibited by the presence of the other rods in the suspension [102, 14].

Most of the organic-based CNT suspensions and surfactant-aided aqueous CNT suspensions reported in the literature qualify from a rheological point of view as dilute or semi-dilute [103]. Some exceptions can be found, for instance, the concentrated suspension of HiPCO[1] SWNTs within super-acids, where transition from an isotropic to a lyotropic nematic liquid crystal phase has been observed [14].

On the other hand, throughout the semi-dilute concentration range, the apparition of an interconnecting CNT network has been particularly studied because of the interest on the associated mechanical and electrical applications. The characteristic concentration of this microstructure is known as the rheological percolation threshold. In function of the type of CNT (aspect ratio, physical properties, surface-treatment) and the suspending medium, rheological percolation thresholds have been found varying from 0.1 wt.% to 10 wt.% [70, 74].

[1] High-Pressure CO Conversion

1.2.4 Dispersion State

In function of the physicochemical interactions nanotube/suspending-medium and the concentration regime, a large variety of microstructures can be found in the CNTs suspensions. Isolated tubes, bundles, random agglomerates, networks and even isotropic and nematic phases can be enumerated between the morphological states reported in the literature.

The morphologies of SWNTs within quiescent polyelectrolyte-assisted aqueous suspensions have been studied using light and X-ray scattering methods. According to such techniques, no rod-like character was identified in a length scale going from 10 Å to 50 μm. On the contrary, a fractal network structure made of ropes (bundles of aligned SWNT) was observed. It was also showed that employing a specific ultrasound mixing protocol is possible to obtain isolated rod-like morphology within the suspension [98]. On the other hand, small angle neutron scattering (SANS) has been also used to identify the morphologies of purified SWNTs dispersed in D_2O with the aid of an ionic surfactant. In function of the surfactant employed and the concentration of SWNTs, different scattered signals were observed. For suspensions said well dispersed, SANS profiles showed the presence of isolated rigid rods and loose SWNT three-dimensional networks. Less efficient surfactants generated a mixed morphology constituted probably by isolated tubes, bundles, large agglomerates and even a three-dimensional network of ropes [99].

Rheological measurements have also used for identifying and characterizing the microstructures developed in quiescent CNT suspensions and in the presence of external fields. For example, measurements of reduced viscosity have been employed to identify the morphological transitions from the dilute rigid-rod to the semi-dilute rigid-rod condition and from the latter to the concentrated rigid-rod condition for a suspension made of pristine SWNTs within a super-acids mixture. Rheological signatures were suitable for morphological characterisation because the phase behaviour of the SWNT/super-acid system exhibits many parallels with that one of a rod-like polymer solution. In addition, optical microscopy was employed to characterise the different morphologies developed in the concentrated regime: a biphasic state composed of an isotropic random phase in equilibrium with a self-assembled SWNT-ropes phase (called by the authors as *SWNT spaghetti*) and a single nematic liquid crystal phase [14].

Stability is another aspect controlling the properties of CNT suspensions. Determining how the dispersion state of CNT suspensions evolves in time is crucial for monitoring their processing and tailoring their final applications. For example, monitoring the stability of bare MWNT suspended in uncured poly di-methyl siloxane can be carried out by following the rheological signature of the suspension. In fact, there is a critical mixing time (given by the concentration and the mixing shear stress) marking the limit between unstable and stable suspension. Beyond such critical mixing time the rheological signature of the suspension remains invariable in time and is characteristic of a satisfactory dispersion of highly entangled MWNTs agglomerates. On the contrary, at shorter mixing times, the rheological signature of the suspension is variable and erratic due to the random jamming

of dense nanotube clusters in the system. Moreover, aging by re-aggregation of MWNTs is particularly important at concentrations higher than the rheological percolation threshold [104].

1.2.5 Surface Treatment

As a mean promoting the dispersion of CNTs as individual tubes into the suspending medium, CNTs can be chemically modified on the outer surface in order to overcome the intrinsic attractive forces between CNTs and enhance the compatibility with the suspending medium.

One of those methods of CNT chemical modification is the surface oxidation by acid treatment. Reflux of a strong acids mixture on pristine MWNT introduces phenolic, carboxylic and lactonic groups on the outer-surface of the nanotube. It has been demonstrated by rheological measurements that those surface groups are able to stabilize MWNT aqueous suspensions at higher concentrations than those achieved with non-oxidized MWNT [105].

Previous oxidative route has been employed for further and enhanced surface chemical modifications. Different open-end functions can be attached to the nanotube by standard condensation reactions onto the carboxylic surface groups. For example, SWNTs can be efficiently dispersed in chloroform by covalent functionalization with pyrrolidine via an amidation reaction [106]. A large compendium of the chemical protocols employed to modify the CNT surface by open-end functionalization is available in the literature [107]. Given that open-end functionalization is preceded by an oxidative treatment, this chemical modification is known for shorten and damage CNTs [5]. An alternative surface chemical modification, less destructive, is the side-wall covalent functionalization. Aryl-diazonium salts have been efficiently reacted with ionic-surfactant-coated-SWNTs in aqueous medium. In this way, a stable SWNT aqueous suspension with unbundled nanotubes was obtained [108]. The yield of the side-wall functionalization protocol has been showed to be elevated; one in nine carbon atoms on the CNT outer-wall was shown to be attached to an organic addend [109]. On the other hand, SWNTs functionalized with phenyl groups have been highly sulfonated with the purpose of produce stable aqueous suspensions [110].

Anyway, an obstacle for the extended use of surface treatment protocols is the fact that each chemical modification scatters free electrons in the CNT structure and, in consequence, the high-performance electronic properties of CNTs are compromised [5].

1.3 Rheology of CNT Suspensions

From the previous overview is clear that properties of CNT suspensions depend on several factors coming firstly from the intrinsic characteristics of the filler and the suspending medium. In addition, when put together CNTs and suspending medium, an additional dimension of strongly inter-dependent factors appears determining the properties of the

suspension. Nowadays, in spite of the continuous improvement of the measuring techniques and processing methods, all those factors remain extremely variables; a fact explaining many of the apparent inconsistencies reported in the literature of CNT suspensions [5]. Hence, special care must be taken into account when discussing the physical basis behind the properties of CNT suspensions. In this context, rheological behaviour has been profiled as a powerful tool for properly analysing the bulk microstructure and the mechanical properties of CNT suspensions [105, 68, 69, 14, 111, 112, 70, 113, 114, 115, 116].

On the other hand, transport and processing of CNT suspensions require a deep comprehension of their flow behaviour. In this case again, rheological characterization is a suitable tool for understand the dynamic behaviour of CNT suspensions and correctly predict their processing at large scale [4, 117, 118, 119].

Given the facts, the importance of the study of the rheological behaviour of CNT suspensions is largely justified. In what follows, the most important findings of the state-of-the-art concerning the rheology of CNT suspensions are reviewed.

1.3.1 An Overview by Concentration Regime

At the beginning of 2010 Hobbie published an interesting overview of the shear rheology of CNT suspensions; his paper looks for establishing a parallel with the polymer solutions rheology and, to do it properly his review was presented in terms of concentration regime [6]. Given the importance of the filler volume fraction on the rheological behaviour of CNT suspensions, this section will be structured in the same way as the Hobbie's paper.

The Dilute Regime

Dynamics of a rigid rod-like fibre in dilute suspension is supposed to be independent of any other fibre within the suspending medium. In other words, excluding imposed external fields, the kinematics of the fibre is driven exclusively by its intrinsic structure. In this context, a dilute suspension is an ideal modelling framework to reveal the physics behind the dynamics of an individual fibre. CNTs are supposed to behave as rigid rod-like high-aspect ratio fillers in suspension when they are dispersed in form of individual CNTs or aligned bundles of CNTs. For a given CNT-based rod-like structure of length $2l$, diameter d and effective filler aspect ratio $R = l/d$, the limit of the diluted regime is reached when the filler volume is equal to R^{-2}.

Not astonishingly, shear viscosity is found proportional to the CNT-based slender filler concentration. In other words, curves of the suspension intrinsic viscosity in function of the shear rate are independent of CNT concentration [14, 104]. Based on the theory of rigid rod-like suspensions and the measurement of the zero-shear viscosity in dilute CNT suspensions, a method for determining approximately the length distribution of SWNTs has been proposed [120].

Dilute CNT suspensions have consistently showed a shear thinning behaviour. Relaxation time associated with the beginning of the shear thinning has been satisfactorily

Small-Amplitude Oscillatory Deformation

In both theories, for fibre suspensions and polymer solutions, it is usually supposed that the total shear-stress $\boldsymbol{\tau}$ is the sum of the contribution from the solvent $\boldsymbol{\tau}_s$ and, another $\boldsymbol{\tau}_p$, coming from the suspended entities (fibres or polymer molecules) [141, 102]. Presuming the same for the treated SWNT-epoxy resin system, the contribution of the suspended SWNTs to the complex modulus of the suspension, $G^* = G' + iG''$, can be calculated as follows:

$$G'_p = G' - G'_s \tag{1.1}$$

$$G''_p = G'' - G''_s = G'' - \eta_s \omega \tag{1.2}$$

where G' is the storage modulus, G'' is the loss modulus, p refers to the suspended particles (in this case the SWNTs), s refers to the solvent, η_s is the solvent viscosity and ω is the angular frequency.

When the functionalized SWNT suspensions presented in Fig. 1.1 were submitted to a small-amplitude oscillatory deformation a non-negligible elastic dynamic response was identified in the tested frequency range. Based on Eqs. (1.1) and (1.2), Figs. 1.2 and 1.3 show the contribution of functionalized SWNTs to the storage and loss modulus of those SWNT-epoxy resin suspensions.

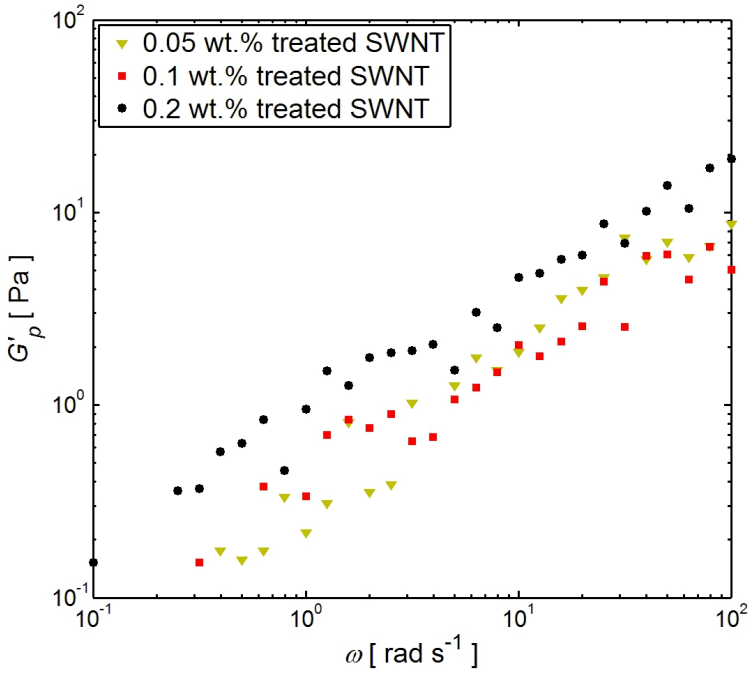

Figure 1.2: Contribution of treated SWNTs to the storage modulus of three different dilute and semi-dilute suspensions within an epoxy resin. Isothermal test at 25°. Epoxy resin is supposed to be Newtonian, so $G'_s \sim 0$. Courtesy of Dr. Anson Ma (Rice University)

A constant-slope evolution for the storage and loss modulus was observed in the tested frequency range. This kind of rheological behaviour was found characteristic of the SWNT suspensions in dilute and semi-dilute concentration regime. Those linear viscoelastic data were fitted with the FP-based orientation model (satisfactory in the steady shear scenario), but using an empirical relationship for the rotary diffusion coefficient that depends on the applied frequency. In other words, a more detailed physical model is required [122].

At present, several hypotheses for explaining this interesting linear viscoelastic response have been postulated as, for example, the existence of a weak SWNT network [112], the electrostatic interactions between surface-treated SWNTs [122] and the bending dynamics of individual SWNTs [142]; however the debate about the physical origins of this mild elasticity in the linear viscoelasticity spectra of dilute SWNT suspensions is far from be closed.

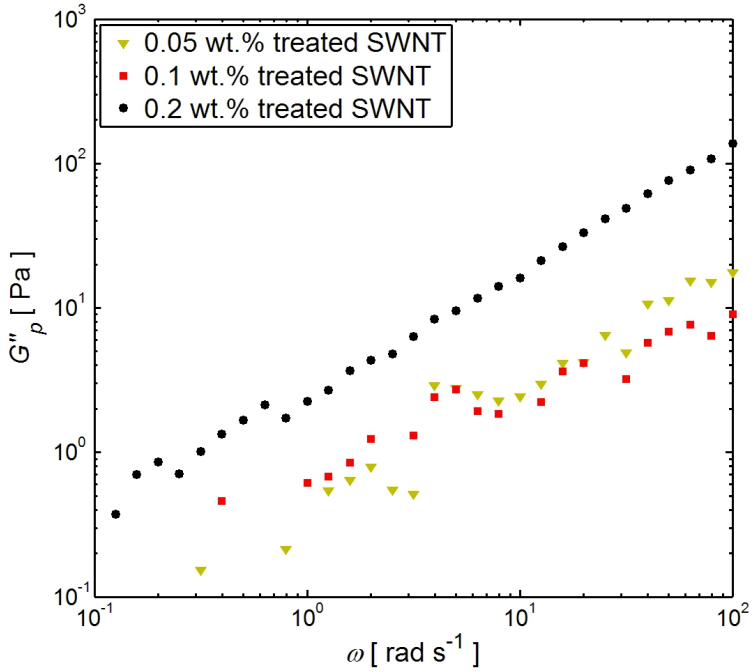

Figure 1.3: Contribution of treated SWNTs to the loss modulus of three different dilute and semi-dilute suspensions within an epoxy resin. Isothermal test at 25°. Epoxy resin is supposed to be Newtonian ($\eta_s = 10$ Pa s). Courtesy of Dr. Anson Ma (Rice University)

Rheological behaviour of CNT suspensions is supposed to be strongly influenced by the recoverable bending of the CNT structure [6]. For instance, it has been conjectured that an elastic dumbbell model is more successful than a rigid dumbbell model for capturing the linear viscoelastic response of treated sonicated carbon nanofiber suspensions given the fact that the former model can incorporate the recoverable bending of the individual carbon nanofibers [140]. Moreover, structure of CNTs has been recurrently mimicked as a mesoscale parallel of the structure of rigid rod-like polymer molecules [14, 121, 125, 6], that usually have been modelled as semi-flexible filaments or worm-like chains [143]. In fact, Brownian dynamics (BD) simulations of small-amplitude dynamical solicitations on dilute

solutions of semi-flexible chains have showed a mild elastic response in the intermediate and high frequency range [144].

Relaxation after Shear-Strain Step

Shear-stress relaxation tests are intended to provide additional information about the spectra of characteristic-times associated to the mechanical response of a viscoelastic system during a transient solicitation. Figure 1.4 presents the shear-stress relaxation signatures after a shear-strain step of 1%, applied to two different concentrated suspensions of treated SWNT (0.1 wt.% and 0.2 wt.%) within an epoxy resin. Relaxation modulus for the solvent alone is also showed for comparison.

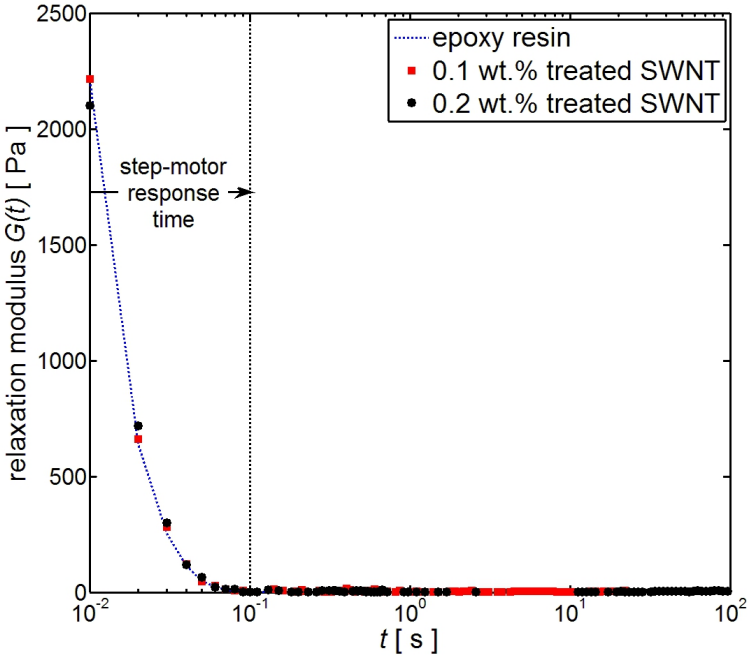

Figure 1.4: Shear-stress relaxation modulus of an epoxy resin and two different dilute suspensions of functionalized SWNT within an epoxy resin. Response after a 1% shear-strain step. Isothermal test at 25°. Courtesy of Dr. Anson Ma (Rice University)

Shear-strain of 1% is within the linear viscoelastic region according to the strain sweep test carried out on the two dilute treated SWNT suspensions showed in Fig. 1.4 [134]. A very fast relaxation process is observed for the two suspensions, even masked by the motor response time of the rheometer. The shear-stress relaxation is very close to that one exhibited by the solvent alone, which in fact corresponds with a completely viscous-fashion response.

Theoretically, existence of a weak SWNT network would be revealed by measuring, at least, a residual shear-stress after the stepper motor response time, but the stress relaxation observed is practically instantaneous.

Research Motivation

From the previous overview about the linear viscoelastic response (in dynamic and transient modes) of dilute and low semi-dilute suspensions of treated SWNT within a Newtonian solvent, it is clear that at present there is a lack of comprehension on the dynamics of an individual SWNT surrounded by small solvent molecules, which is the physics supposed to govern the mechanical response of dilute and low semi-dilute suspensions, where no inter-tube interactions are presumed to exist. On the other hand, a deep comprehension of the dynamics of the SWNT structure as individual entity appears absolutely pertinent before trying to model the rheological behaviour of more concentrated suspensions. In that context, the main goal of the current dissertation is to propose a more detailed physical model of the SWNT structure and to validate it by simulating the linear viscoelastic response of dilute SWNT suspensions (in dynamic and transient mode) by using a BD approach.

Chapter 2

Brownian Dynamics and Rheological Modelling

Analogies between CNTs and polymers have been supported on the similarities observed in the rheological behaviour of their suspensions. For instance, an entanglement-like transition reflected in an abrupt enhancement of the apparent viscosity in function of the concentration has been noticed in aqueous MWNT suspensions and polymer solutions [105, 96]. Moreover, a parallel between the SWNT/super-acid suspensions and the stiff-chain polymer solutions has been clearly established in terms of rheological behaviour and morphological transitions [13]. In fact, regarding the mechanical structure, it has been claimed that an individual SWNT can be thought as a meso-scaled rod-like polymer with a higher persistent length (1-2 orders of magnitude) [14]. Those comparisons have led to describe the dynamics of SWNTs, short DNA, collagen fibrils, F-actin, xanthan, poly(-benzil-L-glutamate) and, even, rod-like viruses in dilute and semi-dilute suspensions by mimicking their structure via a slender semi-flexible filament model [142].

The semi-flexible filament makes part of a series of coarse-grained models developed in the framework of the kinetic theory describing the rheological behaviour of polymer solutions. Brownian dynamics (BD) simulations have been recursively employed to study the dynamic response of more detailed versions of the kinetic-theory models, as a numerical alternative when the analytical treatment becomes complex. In this context, BD appears as a convenient modelling approach for enriching the current physical models proposed to mimic the SWNT structure in dilute suspension.

Given the horizon of the modelling challenge of this dissertation, this chapter deals with the numerical tool to be employed for achieving the task. In the first section, the relation between the polymer kinetic theory and the stochastic approach is illustrated. Subsequently, a general introduction of the BD modelling field is presented, emphasizing on its stochastic nature. Finally, from §2.3 to §2.5, a detailed application of this numerical technique is exposed within the framework of the linear viscoelastic behaviour of dilute suspensions of bead-rod-spring chains. Bead-rod-spring chains constitute the cornerstone of the coarse-grained models developed in *polymer* kinetic theory and their constitutive

equations have been solved analytically. Bead-rod-spring models are simulated in this chapter in order to, firstly, validate the implemented BD algorithms and, secondly, optimize some numerical aspects that will be used in the simulations devoted to the SWNT case in the next chapter.

2.1 Rheology of Polymer Liquids and Kinetic Theory Models

A comprehensive theoretical modelling of the problems in fluid dynamics requires a suitable formulation of the constitutive equation for the momentum flux or stress tensor. Flow of complex fluids differs from that one occurring in classical Newtonian fluids because it cannot be described by using a simple viscous constitutive equation. In fact, the mechanical response of a complex fluid to a given deformation appears to be viscoelastic, in other words, the complex fluid exhibits a mechanical behaviour intermediate between a perfect elastic solid and a perfect viscous liquid. Two viscoelastic regimes can be identified in function of the imposed strain. If the viscoelastic response is independent of the applied strain, then we assist to the linear viscoelastic behaviour. This mechanical regime is typically associated with very small deformations. On the other hand, when the viscoelastic response depends on the applied strain, then we fall in the non-linear viscoelastic regime. This work is focused on linear viscoelasticity because this mechanical regime constitutes the natural first approach in a rheological-modelling framework.

The main aim of rheology consists to establish a suitable constitutive equation that relates stress and strain tensors for a given fluid and, sometimes, for a particular kind of flow. Kinetic theory in complex fluids is an exhaustive mathematical framework that looks for explaining the bulk flow phenomena based on the molecular structure of the fluid system. In that sense, kinetic theory is one of the tools employed by rheologists for generating suitable constitutive equations for non-Newtonian fluids. Formal framework in kinetic theory is built on coarse-grained representations of the molecular structure involved in the flow phenomena. Historically, the former coarse-grained molecular models appeared to emulate the polymer molecular structure. That explains why frequently the literature makes reference to *polymer* kinetic theory.

The coarse-grained molecular models in kinetic theory constitute a first attempt to relate the molecular structure to the bulk flow mechanics. Basic coarse-grained models emulate the most relevant characteristics of the molecular structure using beads, rods and springs as constitutive blocks. In what follows, an overview about the origins of the multi-bead-rod and the multi-bead-spring models is illustrated, based on the descriptions made by Bird et al. elsewhere [141].

2.1.1 Bead-Rod Models

Multi-bead-rod models were proposed to emulate the structure of linear polymer chains. The first natural representation consisted in neglecting the pendant atoms or groups linked

to the central chain and replacing this central chain by a series of beads and mass-less rods, where beads represent the constitutive atoms of the central chain and rods represent the chemical bonds between them. At this level of representation, the stochastic nature of the coarse-grained model emerges because all possible thermal interactions with the solvent molecules are reduced to an instantaneous stochastic force acting on each bead. Adjacent bonds in a linear polymer chain are restricted to very narrow intervals of solid angle values due to sterical hindering [145]. Based on this physical argument, the bead-rod chain model with fixed solid angles and restricted bond-rotation was proposed.

A simpler model considers that the rotational hindrances can be neglected, but the solid angles between adjacent rods are maintained. This representation is known as the *freely-rotating chain* model. A complete series of articles about the non-equilibrium dynamics of the freely rotating chain model has been published [146].

An even coarse-grained multi-bead-rod model neglect any rotating and bending hindering between adjacent rods. This model is known as the *freely-jointed bead-rod chain* or, simply, the *Kramers chain* model. In this case, beads do not represent central chain atoms, but a portion of the polymer chain, typically 10-20 monomer units. In short, a *Kramers chain* can be described as an ensemble of n beads linked by $n-1$ rods of length a (see 2.1), where each bead is characterised by a drag coefficient ζ.

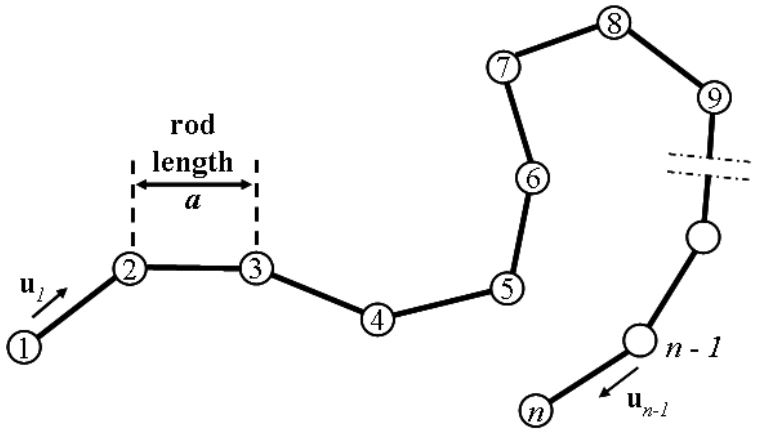

Figure 2.1: Freely-jointed multi-bead-rod model composed of n beads and $n-1$ rods of length a

It has been demonstrated that supposing a random-walk distribution for the *Kramers chain* configuration, the mean-square end-to-end distance at equilibrium writes (see for example [139]):

$$\left\langle r^2 \right\rangle_{eq} = a^2 \left(n-1\right) \tag{2.1}$$

On the other hand, using a thermodynamic approach it was shown that the average tension in a *Kramers chain* suspended in a solvent bath at temperature T and extended

to a fixed end-to-end vector $\mathbf{r}$ (whose norm does not exceed one-half of the contour length of the multi-bead-rod chain) writes as follows:

$$\mathbf{F}^{(c)}(\mathbf{r}) = \frac{3k_BT}{a^2(n-1)}\mathbf{r} \tag{2.2}$$

It is important to point out that previous expression is only exact when supposing a random-walk distribution for the configuration distribution function of the constitutive rods. In fact, this condition is only true for a large number of beads n. Equation (2.2) means that a three-dimensional freely-jointed multi-bead-rod model behaves mechanically as a Hookean spring of null-equilibrium-length with a spring constant H equals to:

$$H = \frac{3k_BT}{a^2(n-1)} = \frac{3k_BT}{\langle r^2\rangle_{eq}} \tag{2.3}$$

2.1.2 Bead-Spring Models

Based on the characteristics of the mechanical behaviour of a freely-jointed multi-bead-rod chain, it seemed natural to propose another up-level of coarse-graining for representing the structure of linear polymer chains. Actually, a linear polymer chain can be modelled as a series of springs, representing several hundreds of central chain atoms, linked by beads that concentrate the masses and the friction effects associated to the replaced central chain atoms. This model is called the freely-jointed multi-bead-spring chain (see 2.2). Several disadvantages appear at this level of coarse-graining: contour length is no more constant and, furthermore, if the spring potential is supposed Hookean, the chain can be infinitely extended, something that is physically unrealistic.

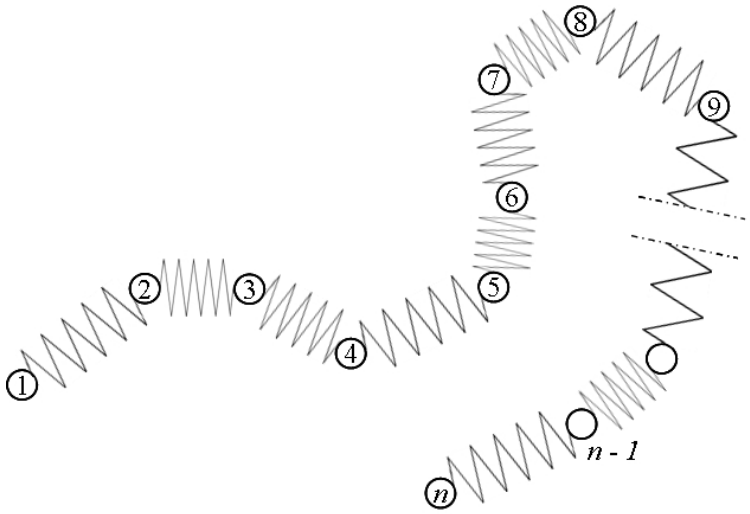

Figure 2.2: Freely-jointed multi-bead-spring model composed of n beads and $n-1$ springs

Considering a freely-jointed multi-bead-spring chain constituted of n beads linked by $n-1$ springs, it results not surprising that the average end-to-end distance at equilibrium

be an extension of the analogue expression derived for the freely-jointed multi-bead-rod model:

$$\left\langle r^2 \right\rangle_{eq} = \frac{3k_B T\,(n-1)}{H} \tag{2.4}$$

In spite of the multi-bead-rod-spring models were initially developed in the framework of *polymer* kinetic theory, those coarse-grained representations has been extended to model a vast kind of systems, including proteins, DNA, virus and CNTs.

One can consider two different approaches when tackling with kinetic theory models: a deterministic and a stochastic one. On the one hand, the deterministic approach deals with the classical resolution of the diffusion equation (or FP equation), which represents the evolution of the probability density function (description of the configurational space) of a given coarse-grained model. On the other hand, the stochastic approach proposes following the motion of a representative population of coarse-grained models and estimating macroscopic properties by properly averaging the physical state of the population under consideration. The BD modelling used in this thesis is in phase with this latter approach.

2.2 The Brownian Dynamics (BD) Approach

2.2.1 Principles

A mathematical representation of all physical phenomena ocurring in the physical world cannot be treated efficiently using only one kind of model. In general, the choice of a given modelling approach depends on the time and length scales involved in the phenomenon. For example, quantum mechanics is a suitable model for representing the physical phenomena occurring at the level of quantum particles and atomic sub-particles, but probably the quantum mechanics framework is not the more convenient choice to model a tensile relaxation test in a polyethylene film. Today, quantum mechanics is the finest description of the physical behaviour of matter. Going up in length and time scales of modelling requires different mathematical formulations with the aim of encapsulate the phenomena occurring at finer scales. For example, between the molecular and macroscopic scales, models must contain a mathematical architecture taking into account the rapid oscillations occurring at lower scales (i.e. atoms, smaller molecules or particles). BD is precisely one of the mathematical frameworks employed for representing the physics at the micro-meso scale (1 nm - 10 μm). In BD the rapid thermal oscillations at lower scales are tackled as a stochastic variable [147].

The historical motivation that inspired the development of the BD framework was the publication of the Robert Brown's observations about the random motion of pollen particles in water. The irregular path described by those pollen particles was explained

afterwards as the result of random thermal collisions between pollen particles and water molecules. By the way, a mathematic formalism describing the motion of a particle submitted to stochastic forces was introduced by the French physicist Paul Langevin [148]. In fact, a general differential stochastic equation is also known as a *Langevin equation*. Considering a Brownian particle (in the large sense, i.e. a discrete portion of matter submitted to stochastic forces coming from the surrounding homogeneous media) of mass M, the instantaneous general *Langevin equation* of motion writes:

$$M\ddot{\mathbf{r}} = -\nabla U\left(\mathbf{r}\right) - \varsigma M\dot{\mathbf{r}} + \varsigma M\boldsymbol{\kappa}\left(\mathbf{r}\right) + \mathbf{F}^{(b)} \tag{2.5}$$

where $\mathbf{r}$ is the particle position, ς is the specific friction coefficient, $\boldsymbol{\kappa}\left(\mathbf{r}\right)$ is the homogenous velocity gradient at the position of the particle, U is the sum of all the particle interaction potentials (e.g. mechanical, electrostatic, magnetic) and $\mathbf{F}^{(b)}$ is the Brownian force acting on the particle. This last variable confers to the differential equation its stochastic nature. Keeping in mind that $\mathbf{F}^{(b)}$ is originated from independent thermal collisions with the surrounding particles; the central limit theorem would conduct intuitively to think that $\mathbf{F}^{(b)}$ behaves following a Gaussian process. In fact, a formal definition of $\mathbf{F}^{(b)}$ in coherence with the stochastic calculus framework writes as follows:

$$\mathbf{F}_t^{(b)} = \sqrt{2k_BT\varsigma M}\frac{d\mathbf{W}_t}{dt} \tag{2.6}$$

where k_B is the Boltzman's constant, T is the absolute temperature and $\mathbf{W}_t$ is a Wiener process. $\mathbf{W}_t$ is a well-defined Gaussian process itself, hence can be defined by the first and second moments of its distribution:

$$\left\langle \mathbf{W}_t \right\rangle = \mathbf{0} \tag{2.7}$$

$$\left\langle \mathbf{W}_{t_1} \otimes \mathbf{W}_{t_2} \right\rangle = \min\left(t_1, t_2\right)\boldsymbol{\delta} \tag{2.8}$$

In a BD simulation, one is rather interested in the numerical implementation of a multi-dimensional increment of a Wiener process, $\Delta\mathbf{W}_{tt'} = \mathbf{W}_t - \mathbf{W}_{t'}$. Using the central limit theorem, it can be demonstrated that those increments are independent and follow also a Gaussian distribution with the next moments:

$$\left\langle \mathbf{W}_t - \mathbf{W}_{t'} \right\rangle = \mathbf{0} \tag{2.9}$$

$$\left\langle \left(\mathbf{W}_t - \mathbf{W}_{t'}\right) \otimes \left(\mathbf{W}_t - \mathbf{W}_{t'}\right) \right\rangle = \left|t - t'\right|\boldsymbol{\delta} \tag{2.10}$$

When implementing an explicit integration of a $\mathcal{D}$-dimensional Wiener process (defined in orthogonal basis) in the time interval $[0, t_n]$, equi-partitioned in n intervals of size $\Delta t = t_i - t_{i-1}$; it is just necessary to define the initial value of the Wiener process, $\mathbf{W}_0 = \mathbf{0}$, and calculate iteratively the function as follows: $\mathbf{W}_{t_i} = \mathbf{W}_{t_{i-1}} + \Delta\mathbf{W}_{t_i}$, where each component

of $\Delta \mathbf{W}_{t_i}$ is obtained from an independent one-dimensional normal distribution $\mathrm{N}(0, \Delta t)$.

Definition of the stochastic Brownian force given in Eq. (2.6) is coherent with the principle of equi-partition of energy, the fluctuation-dissipation theorem (in the sense that frictional force depends only on the instantaneous local velocity) and the formalisms of stochastic calculus [149].

BD is a limit case of the Langevin dynamics framework. In BD the inertial effects are neglected; in other words, BD supposes that no average acceleration takes place on the Brownian particle. In some physical sciences BD is also known as *overdamped* Langevin dynamics. Non-inertia assumption is justified in the insignificance of the inertial forces coming from small-mass particles in front of the viscous and thermal forces acting on the same particle. BD equation of motion for a Brownian particle writes therefore as follows:

$$\mathbf{0} = -\nabla U(\mathbf{r}) - \varsigma M \dot{\mathbf{r}} + \varsigma M \boldsymbol{\kappa}(\mathbf{r}) + \sqrt{2 k_B T \varsigma M} \frac{d\mathbf{W}_t}{dt} \tag{2.11}$$

Defining $\zeta = M\varsigma$ as the friction coefficient and $D = k_B T/\zeta$ as the diffusion coefficient of the particle, the instantaneous velocity of the Brownian particle can be written as follows:

$$\dot{\mathbf{r}} = \frac{-\nabla U(\mathbf{r})}{\zeta} + \boldsymbol{\kappa}(\mathbf{r}) + \sqrt{2D} \frac{d\mathbf{W}_t}{dt} \tag{2.12}$$

BD simulations have been used intensively to study the physics of different kind of macromolecules and soft matter systems [150] as, for example, the rheological behaviour of polymer [151, 152, 153, 154, 155, 156], the dynamics of proteins and DNA [157, 158, 159, 160], the flow behaviour of colloids [161, 162, 163, 164, 165, 166, 167], the structural dynamics of liquid-crystals [168, 169] and the dynamics of CNTs [170, 171, 17].

2.2.2 The Interest of the Stochastic Approach in Rheology

A natural question that appears when studying the dynamics of complex fluids is why to prefer using an extensive (and probably more costly) method for integrating the classical diffusion equation describing the evolution of the probability density function related to the configurational space of a given molecular model. In the conventional framework of the kinetic theory, the equations of motion of the different constitutive blocks in a given coarse-grained model (beads, rods, springs) added to the continuity equation for the configurational distribution function are used to build a Fokker-Planck (FP) equation. The FP equation is a deterministic partial differential equation describing the evolution of the probability density function associated with the configurational space of a given coarse-grained model. The common utility of this deterministic diffusion equation consists in recover the exact physical response of the system when submitted to a given external field by integrating the FP equation in the configurational space and in the time (if looking for dynamic properties) in order to develop constitutive equations. Normally, those constitutive equations are employed a posteriori to calculate more complex flows by using a continuum mechanics framework.

The crucial point in the previously described process lies on the mathematical method employed for integrating the diffusion equation given its multidimensional character. FP equation is a multidimensional function that depends on time and all the space coordinates chosen to define the configuration of a given coarse-grained molecular model. It is necessary to point out that there is a vast collection of numerical strategies developed to solve this problematic integration [172, 173, 174, 175, 176, 177, 178, 179].

However, it appears that more and more the stochastic approach of the kinetic theory is employed for solving the dynamics of coarse-grained models for complex fluids. In this case, the stochastic differential equation of motion for each coarse-grained system is tackled directly. In order to evaluate a given physical property, an average over a finite population of model systems has to be performed (equivalent to the integration of the FP equation in the configurational space) . The main difficulties emerging with this approach are: the associated stochastic noise, the low convergence order and the computational cost required to overcome the first two mentioned obstacles. In the way of thinking of the author this growing-up leaning for tackling the stochastic approach is due mainly to three reasons: i) the enhanced possibility of enrich a given coarse-grained molecular model by analyzing its configurational evolution under designed flow conditions, ii) the raising capacities of the computational tools that reduce the simulation times, and iii) the interesting idea of resolving viscoelastic-flow engineering problems without resorting to closed-forms of the constitutive equations for the stress tensor. This last idea means to establish micro-to-macro simulations where the configuration state of a population of coarsed-grained systems lets to calculate the stress field, allowing to compute the evolution of the flow field and, subsequently, to update the configurational space of coarse-grained models by solving the stochastic differential equations of motion [180, 181, 182, 183, 184, 185, 186, 187].

2.3 BD Simulations of Linear Viscoelasticity Tests

Once established the close relation between the BD approach and the modelling of the rheology of complex fluids, the concrete implementation of a BD simulation in the framework of linear viscoelasticity is tackled now.

From now on an extensive BD modelling approach is systematically used to predict the rheological response of a given micro-mechanical model highly diluted within a Newtonian solvent. Two classical tests used in linear viscoelasticity are simulated: a dynamic test given by a small-amplitude oscillatory deformation and a relaxation test obtained after a rapid shear-strain step.

In both simulation tests, suspension is supposed confined between two parallel infinite-plates (in the case of three-dimensional simulations, see Fig. 2.3) or between two parallel infinite-bars (in the case of bi-dimensional simulations).

Different strain functions can be imposed by tailoring the relative sliding motion of the plates (or bars); inducing a homogeneous deformation within the suspension confined between the plates (or bars). In both simulation tests, rheological response is supposed

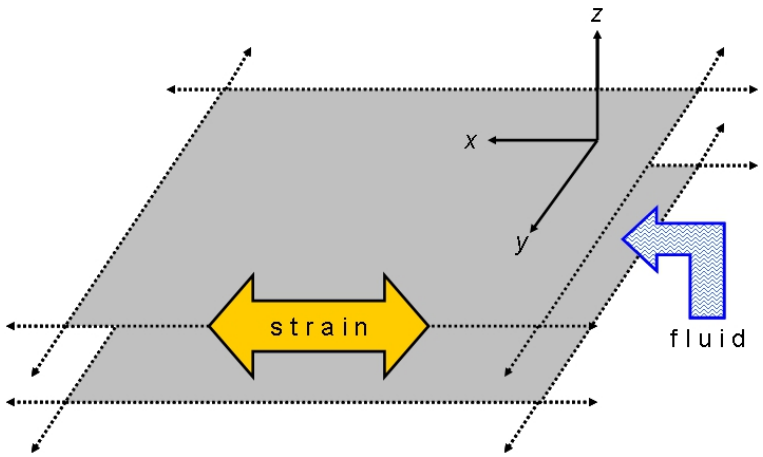

Figure 2.3: Parallel infinite plates where BD simulations in shear rheology are carried out. Upper plate slides in relation to the lower one along the x- axis for homogeneously shearing the fluid confined in between

coming mainly from the bulk of the suspension, therefore wall and free-surface effects are ignored. Rheological properties are calculated from a properly defined average over N micro-mechanical models, where N can be considered as the base-number of degrees of freedom in the BD approach or, simply, the size of the simulation system. As the suspension is supposed highly diluted, no interaction effects are considered between micro-mechanical systems and, hence, no computational storage of the relative positions between micro-mechanical models is necessary. In what follows, more detailed descriptions of the global algorithms employed to simulate each rheological test are presented.

2.3.1 Small-Amplitude Oscillatory Deformation Test

A general flowchart of the algorithm intended to simulate a frequency sweep test in linear regime is presented in Fig. 2.4.

The first step consists to obtain a configuration in thermal equilibrium. No external flow is imposed. Configuration of the BD system (N micro-mechanical models) evolves in time under the action of the forces coming from the friction with the solvent, the internal energy potentials and the thermal interaction with the solvent molecules (Brownian stochastic potential). Time integration in this equilibrium stage is carried out until at least one of two criteria is satisfied: stabilization of the stored internal energy or integration during three times the longest characteristic time associated with the micro-mechanical model.

Once the equilibrium configuration of the BD system has been obtained, the dynamic strain function $\gamma = \gamma_0 \sin \omega t$ can be applied, where γ_0 is a deformation within the linear regime. Frequency sweep test is carried out on a finite number of frequencies homogeneously distributed in logarithmic scale between the lowest frequency ω_1 and the highest frequency ω_n. The BD prediction of the complex modulus at each tested frequency is composed of two steps. First, a dynamic stabilisation of the BD system is carried out during

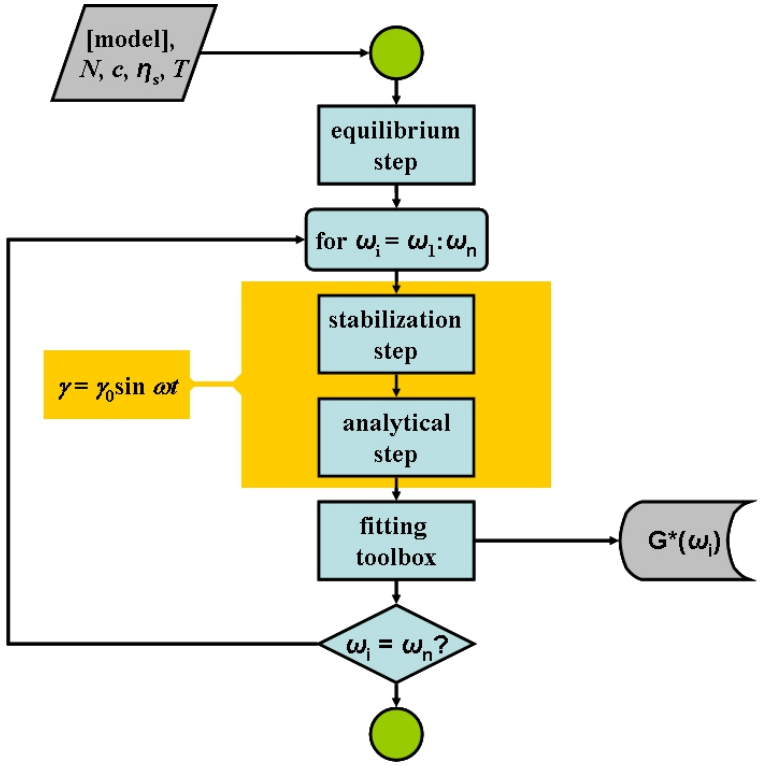

Figure 2.4: Flowchart of the general BD algorithm for simulating a small-amplitude oscillatory deformation test

three times the longest characteristic time before starting the second stage, called analytical step, in which the BD-calculated shear-stress signal is stored during one-and-a-half periodic oscillations. This signal is used as entry variable in a fitting toolbox with the aim of determine the parameters (τ_0, δ) of a smooth shear-stress function $\tau = \tau_0 \sin(\omega t + \delta)$ by using a Newton-based error-minimization methodology. Dynamic complex modulus at each frequency is then computed easily in the next way:

$$G^*(\omega) = G'(\omega) + iG''(\omega) = \frac{\tau_0}{\gamma_0}\cos\delta + i\frac{\tau_0}{\gamma_0}\sin\delta \tag{2.13}$$

where G' is the storage modulus and G'' is the loss modulus.

2.3.2 Relaxation Test after a Shear-Strain Step

A flowchart of the algorithm employed to predict the relaxation shear-modulus after a shear-strain step is presented in Fig. 2.5.

As in the dynamic test, simulation requires a BD system (N micro-mechanical models) in thermal equilibrium before applying the material strain function. An equilibrium stage (i.e. with no external flow) is carried out until one of two criteria is satisfied: stabilization of the stored internal energy or integration during three times the longest characteristic time associated with the micro-mechanical model.

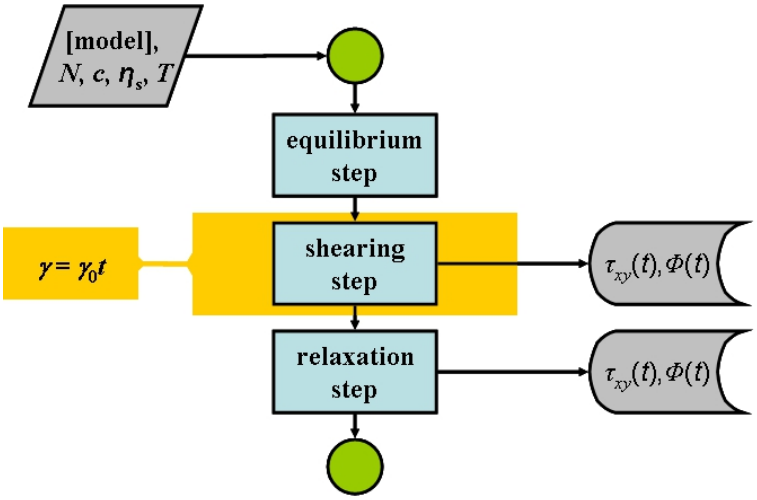

Figure 2.5: Flowchart of the general BD algorithm for simulating a shear-strain step test

Once an equilibrium configuration has been obtained for the BD system, the shear-strain function $\gamma = \dot{\gamma}_0 t$ is applied. During the shear-strain step a constant shear-strain rate $\dot{\gamma}_0$ is imposed during a total charging time t_c and the BD-calculated shear-stress and internal-energy signals are stored. It is important to point out that the shear-strain at the end of the shear-strain step, i.e. $\gamma_0 = \dot{\gamma}_0 \cdot t_c$ is required to be within the linear regime of deformation.

At the end of the charging time, shear-strain function is turned-off to zero and the BD system is let to relax. BD-calculated shear-stress and internal-energy signals are stored in time until at least one of two criteria is satisfied: stabilization of the stored internal energy during one-half of the longest characteristic time of the micro-mechanical model or integration during three times the same longest characteristic time of the micro-mechanical model.

The theoretical basis and the main numerical issues associated with a BD simulation in linear viscoelasticity will be illustrated in the context of the more basical *polymer* kinetic theory models: the multi-bead-spring chain and the multi-bead-rod chain. Validation and optimization of the BD numerical approach is feasible thanks to the well-known exact solutions of the constitutive equations for dilute suspensions of some classical Bead-Rod-Spring chain models: the multi-bead-Hookean-spring model without hydrodynamic interaction (Rouse theory), the multi-bead-Hookean-spring model with equilibrium-averaged hydrodynamic interaction (Zimm theory) and the freely-jointed (three-bead)-(two-rod) chain (*trimer* system).

2.4 BD of Bead-Spring Models

Even though the multi-bead-rod model appeared chronologically earlier than the multi-bead-spring model, this latter is tackled preliminarily here because it offers a simpler mathematical structure that is reflected immediately on the simplicity of the BD numerical methods associated with. In addition, due probably to the simpler mathematic formalisms, the multi-spring-bead model has been more recurrently employed to model the dynamics of complex fluids.

2.4.1 Kinematic Formulation

Let consider the multi-bead-spring chain model in Fig. 2.2. In what follows, a multi-bead-spring chain is constituted of n beads joined by $n-1$ non-bendable springs. The instantaneous position of each bead is defined in a coordinate reference system by the vector $\mathbf{r}_i$. An alternative way for describing the position and the orientation of the multi-bead-spring chain is possible defining the centre of masses of the chain, $\mathbf{r}_c$ and the connector vector $\mathbf{Q}_i$ between consecutive beads:

$$\mathbf{r}_c = \frac{1}{n}\sum_{i=1}^{n}\mathbf{r}_i \tag{2.14}$$

$$\mathbf{Q}_i = \mathbf{r}_{i+1} - \mathbf{r}_i \tag{2.15}$$

Multi-bead-spring chain is supposed suspended into a solvent at temperature T. Solvent is considered a Newtonian fluid with viscosity η_s. Concentration of the multi-bead-spring chain is defined in terms of the number of density, c chains per volume unit. As the solution is supposed highly diluted no interaction between multi-bead-spring chains is considered. Moreover, flow field in the overall suspension is supposed homogeneous, in the meaning that the rate-of-strain tensor is the same in all points of the flow field or, at least, in the scale of twice the contour length of the multi-bead-spring chain [141].

In the kinematic formulation of this kind of coarse-grained model is presumed that all changes of momentum are concentrated on beads. Furthermore, an assumption of inertialess is employed; due to the insignificance of inertial forces (small masses) in front of the friction and thermal forces acting on them. In what follows a detailed description of the forces acting on beads is presented.

Hydrodynamic drag force acting on bead i, $\mathbf{F}_i^{(h)}$

This force describes the resistance experienced by the bead as it moves through the fluid. One of the simplest ways to express this force is given by the Stoke's law, which considers the hydrodynamic drag force proportional to the difference between the fluid velocity at the bead position and the averaged bead velocity. A more general expression takes into account a hydrodynamic interaction component that comes from the physical perturbation

of the local flow field due to the global chain movement. Hydrodynamic drag force acting on bead i writes as follows:

$$\mathbf{F}_i^{(h)} = \boldsymbol{\zeta}\left(\boldsymbol{\kappa}\left(\mathbf{r}_i\right)\cdot\mathbf{r}_i + \mathbf{v}_i^{'} - \dot{\mathbf{r}}_i\right) \tag{2.16}$$

where $\boldsymbol{\zeta}$ is a second-order friction tensor, $\boldsymbol{\kappa}$ is the gradient of the bulk velocity field and $\dot{\mathbf{r}}_i$ is the averaged instantaneous bead velocity. On the other hand, $\mathbf{v}_i^{'}$ accounts for the variation in the local flow field around $\mathbf{r}_i$ due to the motion of the other beads in the same chain.

In *polymer* kinetic theory, Rouse model neglects this intra-molecular interaction (i.e. $\mathbf{v}_i^{'} = \mathbf{0}$); resorting to the well-known *free draining motion* hypothesis [188]. On the other hand, theories taking into account the hydrodynamic interaction suppose that the bead velocity $\mathbf{v}_i^{'}$ depends linearly on the hydrodynamic forces acting on the others beads inside the chain:

$$\mathbf{v}_i^{'} = -\sum_j \boldsymbol{\Omega}_{ij}\cdot\mathbf{F}_j^{(h)} \tag{2.17}$$

where $\boldsymbol{\Omega}_{ij}$ is the Oseen-Burgers hydrodynamic interaction tensor. Say that the perturbation of a velocity field in a given point of the space depends linearly on the hydrodynamic forces acting in the surroundings of that point presupposes a Maxwellian velocity distribution [141]. Oseen-Burgers hydrodynamic tensor writes as follows:

$$\boldsymbol{\Omega}_{ij} = \frac{1}{8\pi\eta_s r_{ji}}\left(\boldsymbol{\delta} + \frac{\mathbf{r}_{ji}\otimes\mathbf{r}_{ji}}{r_{ji}^2}\right) \tag{2.18}$$

where $r_{ji} = \sqrt{\mathbf{r}_{ji}\cdot\mathbf{r}_{ji}}$ and $\boldsymbol{\delta}$ is the unit tensor. Zimm model, in the context of *polymer* kinetic theory, takes into account the hydrodynamic interaction effect using the equilibrium-averaged Oseen-Burgers tensor:

$$\left\langle\boldsymbol{\Omega}_{ij}\right\rangle_{eq} = \frac{1-\delta_{ij}}{6\pi\eta_s}\left\langle\frac{1}{r_{ji}}\right\rangle_{eq}\boldsymbol{\delta} \tag{2.19}$$

Intra-molecular force acting on bead i, $\mathbf{F}_i^{(\phi)}$

This force corresponds to the sum of all the spring forces acting on bead i. In a multi-bead-spring chain, total intra-molecular force on bead i writes as follows:

$$\mathbf{F}_i^{(\phi)} = \sum_{j=1}^{n-1}\left(\delta_{i,j} - \delta_{i,j+1}\right)\mathbf{F}_j^{(c)} \tag{2.20}$$

where $\mathbf{F}_j^{(c)} = \partial\phi_j/\partial\mathbf{Q}_j$ is the connector force acting on bead j along spring j, defined as the gradient of the spring potential energy ϕ_j. Linear force law is the simplest connector

force:

$$\mathbf{F}_i^{(H)} = \frac{\partial \phi_i^{(HOOK)}}{\partial \mathbf{Q}_i} = \frac{\partial}{\partial \mathbf{Q}_i}\left(\frac{1}{2}H\left(\sqrt{\mathbf{Q}_i \cdot \mathbf{Q}_i}\right)^2\right) = H\mathbf{Q}_i \tag{2.21}$$

Previous Hookean-type law force is based on the entropic analysis over a tighten random-walk polymer chain. H is a Hookean spring constant that can be related to temperature and some molecular structural parameters (see §2.1.1). The linear law force is only valid for large polymer chains and small strain regimes. Hence, Hookean law force is inadequate for processes involving large deformations. This fact motivated the use of non-linear force laws, for instance:

- Finite extensible non-linear elastic (FENE) force law [189]

$$\mathbf{F}_i^{(FENE)} = \frac{H\mathbf{Q}_i}{1-(Q_i/Q_{i,0})^2} \tag{2.22}$$

  where $Q_{i,0}$ is the maximal extension of the spring.

- Inverse Langevin (IL) force law [190]

$$\mathbf{F}_i^{(IL)} = \frac{k_B T}{a}\mathcal{L}^{-1}\left[\frac{\mathbf{Q}_i}{Q_{i,0}}\right] \tag{2.23}$$

  where a is typically twice the persistent length l_p and the Langevin function $\mathcal{L}$ is given by $\mathcal{L}(x) = \coth x - x^{-1}$. Persistent length in a polymer molecule is a measure of the flexibility of the chain; in other terms, the direction of the chain-axis in a quiescent polymer molecule is uncorrelated only along contour length distances equal or higher than $2l_p$.

- Worm-like chain (WLC) force law [191]

$$\mathbf{F}_i^{(WLC)} = \frac{k_B T}{a}\left[\frac{1}{2}\frac{1}{(1-Q_i/Q_{i,0})^2} - \frac{1}{2} + \frac{2Q_i}{Q_{i,0}}\right]\frac{\mathbf{Q}_i}{Q_{i,0}} \tag{2.24}$$

A comparison of the various spring-force laws is presented in Fig. 2.6. Observe that FENE-like force laws are linear at small extensions and tends to infinite when extension approaches the finite maximal length.

Brownian force acting on bead i, $\mathbf{F}_i^{(b)}$

The Brownian force accounts for the change of momentum at each bead (supposed as Brownian particles) due to the ensemble of instantaneous collisions of the solvent molecules against it. In nature, those collisions are faster than the bead motion, that is why Brownian forces are considered as stochastic variables in the BD time scale. Due to the isotropic condition of those collisions, Brownian force is treated mathematically as a quantity with

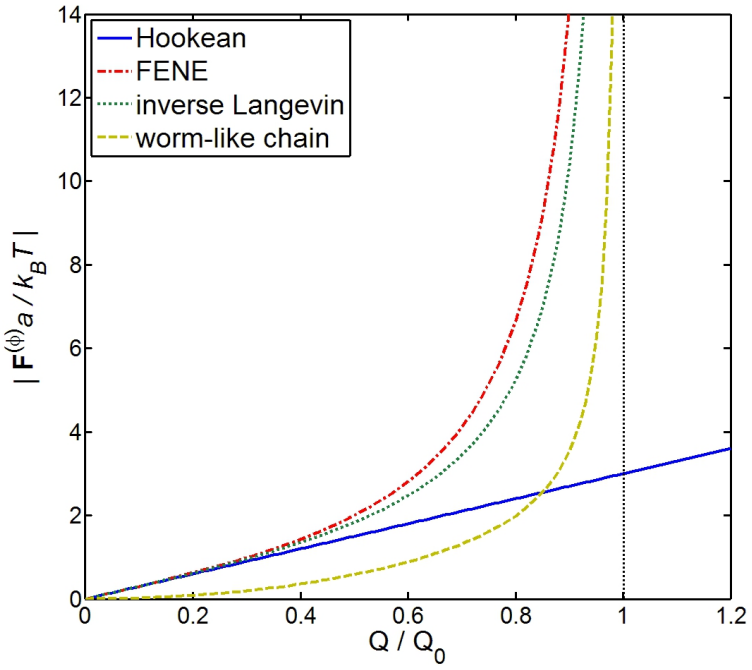

Figure 2.6: Curves of the spring connector force $\left|\mathbf{F}^{(c)}\right|$ in function of the reduced spring extension for several spring force laws employed in *polymer* kinetic theory

zero mean in time and space (ergodicity principle). On the other hand, the second-moment of a the distribution of Brownian forces must to equilibrate the dissipative forces [149]. In short, an "instantaneous" Brownian force distribution in a BD simulation is characterised as a Gaussian process with the next first and second moments:

$$\left\langle \mathbf{F}_i^{(b)}(t) \right\rangle = \mathbf{0} \tag{2.25}$$

$$\left\langle \mathbf{F}_i^{(b)}(t) \otimes \mathbf{F}_j^{(b)}(t+\Delta t) \right\rangle = \frac{2k_B T}{\Delta t}\boldsymbol{\zeta} \tag{2.26}$$

where Δt is a discrete approximation of a differential in time and $\langle \ldots \rangle$ represents an ensemble average. It is important to mention that in an orthogonal basis of $\mathcal{D}$ dimensions the multi-dimensional Gaussian process can be decoupled in $\mathcal{D}$ independent uni-dimensional Gaussian processes [149].

External forces acting on bead i, $\mathbf{F}_i^{(e)}$

Gravitational and electromagnetic fields can induce non-negligible external forces over the beads of the system. These forces are not considered here.

Taking into account that beads are considered as Brownian particles, the inertial effects are neglected. In such context, the force balance must to be satisfied at each time at each bead i:

$$\mathbf{F}_i^{(h)} + \mathbf{F}_i^{(\phi)} + \mathbf{F}_i^{(b)} + \mathbf{F}_i^{(e)} = \mathbf{0} \tag{2.27}$$

Using the definition of the hydrodynamic drag force, previous differential stochastic equation can be transformed to explicit the bead velocity:

$$\frac{d\mathbf{r}_i}{dt} = \mathbf{v}_i^{'} + [\boldsymbol{\kappa}\left(\mathbf{r}_i\right) \cdot \mathbf{r}_i] + \boldsymbol{\zeta}^{-1}\mathbf{F}_i^{(\phi)} + \boldsymbol{\zeta}^{-1}\mathbf{F}_i^{(b)} + \boldsymbol{\zeta}^{-1}\mathbf{F}_i^{(e)} \tag{2.28}$$

Integration in time of previous stochastic equation governs the kinematic evolution of the bead-spring system. As any numerical method, in a BD simulation time is treated as a discrete variable and, hence, different numerical integration schemes can be proposed.

2.4.2 Integration Schemes

Given the structure of Eq. (2.28) a simple explicit integration scheme inspired by the numerical resolution of ordinary differential equations appears as a natural integration scheme. In fact, the Euler-Maruyama method is the simplest way to integrate numerically Eq. (2.28). Given an initial configuration at time t, $\mathbf{r}_{i,\,t}$, is possible to estimate $\mathbf{r}_{i,\,t+\Delta t}$ by using the next formula:

$$\mathbf{r}_{i,\,t+\Delta t} = \mathbf{r}_{i,\,t} + \left(\mathbf{v}_i^{'} + [\boldsymbol{\kappa}\left(\mathbf{r}_i\right) \cdot \mathbf{r}_i] + \boldsymbol{\zeta}^{-1}\mathbf{F}_i^{(\phi)}\right)_t \Delta t + \left(\sqrt{2k_BT\boldsymbol{\zeta}^{-1}}\right)\Delta\mathbf{W}_i \tag{2.29}$$

where $\Delta\mathbf{W}$ is a random increment following a multi-dimensional Wiener process. This random Wiener process follows a normal distribution with the next first and second moments:

$$\langle\Delta\mathbf{W}_i\rangle = \mathbf{0} \tag{2.30}$$

$$\langle\Delta\mathbf{W}_{i,\,t} \otimes \Delta\mathbf{W}_{j,\,t+\Delta t}\rangle = \Delta t\boldsymbol{\delta} \tag{2.31}$$

Rewriting Eq. (2.29) only in terms of the time step Δt we have:

$$\mathbf{r}_{i,\,t+\Delta t} = \mathbf{r}_{i,\,t} + \left(\mathbf{v}_i^{'} + [\boldsymbol{\kappa}\left(\mathbf{r}_i\right) \cdot \mathbf{r}_i] + \boldsymbol{\zeta}^{-1}\mathbf{F}_i^{(\phi)}\right)_t \Delta t + \left(\sqrt{2k_BT\boldsymbol{\zeta}^{-1}\Delta t}\right)\Delta\mathbf{N}_i\left(0,1\right) \tag{2.32}$$

where $\Delta\mathbf{N}_i\left(0,1\right)$ is a multi-dimensional Gaussian increment of mean 0 and variance 1. Performance of the Euler-Maruyama method is extremely sensitive to the time step employed. In fact, convergence of the integration scheme is only guaranteed when $\Delta t \rightarrow 0$

[192]. Suppose a stochastic differential equation with the next general form:

$$dX = A(X)\,dt + B(X)\,dW \tag{2.33}$$

An integration scheme converges strongly with order υ at time t_{max} if the next condition is satisfied:

$$\left\langle \left| X(t_{\max}) - X_{true}(t_{\max}) \right|^2 \right\rangle^{1/2} \leq C\,(\Delta t)^{\upsilon} \tag{2.34}$$

for all time step lengths equal or inferior to Δt and being C a positive constant. It has been proven that the Euler-Maruyama method exhibit a low order of strong convergence $\upsilon = 1/2$ [149]. Identification of the maximal time step satisfying the strong convergence criteria for a specific C value is normally done by trial and error and plotting the error in function of the time step. In spite of the low order of convergence, when the drift and diffusive coefficients ($A(X)$ and $B(X)$ in Eq. (2.32) respectively) are almost constants, the Euler-Maruyama method is the most frequently used integration scheme. Thus, this explicit integration scheme is widely used in BD simulations for bead-spring systems with Hookean-springs.

Now, when the drift and diffusion coefficients become more complex, the fully explicit method is not satisfying and high order integration schemes are required. Such is the case when non-linear spring potentials are employed to guarantee a finite spring extensibility. In fact, the main difficulty appearing with the numerical temporal integration of this kind of bead-spring systems is that the bead displacements have to be bounded in order to not exceed the maximal spring extension. For describing those high-order integration algorithms is better to express the bead-spring chain dynamics (given in the Eq. 2.28) in terms of the connector vector $\mathbf{Q}_i$:

$$\frac{d\mathbf{Q}_i}{dt} = \left(\mathbf{v}'_{i+1} - \mathbf{v}'_i\right) + \left[\boldsymbol{\kappa}(\mathbf{r}_i)\cdot\mathbf{Q}_i\right] + \boldsymbol{\zeta}^{-1}\left(\mathbf{F}^{(\phi)}_{i+1} - \mathbf{F}^{(\phi)}_i\right) + \boldsymbol{\zeta}^{-1}\left(\mathbf{F}^{(b)}_{i+1} - \mathbf{F}^{(b)}_i\right) \tag{2.35}$$

A first approximation to solve the previous equation containing non-linear spring forces consists in use a conventional explicit scheme (Euler-Maruyama or Picard's method) and just reject the updating step that produces a not-physical displacement (maximal spring extension exceeded). Some practical rejection criteria and useful advices for the choice of the time step are given elsewhere [149].

More appropriate methods to integrate Eq. (2.35) are based on implicit schemes. For example, Somasi et al. [193] proposed a fully implicit scheme inspired in the two-step semi-implicit algorithm proposed by Öttinger for FENE dumbbells [149]. In general, at each time step, those implicit methods are composed of a predictor step followed by a corrector one. Given a bead-spring configuration at the time t, $\mathbf{Q}_{i,\,t}$, the configuration after one time step is generated as follows:

- *Predictor step.* Using a conventional explicit scheme an artificial configuration $\mathbf{Q}^*_i$ is

calculated as follows:

$$\mathbf{Q}_i^* = \mathbf{Q}_{i,\,t} + \left[\begin{array}{l} \left(\mathbf{v}'_{i+1,\,t} - \mathbf{v}'_{i,\,t}\right) + \left[\boldsymbol{\kappa}\left(\mathbf{r}_i\right) \cdot \mathbf{Q}_{i,\,t}\right] + \\ \boldsymbol{\zeta}^{-1}\left(\mathbf{F}^{(\phi)}_{i+1,\,t} - \mathbf{F}^{(\phi)}_{i,\,t}\right) + \boldsymbol{\zeta}^{-1}\left(\mathbf{F}^{(b)}_{i+1,\,t} - \mathbf{F}^{(b)}_{i,\,t}\right) \end{array} \right] \Delta t \tag{2.36}$$

- *Corrector step*. Rewriting the spring potential forces in terms of the connector vectors and using the trial configuration obtained in the predictor step to average the flow-field contribution to the drag forces is possible to write an updating time step as follows:

$$\begin{array}{l} \overline{\mathbf{Q}}_i + 2\boldsymbol{\zeta}^{-1}\left(\frac{\partial \phi_i}{\partial \overline{\mathbf{Q}}_i}\right)\Delta t = \mathbf{Q}_{i,\,t} + \frac{1}{2}\left[\boldsymbol{\kappa}\left(\mathbf{r}_i\right) \cdot \mathbf{Q}_{i,\,t} + \boldsymbol{\kappa}\left(\mathbf{r}_i\right) \cdot \mathbf{Q}_i^*\right]\Delta t + \\ \boldsymbol{\zeta}^{-1}\left(\sum_{j=1}^{n-1}\left(\delta_{i,j+1} + \delta_{i+1,j}\right)\left(\frac{\partial \phi_j}{\partial \overline{\mathbf{Q}}_j}\right)\right)\Delta t + \boldsymbol{\zeta}^{-1}\left(\mathbf{F}^{(b)}_{i+1,\,t} - \mathbf{F}^{(b)}_{i,\,t}\right)\Delta t \end{array} \tag{2.37}$$

  The left member of previous equation depends exclusively on the connector vector $\overline{\mathbf{Q}}_i$. By selecting the connector forces treated implicitly in the right side of Eq. (2.37) it is possible to reorder the expression to obtain a cubic equation for the magnitude of $\overline{\mathbf{Q}}_i$. By choosing an appropriate root (inferior to the maximal spring extensibility) for such equation, the non-implicit spring forces (function of the connector vectors) can be updated and an iterative process can be formulated (doing $\mathbf{Q}_i^*$ equal to $\overline{\mathbf{Q}}_i$ from the previous iteration) until difference between consecutive solutions is inferior to a specified tolerance ε:

$$\sqrt{\sum_{i=1}^{n-1}\left(\overline{\mathbf{Q}}_i - \mathbf{Q}_i^*\right)^2} \leq \varepsilon \tag{2.38}$$

  Once the iterative process converges, $\overline{\mathbf{Q}}_i$ is said to be the spring configuration at time $t + \Delta t$, $\mathbf{Q}_{i,\,t+\Delta t}$, with the guarantee that the lengths of the connector vectors are allowed physical ones.

In spite of the heavier calculus involved at each time step in relation to the explicit algorithm, the advantage of the implicit schemes is that larger time steps can be employed. For such reason, each modelling requires a particular analysis for determining which integration method produces a more efficient BD simulation.

Several studies about the numerical integration of non-linear stochastic equations and time step width control are found elsewhere, as well as, relevant examples of BD simulations of bead-spring systems with finite-extensibility spring potentials [194, 195, 196].

2.4.3 Stress Tensor Calculation

In order to obtain the rheological behaviour of any coarse-grained molecular model it is necessary to extract the stress tensor information from its mechanical balance at each

instant. Total shear-stress tensor $\boldsymbol{\tau}$ in a suspension is supposed to be the sum of the contribution coming from the solvent $\boldsymbol{\tau}_s$ and another one coming from the suspended entities $\boldsymbol{\tau}_p$ (in this case, the multi-bead-spring chains) [141]:

$$\boldsymbol{\tau} = \boldsymbol{\tau}_s + \boldsymbol{\tau}_p \tag{2.39}$$

It is important to notice that at equilibrium (i.e. no external forces and no external-flow field), the total shear stress tensor $\boldsymbol{\tau}$ is zero. Assuming that the solvent is a Newtonian fluid, then previous Eq. (2.39) can be rewritten as follows:

$$\boldsymbol{\tau} = \eta_s \dot{\boldsymbol{\gamma}} + \boldsymbol{\tau}_p \tag{2.40}$$

where η_s is the solvent viscosity and $\dot{\boldsymbol{\gamma}}$ is the homogeneous rate-of-strain tensor. Anyway, to model the intrinsic rheological response of the bead-spring chain, one is particularly interested on the shear stress contribution coming from the suspended particles $\boldsymbol{\tau}_p$. In the early literature of *polymer* kinetic theory there are several formal derivations of expressions accounting for the shear stress tensor contribution coming from multi-bead-spring chains suspended in a liquid media [197, 198]. According to those developments in a bead-spring chain there are three principal physical effects contributing to the total shear stress tensor: (1) the intra-molecular forces across the connector vectors; (2) the external forces acting on beads and (3) the transport of momentum caused by the displacement of the beads. Those are not the only sources contributing to the physical mechanical state of the system, but in the framework of a standard rheological test those described mechanisms are definitively the most important.

Based on this deduction guideline, the Kramers expression for the shear-stress tensor contribution coming from a multi-bead-spring chain writes as follows:

$$\boldsymbol{\tau}_p = c\sum_{k=1}^{n-1}\left\langle \mathbf{Q}_k \otimes \mathbf{F}_k^{(c)} \right\rangle - c\sum_{v=1}^{n}\sum_{k=1}^{n-1} B_{vk}\left\langle \mathbf{Q}_k \otimes \mathbf{F}_v^{(e)} \right\rangle - (n-1)\, ck_BT\boldsymbol{\delta} \tag{2.41}$$

where $\langle \ldots \rangle$ represents an average in the configurational space and B_{vk} is a linear operator relating the distance between a bead v and the centre of mass of the chain $\mathbf{r}_c$ with the connector vectors as follows:

$$\mathbf{r}_v - \mathbf{r}_c = \sum_k B_{vk}\mathbf{Q}_k \tag{2.42}$$

The matrix elements of the matrix B_{vk} are defined by [141]:

$$B_{vk} = \begin{cases} \frac{k}{n} & k < n \\ -\left[1 - \frac{k}{n}\right] & k \leq n \end{cases} \tag{2.43}$$

In the right side of Kramers expression in Eq. (2.41) are easily identifiable the three

mentioned physical effects contributing to the shear-stress tensor: the first term corresponds to the intra-molecular forces contribution, the second one represents the contribution of the external forces and the third one accounts for the momentum transfer of beads. This last term is an isotropic contribution to the shear stress tensor based in the supposition of a Maxwellian velocity distribution.

Kramers expression can be slightly transformed by writing the spring-bead chain conformation in terms of the distance of each bead to the centre of mass of the chain, $\mathbf{R}_v = \mathbf{r}_v - \mathbf{r}_c$, and by using the expression relating the intra-molecular force acting on bead v, $\mathbf{F}_v^{(\phi)}$, with the connector force $\mathbf{F}_k^{(c)}$ associated to spring k (Eq. 2.20). Such form is known as the modified-Kramers expression for the shear-stress tensor contribution of a bead-spring chain:

$$\boldsymbol{\tau}_p = -c\sum_{v=1}^{n}\left\langle \mathbf{R}_v \otimes \left(\mathbf{F}_v^{(\phi)} + \mathbf{F}_v^{(e)}\right)\right\rangle - (n-1)\, ck_BT\boldsymbol{\delta} \tag{2.44}$$

Now, combining previous equation with the bead force balance in a multi-bead-spring chain given in Eq. (2.27) and neglecting any external force a much simpler expression for the shear stress tensor can be obtained:

$$\boldsymbol{\tau}_p = c\sum_{v=1}^{n}\left\langle \mathbf{R}_v \otimes \mathbf{F}_v^{(h)}\right\rangle \tag{2.45}$$

where the result $\sum_{v=1}^{n}\left\langle \mathbf{R}_v \otimes \mathbf{F}_v^{(b)}\right\rangle = (n-1)\, k_BT\boldsymbol{\delta}$ has been employed supposing again a Maxwellian velocity distribution. Shear-stress tensor contribution in Eq. (2.45) is known as the Kramers-Kirkwood expression [197, 146].

2.4.4 The Rouse Model

Rouse model is a *polymer* kinetic theory model that mimics the structure of a linear polymer chain using a multi-bead-spring chain, where intra-molecular interactions are neglected. Springs in the Rouse model follows a Hookean law, based on the results of the end-to-end entropic tension experimented by a freely-jointed Kramers chain (following a Gaussian distribution configuration) suspended in an isothermal solvent bath (see §2.1.1). No external forces are considered. A formal compendium of the theory can be found in the recognized publication of Rouse in 1953 [188].

The Hookean-Dumbbell

The simplest version of the Rouse model is the (two-bead)-(one-spring) system or, better known as, the elastic-dumbbell model. It has been found that the mechanical response of the dumbbell model is equivalent to that one of a Maxwell element (spring-dashpot in series) used by rheologists to model a general linear viscoelastic material [199].

Given the simplicity of the dumbbell model, it will be used to study the main numerical

issues of the BD simulations for bead-spring models. An explicit integration scheme has been employed in a three-dimensional BD simulation. First, the equilibrium properties are analysed and, secondly, the dynamic behaviour is presented.

Equilibrium properties

A (two-bead)-(Hookean-spring) system at thermal equilibrium and in absence of an external-flow field has an average square end-to-end distance $\langle r^2 \rangle_{eq}$ equal to:

$$\langle r^2 \rangle_{eq} = \frac{3k_B T}{H} \tag{2.46}$$

An important aspect in BD simulations is the number of entities (or trajectories) required to converge to the central values with satisfactory statistics. In Fig. 2.7 the BD performance to estimate the square end-to-end distance in function of the population considered is presented.

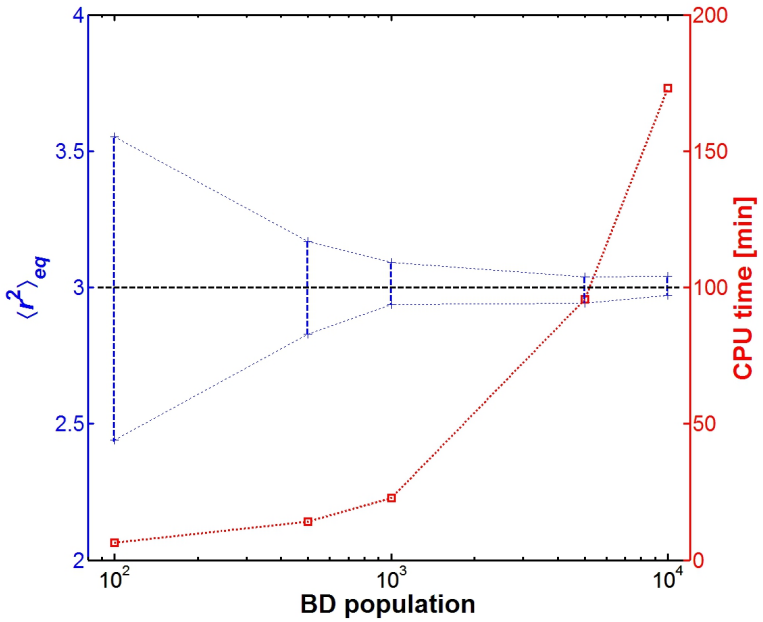

Figure 2.7: Statistics of the square end-to-end distance of a Hookean dumbbell in thermal equilibrium (during 1500 time steps) in function of the BD population. $H = \zeta = k_B T = 1$ are the simulation parameters. Square end-to-end distance at equilibrium is equal to 3 according to the kinetic theory. A time step equal to $\Delta t = \lambda_H/250$ has been employed

The simulated Hookean dumbbell has a square end-to-end distance at equilibrium equal to 3 (given by Eq. 2.46) and a relaxation time of $\lambda_H = 0.25$ according to the kinetic theory framework. A short time step (equivalent to $\Delta t = \lambda_H/250$) was employed in the simulation in order to marginalize the effect of the integration scheme convergence. BD performance is measured as the dispersion of the average square end-to-end distance (95% of confidence) for 1500 time steps once the system has reached an equilibrium configuration (i.e. after

at least 3 times the relaxation time). A reduction of the relative dispersion with respect to the central value is observed from 18.5% for a population of 10^2 dumbbells to 1.1% for a population of 10^4 dumbbells. As expected, a linear evolution of the computational time (Intel® Core™ T7300 2.00 GHz) in function of the number of dumbbells simulated is noticed. For this particular case, a good compromise between simulation accuracy and computational time is obtained for populations between of 10^3 and 5×10^3 dumbbells.

Another important issue in BD simulations, especially when employing an explicit integration scheme, is the time step. In Fig. 2.8 the influence of the time step on the convergence of the integration scheme is revealed. In this case a population of 10^4 dumbbells is employed with the aim of attenuate the noise coming from the random number generation of statistical distributions and isolate the effects originated by the integration scheme.

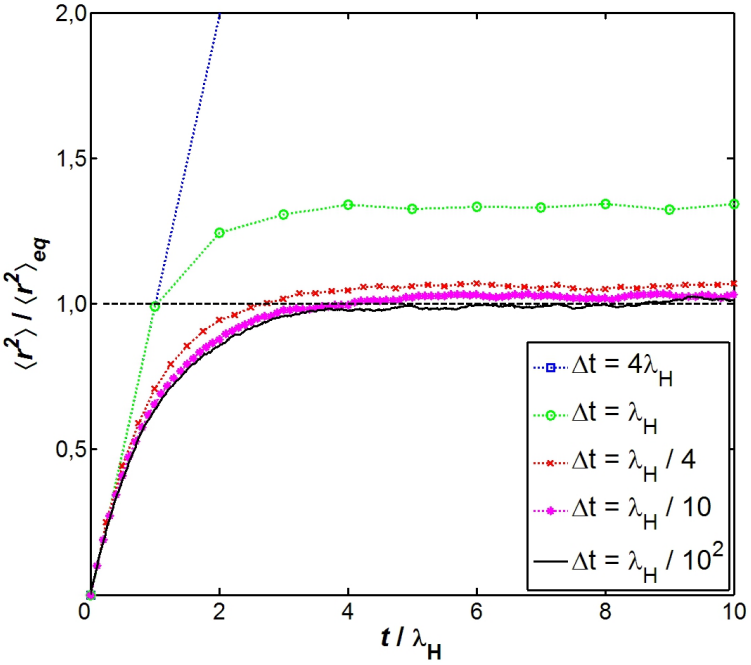

Figure 2.8: Evolution of the reduced square end-to-end distance of a dumbbell after sudden thermal activation for different time steps in the BD simulation. $H = \zeta = k_B T = 1$ are the simulation parameters. Square end-to-end distance is made dimensionless using the equilibrium value given by the kinetic theory. A population of 10^4 dumbbells has been employed

In the Fig. 2.8 the evolution of the squared end-to-end distance of a Hookean dumbbell, after a sudden thermal activation, is presented for different time steps. In absence of temperature, the end-to-end distance of a dumbbell is null. That is the reason why all curves begin at the origin. According to the kinetic theory, a time equal to four times the relaxation time is enough for a Hookean dumbbell model to reach the equilibrium end-to-end distance at constant temperature. From Fig. 2.8, a complete divergence of the integration scheme is observed when a time step bigger than the main relaxation time

is employed. For a time step equal to the relaxation time and equal to a quarter of the relaxation time a convergence of the integration scheme can be appreciated, but the convergence values are inaccurate regarding the kinetic theory values. On the other hand, a finer convergence towards the central values is observed as the time step gets smaller than a tenth of the relaxation time.

At thermal equilibrium, the shear-stress tensor is zero, so for a Hookean dumbbell Kramers expression (Eq. 2.41) writes:

$$\boldsymbol{\tau}_{p,\,eq} = c\left\langle \mathbf{Q} \otimes \mathbf{F}^{(c)} \right\rangle - ck_BT\boldsymbol{\delta} = \mathbf{0} \tag{2.47}$$

which could be written also as:

$$\frac{\left\langle \mathbf{Q} \otimes \mathbf{F}^{(c)} \right\rangle_{eq}}{k_BT} = \boldsymbol{\delta} \tag{2.48}$$

Using a time step equal to $\lambda_H/100$ and an equilibrated population of 10^3 dumbbells (i.e. a BD system equilibrated during a time equal to three times the main relaxation time), the simulation produces a stable shear stress tensor. Third of the trace of the tensor in the left member of Eq. (2.48) has a mean value equal to 0.99 ± 0.03 (95% confidence) during 600 times steps. On the other hand, the out-of-diagonal components of the same tensor have an absolute mean value equal to 0.005 ± 0.063 (95% confidence) during 600 realisations.

Dynamic Properties

The linear viscoelastic behaviour of a Hookean-dumbbell dilute solution can be obtained analytically. The constitutive equation of such system has a well-known solution, that results to be the same of a *convected* Jeffreys model, also known as the *Oldroyd-B model* [141]. Using such constitutive equation, the complex modulus of a Hookean-dumbbell dilute solution writes as follows:

$$G' = \frac{ck_BT\lambda_H^2\omega^2}{1+(\lambda_H\omega)^2} \tag{2.49}$$

$$G'' - \eta_s\omega = \frac{ck_BT\lambda_H\omega}{1+(\lambda_H\omega)^2} \tag{2.50}$$

The BD algorithm employed to estimate the dynamic response of a suspension submitted to a small-amplitude oscillatory strain was previously described in §2.3.1. An explicit integration scheme is implemented in the BD simulation and the Kramers expression is employed to compute the shear stress tensor. Using a time step equal to $\lambda_H/100$ and a population of 10^3 dumbbells (convergent simulation parameters at no-flow conditions), the BD performance is checked in Fig. 2.9 by plotting the loss modulus at the characteristic frequency ($\omega = \lambda_H^{-1}$) in function of the maximal imposed strain.

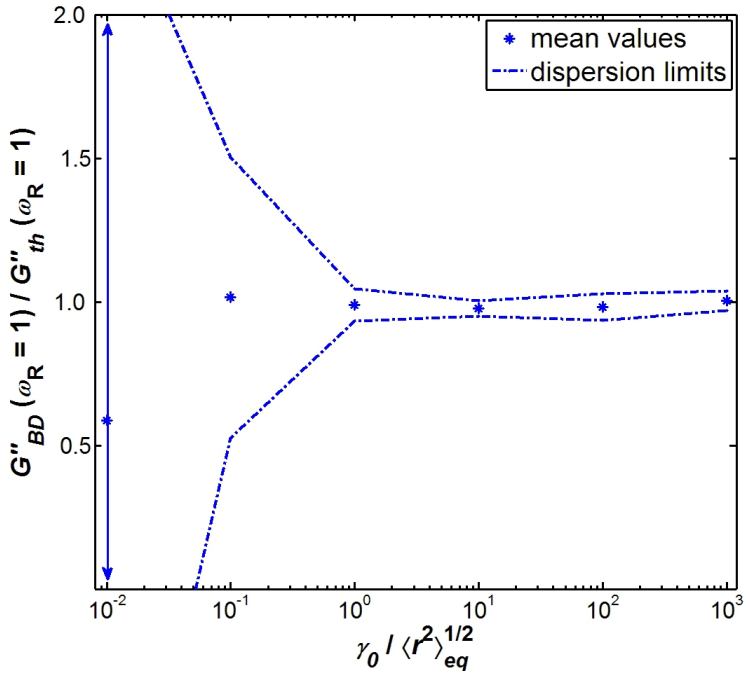

Figure 2.9: BD prediction of the loss modulus at the characteristic frequency for a Hookean dumbbell model in function of the maximal shear strain applied. Maximal shear strain is normalized by the equilibrium end-to-end distance of a Hookean dumbbell model. $H = \zeta = k_B T = 1$ are the simulation parameters. A population of 10^3 dumbbells and a time step equal to $\lambda_H/100$ have been employed

Bead-spring models are not able to describe the decrease of viscosity when shear rate is enhanced [141]. This fact is confirmed by Fig. 2.9 where the BD estimation of the loss modulus at the characteristic frequency appears independent of the maximal shear strain applied. However, a huge numerical dispersion is observed at low strains. This numerical noise is given by the stochastic nature of the Brownian potential when the magnitude of the Brownian forces is equal or higher than the magnitude of the flow-induced forces. A narrower dispersion can be obtained by the implementation of a more precise random number generation algorithm.

At low frequencies the convergence of the integration scheme is guaranteed by the criteria obtained for the no-flow conditions. That is truth because at low frequencies, system motion is controlled essentially by the thermal activity. At high frequencies, nevertheless, additional considerations are needed in order to satisfy the convergence of the integration scheme. In fact, at higher frequencies than the characteristic one, flow-induced forces become the controlling factor of the kinematics of the system and the relative importance of the stochastic forces is progressively reduced. For that reason at high frequencies, as the intensity of the flow field increases time step must to be gradually refined in order to guarantee convergence towards the central values. To show this fact, in Fig. 2.10 the BD convergence at two high frequencies ($\omega_R = 10$ and $\omega_R = 10^2$) is deployed by plotting the relative error of the loss modulus estimation for a population of 10^3 dumbbells with respect to the time step implemented.

From Fig. 2.10, at a reciprocal frequency equal to 10^1, a diminution of the relative error from 16% to 0.7% is appreciated when the time step is reduced from $\lambda_H/100$ to $\lambda_H/10^4$. An even more pronounced effect of the time step is observed for a reciprocal frequency of 10^2, given the high sensitivity of the sine function around zero (phase angle tends to zero as frequency increases). In that case, a diminution of the relative error from 84% to 4% is checked for the same refining of the time step. On the other hand, storage modulus is much less sensitive to the time step than the loss modulus in the high frequency regime because of the less variability of the cosine function with respect to the sine function around zero. For example, at $\omega_R = 10^2$, a reduction of the relative error going from 1.6% to less than 0.1% is observed when the time step is diminished from $\lambda_H/100$ to $\lambda_H/10^4$.

In Fig. 2.11 the global BD performance to predict the complex modulus in a frequency sweep test within a representative frequency interval is presented.

BD performance is depicted by plotting the mean relative error for the storage and loss modulus for 34 frequencies homogenously distributed within an interval of reduced frequencies going from 10^{-2} to 10^2 in function of the time step. A population of 5000 dumbbells is used in the BD simulations. In all the sweep frequency tests a practically constant mean relative error for the storage modulus is obtained ($\sim 2\%$). This inaccuracy in the prediction of the storage modulus is coming mainly from the low frequencies regime ($10^{-2} \leq \omega_R \leq 10^{-1}$) given the high variability of the cosine function approaching $\pi/2$ (phase angle tends to this value as frequency diminishes). No improvement in convergence to the central values is appreciated when refining the time step because the

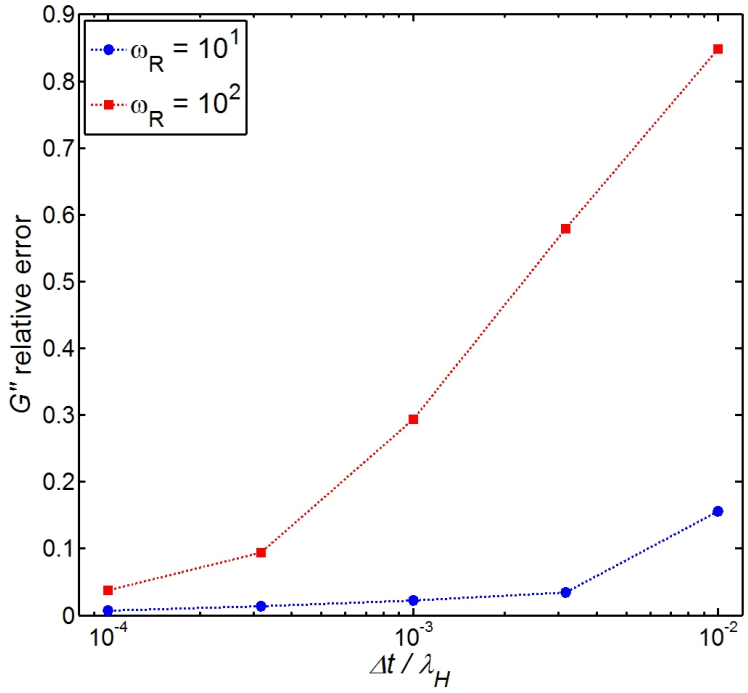

Figure 2.10: Relative error of the BD prediction for the loss modulus at high frequencies in function of the time step. $H = \zeta = k_B T = 1$ are the simulation parameters. A population of 10^3 dumbbells has been employed. Relative error is defined as follows: $|(\log G''_{BD}(\omega_R) - \log G''_{th}(\omega_R)) / \log \Theta|$, where $\Theta = G'_{th}\left(\omega_R = 10^2\right) / G''_{th}\left(\omega_R = 10^2\right)$ is the maximal interval of complex modulus variation in the tested frequency interval

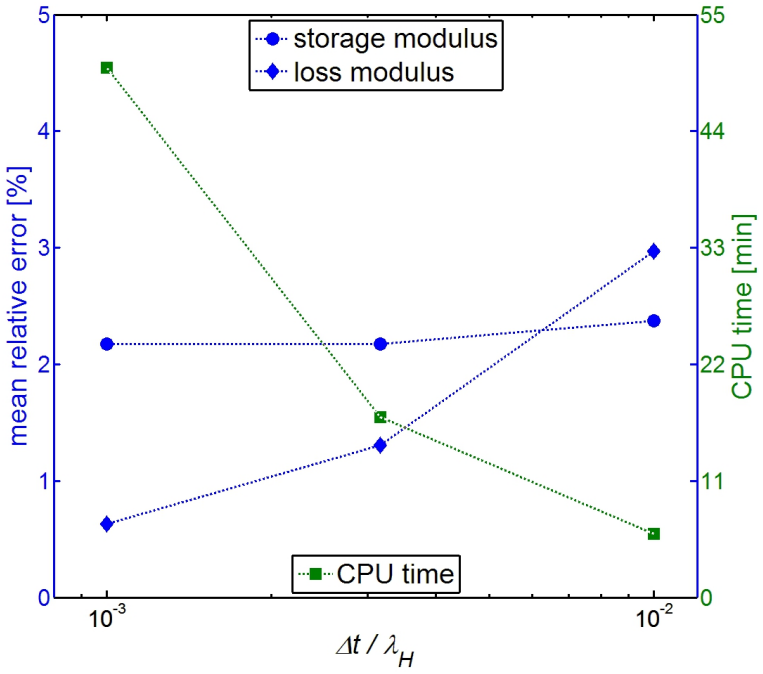

Figure 2.11: Mean relative error of the BD prediction of the storage and loss modulus (for a Hookean dumbbell model) and total computational time in function of the time step implemented. Mean relative errors are calculated as the average of 34 points distributed homogenously in a reduced frequency range going from 10^{-2} to 10^{2}. Relative error is defined as follows: $\left|\left(\log G'_{BD}\left(\omega_R\right) - \log G'_{th}\left(\omega_R\right)\right) / \log \Theta\right|$, where $\Theta = G'_{th}\left(\omega_R = 10^{2}\right) / G'_{th}\left(\omega_R = 10^{-2}\right)$ is the maximal interval of complex modulus variation in the tested frequency interval. $H = \zeta = k_B T = 1$ are the simulation parameters. A population of 5000 dumbbells has been employed

origin of the dispersion is not associated with the integration scheme, but with the natural fluctuations of the stochastic forces that control the kinematics of the dumbbell at low velocities. Implementation of a more sophisticated algorithm for generating random numbers is required to improve the convergence of the storage modulus at low frequencies. In fact, the list of pseudo-random numbers generators is continuously growing as reflect of the remaining challenges in this computational art [149, 200]. On the contrary, a considerable improvement in the loss modulus prediction is checked as smaller time steps are employed. A reduction of the mean relative error from 3.0% to 0.6% is obtained when time step is shortened from $\lambda_H/100$ to $\lambda_H/10^3$. This improvement in convergence for the loss modulus is related directly to the better accuracy at high frequencies, as showed before in Fig. 2.7. As expected, a linear increment on the computational time (4× Intel Itanium® 2 Monticito 1400 MHz) is observed as the time step is shortened.

The Multi-Bead-Spring Chain

The analytical expression of the constitutive equation for the Rouse model (composed of $n-1$ Hookean springs) is well-known. It results to be the linear superposition of $n-1$ Hookean dumbbells with a spectrum of relaxation times λ_j following the next normal modes [141]:

$$\lambda_j = \frac{\zeta/2H}{4\sin^2\left(j\pi/2n\right)} \tag{2.51}$$

When a dilute solution of Rouse chains is submitted to a small-amplitude oscillatory deformation test, the complex modulus contribution given by the chains writes as follows:

$$G' = ck_BT\sum_{j=1}^{n-1}\frac{\lambda_j^2\omega^2}{1+\left(\lambda_j\omega\right)^2} \tag{2.52}$$

$$G'' - \eta_s\omega = ck_BT\sum_{j=1}^{n-1}\frac{\lambda_j\omega}{1+\left(\lambda_j\omega\right)^2} \tag{2.53}$$

In principle, the numerical considerations extracted from the BD simulations with Hookean-dumbbells can be extrapolated to the BD simulations of multi-bead-spring chains. In Figs. 2.12 and 2.13 the BD predictions for the complex modulus of Rouse chains with 1, 10 and 50 springs are compared. All BD simulations are carried out using a population of 5000 chains, a number proved to provide a good compromise between prediction accuracy and computational time (see Fig. 2.7). A frequency sweep test is carried out on 34 points homogeneously distributed in a reciprocal frequency interval going from 10^{-1} to 10^2. A constant time step equal to $\lambda_{n-1}/500$ was implemented, where λ_{n-1} is the shortest time of the relaxation times spectra. This length of the time step was demonstrated to provide also a good compromise between accuracy and computational cost (see Fig. 2.8).

From Fig. 2.12 is observed that the prediction of the storage modulus is less accurate at low frequencies. It was already mentioned that the inaccuracy at low frequencies

comes from the random number generation; hence improvement in the accuracy of the BD prediction is subjected to the implementation of more sophisticated algorithms of random number generation. Quality of the random number generation is only reflected at low frequencies because, at this regime of flow, the dynamics of the multi-bead-spring chain is governed by the randomizing thermal forces; whereas at high frequencies the statistical errors of the computational random number generation are masked by the effects of the external-imposed flow-field.

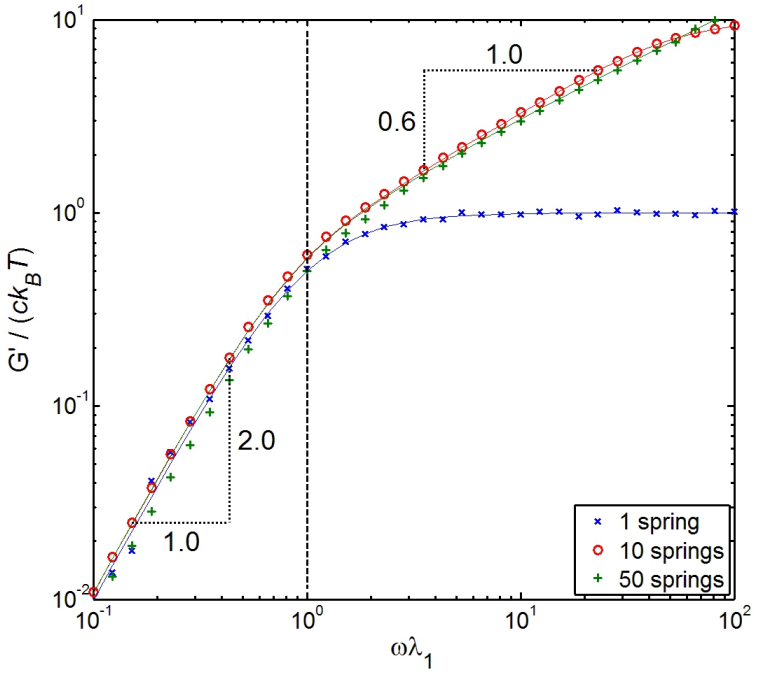

Figure 2.12: BD prediction of the storage modulus in function of the reduced frequency for three Rouse chains: 1-spring, 10-springs and 50-springs. Analytical curves are represented by solid lines. $H = \zeta = k_B T = 1$ are the BD simulation parameters. A population of 5000 chains has been employed

Mean relative errors for the BD prediction of the storage modulus are 0.9%, 0.2% and 0.1% for the Hookean dumbbell, the 10-springs and the 50-springs chain respectively. BD simulations are capable to predict the apparition of new relaxation processes when increasing the number of springs. Notice the elastic enhancement at high frequencies, going from the characteristic plateau of the Hookean dumbbell model to non-zero slopes of the storage modulus in function of the frequency; for instance 0.6 for the 10-springs and 50-springs chain around a reduced frequency of 10. It is worth to mention that Rouse theory predicts a storage modulus evolving with $\omega^{0.5}$ for very long chains ($n > 300$). Tendency towards this limiting value has been registered by the BD simulations; a slight reduction of the storage modulus slope in the high frequency range is appreciated when going from 0.65 for the 10-springs chain to 0.61 for the 50-springs one.

In Fig. 2.13 the BD predictions of the loss modulus in function of the frequency are

plotted for the same Rouse chains presented in the Fig. 2.12. For the Hookean dumbbell system, inaccuracy in the BD prediction is concentrated at high frequencies, on the contrary of the storage modulus. In this case, given the low values of loss modulus at high frequencies, error is coming from a bad resolution of the integration scheme when the phase angle approaches 0. Shorter time steps are required in this frequency window (10^1 to 10^2), but it is important to say that the model response at those frequencies lacks of physical meaning too.

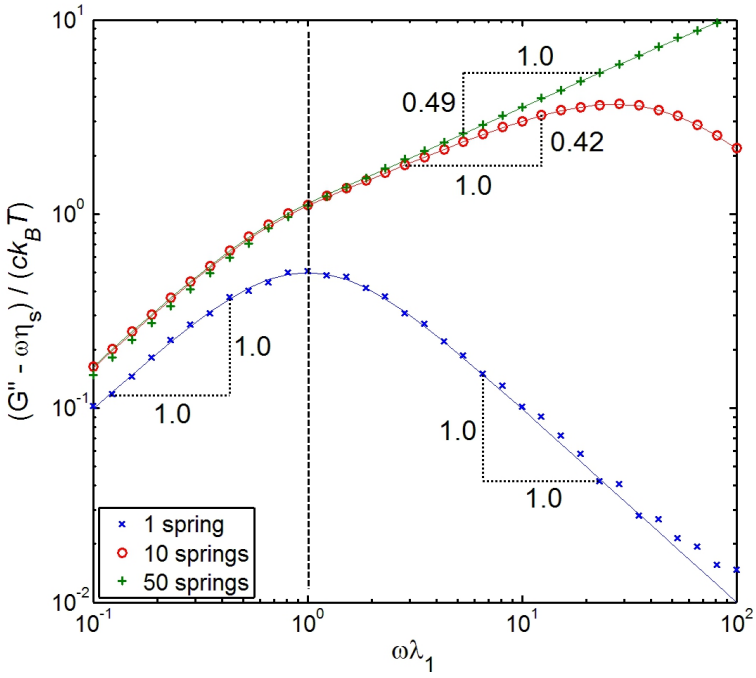

Figure 2.13: BD prediction of the loss modulus in function of the reduced frequency for three Rouse chains: 1-spring, 10-springs and 50-springs. Analytical curves are represented in solid lines. $H = \zeta = k_B T = 1$ are the BD simulation parameters. A population of 5000 chains has been employed

BD simulations are able to correctly predict the evolution of the loss modulus in the high frequency range. Observe, for instance, the linear decrease of the loss modulus for the dumbbell system and the linear increases of the loss modulus for the 10-springs and 50-springs chains at high frequencies. In the high frequency range, the predicted slopes of 0.42 and 0.49 for the 10-springs and 50-springs chains respectively, are also consistent with the maximal limiting value of 0.5 given by the Rouse theory. BD simulations show that when increasing the number of springs, storage and loss moduli tend converging towards the same values in the high frequency range, as predicted by Rouse theory for large number of springs ($n > 300$).

Mean relative errors for the loss modulus prediction are 1.6%, 0.3% and 0.7% for the Hookean dumbbell, the 10-springs and the 50-springs chain respectively. CPU[1] time (4×

[1]Central Processing Unit

Intel Itanium® 2 Monticito 1400 MHz) goes up from 15 minutes to 10 hours when passing from 1-spring to 10-springs, an impressive increment of the computational cost. This fact is explained by the longer main relaxation times when dealing with bigger number of springs that are traduced in longer stabilization steps in the BD algorithm given in §2.3.1, specially in the high frequency range. Additionally, the short time steps required in an explicit integration scheme imply longer analytical steps in the implemented BD algorithm, specially in the low frequency range.

2.4.5 The Zimm Model

Unlike the Rouse model, in Zimm theory hydrodynamic interaction is taken into account. From a formal point of view, the kinematic description is exactly the same as that one of the Rouse model, except for the hydrodynamic drag force, where an additional term is considered to account for the local variation in the bulk flow field caused by the motion of the other beads in the multi-bead-spring chain. Pioneer works on hydrodynamic interaction inside flexible macromolecules are attributed to Kirkwood and Riseman [201, 146]. Zimm adapted the Kirkwood's results in hydrodynamic interaction to the multi-bead-spring model in order to estimate the viscoelastic, birefringence and dielectric properties of dilute polymer solutions. Zimm found the analytical solution of the model by using a transformation to normal coordinates [202].

In the Zimm model, the local interaction term depends linearly on the hydrodynamic forces acting on the other beads of the chain. The equilibrium-averaged Oseen-Burgers hydrodynamic tensor (see §2.4.1) is the linear operator employed and is defined as follows [202]:

$$\langle \boldsymbol{\Omega}_{ij} \rangle_{eq} = \frac{1-\delta_{ij}}{6\pi\eta_s} \sqrt{\frac{2H}{\pi k_B T \left| i-j \right|}}\, \boldsymbol{\delta} \tag{2.54}$$

The particularities of the implementation of a BD simulation for the Zimm model can be revealed by transforming the general expression for the bead velocity given in Eq. (2.28). Considering that in Zimm theory external forces are neglected and an isotropic friction tensor is supposed, the generalized stochastic differential equation in Eq. (2.27) can be rewritten as follows:

$$\frac{d\mathbf{r}_i}{dt} = -\sum_j \langle \boldsymbol{\Omega}_{ij} \rangle_{eq} \cdot \mathbf{F}_j^{(h)} + \left[\boldsymbol{\kappa} \left(\mathbf{r}_i \right) \cdot \mathbf{r}_i \right] + \frac{\mathbf{F}_i^{(\phi)}}{\zeta} + \frac{\mathbf{F}_i^{(b)}}{\zeta} \tag{2.55}$$

where the local hydrodynamic interaction term $\mathbf{v}_i^{'}$ has been approximated by using the equilibrium-averaged Oseen-Burgers hydrodynamic tensor. As the balance of forces over each bead is zero (inertialess Langevin equation) the hydrodynamic force in Eq. (2.55) can

be written in terms of the other forces:

$$\frac{d\mathbf{r}_i}{dt} = \sum_j \langle \mathbf{\Omega}_{ij} \rangle_{eq} \cdot \left[\mathbf{F}_j^{(\phi)} + \mathbf{F}_i^{(b)} \right] + \left[\boldsymbol{\kappa} \left(\mathbf{r}_i \right) \cdot \mathbf{r}_i \right] + \frac{\mathbf{F}_i^{(\phi)}}{\zeta} + \frac{\mathbf{F}_i^{(b)}}{\zeta} \tag{2.56}$$

Reordering and bringing together common terms:

$$\frac{d\mathbf{r}_i}{dt} = \left[\boldsymbol{\kappa} \left(\mathbf{r}_i \right) \cdot \mathbf{r}_i \right] + \frac{1}{\zeta} \sum_j \mathbf{HI}_{ij} \cdot \mathbf{F}_j^{(\phi)} + \frac{1}{\zeta} \sum_j \mathbf{HI}_{ij} \cdot \mathbf{F}_j^{(b)} \tag{2.57}$$

where $\mathbf{HI}_{ij} = \boldsymbol{\delta}_{ij} + \zeta \langle \mathbf{\Omega}_{ij} \rangle_{eq}$ is called the Zimm hydrodynamic interaction tensor. Finally, based on the conditions imposed by the fluctuation-dissipation theorem, the stochastic differential Eq. (2.57) for the bead velocity in a Zimm chain takes the form [147]:

$$\frac{d\mathbf{r}_i}{dt} = \left[\boldsymbol{\kappa} \left(\mathbf{r}_i \right) \cdot \mathbf{r}_i \right] + \frac{1}{\zeta} \sum_j \mathbf{HI}_{ij} \cdot \mathbf{F}_j^{(\phi)} + \sqrt{\frac{2k_B T}{\zeta}} \sum_j \mathbf{C}_{ij} \cdot \frac{d\mathbf{W}_j}{dt} \tag{2.58}$$

where the symmetric Zimm hydrodynamic interaction tensor has been decomposed according to $\mathbf{HI}_{ij} = \sum_k \mathbf{C}_{ik} \cdot \mathbf{C}_{jk}^T$. Usually, component ij of the Zimm hydrodynamic interaction matrix is expressed also using the next formula:

$$HI_{ij} = \delta_{ij} + \left(1 - \delta_{ij}\right) h^* \sqrt{\frac{2}{|i-j|}} \tag{2.59}$$

where h^* is the hydrodynamic interaction parameter according to Thurston and Peterlin [203]:

$$h^* = \frac{\zeta}{\eta_s} \sqrt{\frac{H}{36\pi^3 k_B T}} \tag{2.60}$$

where ζ is the bead friction coefficient, η_s is the solvent viscosity and H is the Hookean-spring constant. The hydrodynamic interaction parameter h^* can be understood also as the ratio of the bead radius to the root-mean-square distance between two beads linked by a spring at equilibrium. In that context, it is expected that h^* is lower than 0.5 [149]. From a practical point of view, experimental viscoelastic data for several polymer solutions are generally well represented by Zimm chains of several hundreds of beads with hydrodynamic interaction parameters between 0.1 and 0.2 [204].

From a numerical point of view (BD approach) integration of the stochastic differential equation for a Zimm chain (Eq. 2.58) does not represent an additional cost with respect to the Rouse chains (Zimm hydrodynamic interaction matrix is constant). In addition, equations employed to describe the kinematics and to compute the shear-stress tensor are quite similar for both models. Hence, the numerical considerations about the number of trajectories required and the time step (in an explicit integration scheme) inferred for Rouse chains can, in principle, be extended to the BD simulations of Zimm chains.

It seems that the calculation of the matrix $\mathbf{C}_{ij}$ has a numerical relevance when general

hydrodynamic interaction (i.e. based on the general expression of the Oseen-Burgers tensor) for chains with large number of beads ($n > 300$) is considered, owing to the fact that the hydrodynamic interaction matrix is recalculated at each time step. Classical Cholesky decomposition is expensive, scaling with the cube of the number of beads [147]. In response, Fixman proposed two alternative numerical methods to calculate the square-root of the hydrodynamic interaction matrix: one by Newton iteration and the other one by Chebyshev polynomial decomposition [205]. Implementation of the last polynomial approximation for the square-root of the hydrodynamic interaction matrix in a BD framework is detailed elsewhere [147]; this method roughly scales with $n^{9/4}$ per time step. In any case, previous numerical issue has a reduced impact on the BD simulation of Zimm chains due to the fact that the equilibrium-averaged hydrodynamic interaction matrix is constant and the required decomposition is carried out just one time for all the simulation.

Given the fact that hydrodynamic interaction is approximated by the equilibrium averaged Oseen-Burgers tensor, a close-form of the constitutive equation can be derived for the Zimm model with the same form of the Rouse model one [141, 149]. For that reason, expressions for the contribution of Zimm chains to the complex modulus of their diluted suspensions have the same form that the equations for Rouse chains (Eqs. 2.52 and 2.53):

$$G' = ck_BT\sum_{j=1}^{n-1}\frac{\tilde{\lambda}_j^2\omega^2}{1+\left(\tilde{\lambda}_j\omega\right)^2} \tag{2.61}$$

$$G'' - \eta_s\omega = ck_BT\sum_{j=1}^{n-1}\frac{\tilde{\lambda}_j\omega}{1+\left(\tilde{\lambda}_j\omega\right)^2} \tag{2.62}$$

The only difference lies on the relaxation time spectra. In the Zimm model the time constants are dictated by:

$$\tilde{\lambda}_j = \frac{\zeta}{2H\tilde{a}_j} \tag{2.63}$$

where $\tilde{a}_j$ are the Eigen-values of the modified Rouse matrix $\tilde{\mathbf{A}}_{ij}$ given by:

$$\tilde{\mathbf{A}}_{ij} = \sum_v\sum_u \bar{\mathbf{B}}_{iv}\mathbf{HI}_{vu}\bar{\mathbf{B}}_{ju} \tag{2.64}$$

and the component vu of the matrix $\bar{\mathbf{B}}_{vu}$ follows the next formula:

$$\bar{B}_{vu} = \delta_{v+1,\,u} - \delta_{v,\,u} \tag{2.65}$$

This analytical solution allows us to evaluate easily the performance of the BD simulation predicting the linear viscoelastic behaviour of multi bead-spring systems with equilibrium-averaged hydrodynamic interaction. Figures 2.14 and 2.15 compare the BD predictions of the complex modulus for a 50-springs Zimm chain with two different hydrodynamic interaction parameters. A frequency sweep test is carried out over 25 points

homogeneously distributed in a reciprocal frequency interval going from 10^{-1} to 10^{2}.

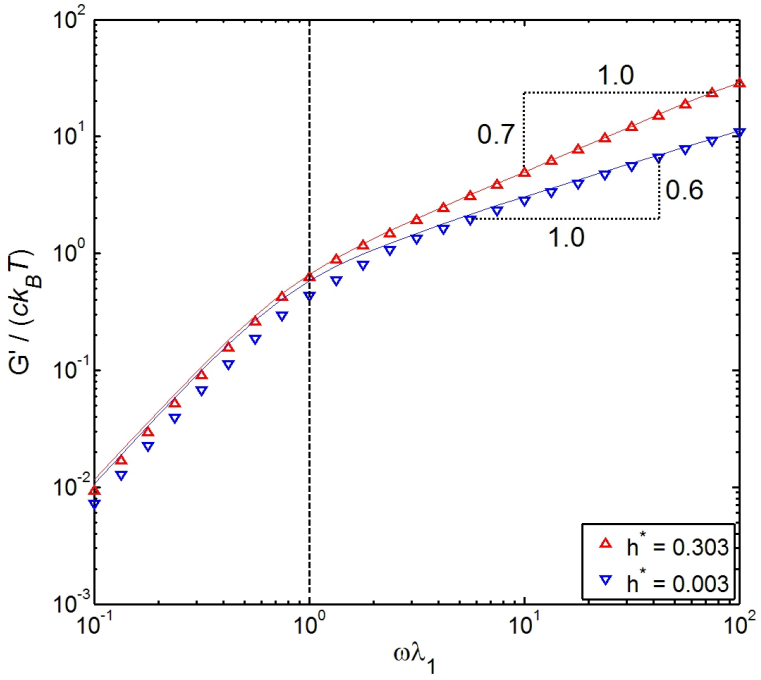

Figure 2.14: BD prediction of the storage modulus in function of the reciprocal frequency for two 50-springs Zimm chains with high hydrodynamic interaction ($h^* = 0.303$) and very low hydrodynamic interaction ($h^* = 0.003$). Analytical curves are represented in solid lines. $H = \zeta = k_BT = 1$ are the BD simulation parameters. A population of 10^4 dumbbells has been employed

From Fig. 2.14 is observed that the BD prediction of the storage modulus is more accurate for the high hydrodynamic interaction case than the low one. In fact, the mean relative error for the low value of h^* is about 2.7% in comparison with the mean relative error of 0.8% for the case of high h^*. The main source of inaccuracy is coming from the low frequency range. This is explained, as in the BD simulations with Rouse chains, by the statistical deviations originated in the numerical computation of the stochastic forces coupled with the relative dominance of the thermal forces as driving mechanism of the chain kinematics in the low frequency range. In consequence, improvement of the accuracy at low frequencies depends on the implementation of more sophisticated random numbers generators.

On the other hand, BD simulations correctly predict the evolution of the storage modulus at high frequencies. Figure 2.14 shows the increase of the slope of G' going from 0.5 for the low hydrodynamic interaction case ($h^* = 0.003$) to 0.7 for the high hydrodynamic interaction case ($h^* = 0.303$), within the reduced frequency interval between 10^1 and 10^2.

In Fig. 2.15 the BD prediction of the loss modulus versus the frequency is plotted for the same Zimm chains presented in Fig. 2.14. As in the storage modulus prediction, a better accuracy is obtained for the high hydrodynamic interaction case. We found a

mean relative error for the low value of h^* equal to 1.6% and a mean relative error near to 0.3% for the high value of h^*. Again, inaccuracy is coming mainly from the low frequency regime. The same reasons invoked to explain the inaccuracy in the prediction of the storage modulus prediction are attributable to the loss modulus case.

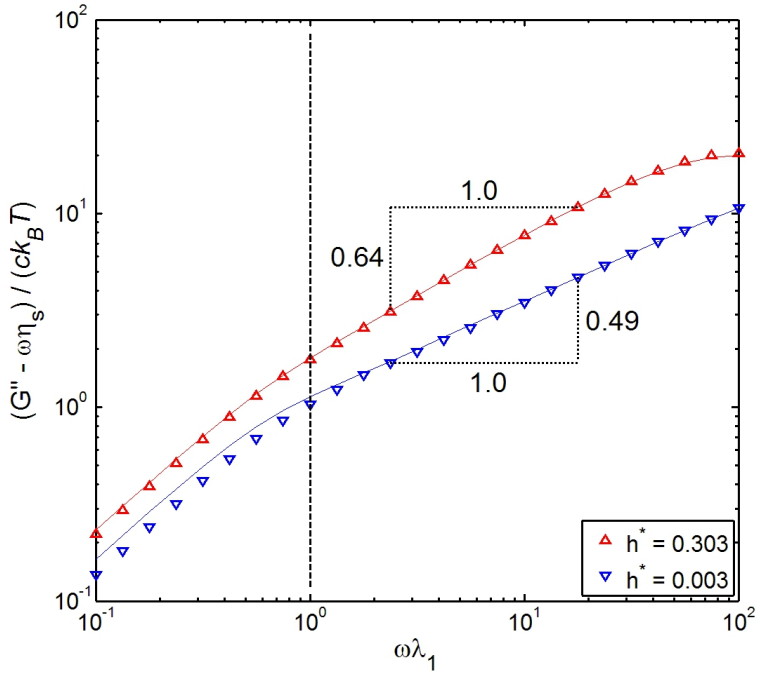

Figure 2.15: BD prediction of the loss modulus in function of the reciprocal frequency for two 50-springs Zimm chains with high hydrodynamic interaction ($h^* = 0.303$) and very low hydrodynamic interaction ($h^* = 0.003$). Analytical curves are represented in solid lines. $H = \zeta = k_BT = 1$ are the BD simulation parameters. A population of 10^4 dumbbells has been employed

BD performance at high frequencies is quite better. Simulations are able to correctly predict the change in the loss modulus slope when varying the relative importance of the hydrodynamic interaction. At low hydrodynamic interaction a Rouse-type slope is observed, whereas at high hydrodynamic interaction ($h^* = 0.303$), the slope of the loss modulus reaches a maximal value of 0.64 around a reduced frequency of 10. This prediction is consistent with the Zimm theory, where the maximal slope for the loss modulus is 2/3 [206]. It is worth to say that for very long chains (i.e. $n > 300$) with high hydrodynamic interaction (for instance, $h^* = 0.3$) Zimm theory predicts a storage and loss moduli evolving with $\omega^{2/3}$ and a constant ratio $(G'' - \eta_s\omega)/G' = \sqrt{3}$ in the high frequency range.

2.5 BD of Bead-Rod Models

The fundamental difference between the bead-rod model and the bead-spring model lies in that the former has a finite contour length. This simple, but important fact is traduced

directly in different rheological responses. On the other hand, a physical model with a finite contour length imposes subtle, but important numerical issues that are reflected in the BD implementation.

As mentioned in §2.1.1, historically bead-rod models were first proposed to emulate the structure of linear polymers in a coarse-grained fashion. Bead-rod model with fixed adjacent angles (as proposed by Flory [145]) constitute the first stage of coarse-graining in kinetic theory. In that model, rods are supposed to represent the bond length between two consecutive atoms in the backbone of the polymer chain. Simpler representations with fewer degrees of freedom have been extensively proposed. For instance, some polymer chains are quite bendable along certain number of monomer units, in those cases from 3 to 5 monomer units can be replaced by one non-bendable rod. Polymer flexibility is then mimicked by introducing some kind of bending potential between consecutive rods. Continuous version of this model is known as the worm-like chain, in which the thermal equilibrium configuration is a perfect straight filament. An even coarser model replaces from 10 to 20 monomer units by one rigid-rod; any notion of flexion hindering at this rod-scale is lost and the polymer chain is represented then by a freely-jointed multi-rod chain [141]. An ultimate scale in the coarse-graining process replaces a hundred of backbone atoms (or a ten of rods from the freely-jointed multi-rod model) by an *entropic* spring, so mechanical behaviour of the macromolecule is represented by a multi-bead-spring chain model (showed in the previous section §2.4). Despite that the historical motivation for the bead-rod model is linked to the polymer science, this representation has been extensible applied to emulate the mechanical behaviour of other structures as short DNA, rod-like virus, collagen fibrils, synthetic polymers and CNTs.

Bead-rod models have escaped from a deeply development in the kinetic theory framework with respect to the bead-spring counterparts because the inextensibility condition imposes the use of generalized coordinates [207]. This mathematical complexity explains why only some results in zero-shear, steady and linear unsteady flows have been obtained for this model [208, 209].

In the case of bead-rod models, BD simulations appear as an interesting alternative approach to by-pass the complex mathematical-treatment of the diffusion equation. Anyway, the use of constraints also implies to be careful during a BD implementation, particularly in terms of the integration scheme and the stochastic forces generation.

Bead-rod models have been particularly studied for approaching the mechanical behaviour of bead-spring chains with very stiff Fraenkel-type springs (non-zero natural length). Intuitively a very stiff Fraenkel spring could be replaced by a rigid rod for the sake of mathematical simplicity. However, it is found that this limit is a very singular one. In fact, bead-rod chains and bead-spring chains differ even in the limit of infinitely stiff springs. For instance, the configurational distribution of a freely-jointed multi-bead-rod chain at thermal equilibrium is found to be different from a random-walk distribution, which is typical for a freely-jointed multi-bead-spring chain [141]. This difference has been confirmed by molecular and Brownian dynamics simulations [210, 211, 212, 151]

and statistical mechanics calculations [213, 214]. On the other hand, it has been showed that introducing a corrective potential force (function of the chain configuration) into the multi-bead-rod chain formulation is possible to mimic the behaviour of multi-bead-spring chains [213, 215]. This result strongly promoted the use of BD simulations for studying the dynamical behaviour of polymers by using the multi-bead-rod model and the corrective potential approach [196, 205, 216, 217, 218, 144, 142]. In this work, the intrinsic behaviour of multi-bead-rod models is tackled; the bead-spring chain statistics is not intended to be mimicked.

In what follows, the basis for a BD implementation of a flexible multi-bead-rod chain with an isotropic friction tensor and in absence of hydrodynamic interaction is presented. Numerical issues are analysed by simulating the freely-jointed (three-bead)-(two-rod) chain or *trimer* system.

2.5.1 Kinematic Formulation

Constraints can be tackled mathematically in a generalized coordinate system (based on the configuration of the chain) or in a Cartesian coordinate system, case in whiwh constraint forces are required to complement the kinematic description. Going and coming back between those two frameworks requires a lot of care in order to conserve a proper equivalence at the levels of the FP equation and the differential stochastic equation [149].

From a formal point of view a general, expression of the FP equation for a multi-bead-rod model, including hydrodynamic interaction and anisotropic friction tensor, was given by Curtiss using generalized coordinates [141]. This diffusion equation is coherent with the equilibrium statistical mechanics for a real bead-rod chain with equal bead masses; in other words, this diffusion equation describes the intrinsic dynamical behaviour of a multi-bead-rod chain. A detailed description of the development of an equivalent stochastic differential equation in the strong sense was given by Öttinger [149]. He also showed a particular transformation of that differential stochastic equation from generalized to Cartesian coordinates. In doing so, not only an explicit definition of the rod inextensibility is required, but also a metric potential force, depending on the chain configuration, has to be considered in order to respect the equivalence (at least in a weak sense) with the FP equation developed by Curtiss. Interestingly, it is found that the negative of such metric force is equal to the corrective potential force added in the BD numerical algorithms of multi-bead-rod chains intended to mimic the behaviour of multi-bead-spring chains.

For the sake of simplicity, the BD implementation in a Cartesian coordinate system is tackled in this thesis. Metric potential forces are neglected without incurring in error because, in one hand, the drag acting on the simulated multi-bead-rod chain is supposed characterized by an isotropic friction tensor and, on the other hand, no hydrodynamic interactions are considered. A particular time-integration algorithm, described further on, is required in order to consistently neglect the metric potential forces. Otherwise, potential metric forces cannot be ignored if one wants that the BD simulation reflects the intrinsic

behaviour of multi-bead-rod chains. So, let us consider the multi-bead-rod chain model showed in Fig. 2.16. Multi-bead-rod chain is constituted of n beads joined by $n-1$ non-bendable rigid rods of length a.

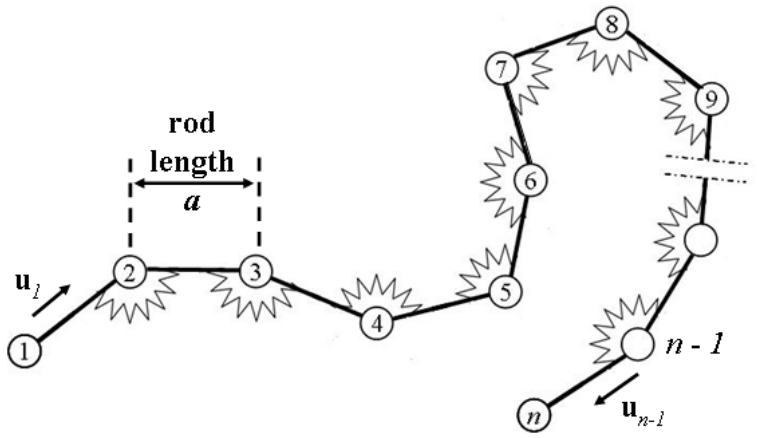

Figure 2.16: Non-freely jointed multi-bead rod model composed of n beads and $n-1$ rods of length a. Bending potential between rods in the multi-bead-rod chain model is mimicked with a hypothetical torsion spring

Position of the bead-rod chain can be instantaneously defined in a Cartesian reference system by the ensemble of bead positions $\mathbf{r}_i$ and the centre of mass of the chain $\mathbf{r}_c$ (see Eq. 2.14). Orientation of each rod is given by the vector $\mathbf{u}_j$, which is a unit vector collinear to the rod connecting beads j and $j+1$. $\mathbf{u}_j$ is defined as follows:

$$\mathbf{u}_j = (\mathbf{r}_{j+1} - \mathbf{r}_j)/a \tag{2.66}$$

Rods are supposed infinitely rigid. Physical length of the system is equivalent to the total length of the multi bead-rod model $(n-1)a$. Existence of an internal bending potential, coming from an hypothetical torsion spring between each pair of rods, is considered with the aim of mimic the bending flexibility of the filament-like physical system. On the other hand, multi-bead-rod chains are supposed suspended into a Newtonian solvent (viscosity η_s) at temperature T. Concentration of the multi-bead-rod chains is defined in terms of c chains per volume unit. High dilution hypothesis is made, so no inter-chain interactions are considered. Moreover, flow field acting on the overall suspension is supposed homogeneous. Beads are considered the centres of hydrodynamic resistance; so all forces are concentred on beads. In what follows, forces acting on the multi-bead-rod chain are described in more detail.

Hydrodynamic drag force acting on bead i, $\mathbf{F}_i^{(h)}$

Physical origin and mathematical description of this force are the same given for the multi-bead-spring model (see §2.4.1). As mentioned before, hydrodynamic interaction is

neglected and an isotropic friction coefficient is supposed in order to avoid the calculation of metric potential forces.

Constraint forces acting on bead i, $\mathbf{F}_i^{(\lambda)}$

This force takes into account the sum of rod tensions acting on each bead i. Rod tension λ_j corresponds to the module of the instantaneous force emerging on bead j for maintaining the distance between beads j and $j+1$ at a constant value a. This force is transmitted along the rigid-rod and is manifested on bead $j+1$ with an opposite sign. Mathematically, total constraint force on bead i can be expressed as follows:

$$\mathbf{F}_i^{(\lambda)} = -\sum_{j=1}^{n-1} \mathbf{n}_{ij}\lambda_j \tag{2.67}$$

where $\mathbf{n}_{ij}$ is a linear operator defined as follows:

$$\mathbf{n}_{ij} = \mathbf{u}_j \left(\delta_{i,j+1} - \delta_{i,j}\right) \tag{2.68}$$

Internal bending potential force acting on bead i, $\mathbf{F}_i^{(\phi)}$

Based on the viscoelastic theory of concentrated solutions of semi-flexible polymers [143], Pasquali and Morse defined a discrete bending potential for a multi-bead-rod model based on the worm-like chain continuous model [218]:

$$\phi = -\frac{K_b}{a}\sum_{i=2}^{n-1} \mathbf{u}_i \cdot \mathbf{u}_{i-1} \tag{2.69}$$

where ϕ is the internal-bending potential and K_b is a bending rigidity constant. The bending potential defined in Eq. (2.69) can be understood as coming from the mechanical action of a torsion spring between two consecutive rods. In this case, local bending energy is proportional to the cosine of the internal angle between two consecutive rods. In other words, minimal internal bending energy state is achieved when all rods are completely aligned. Usually, this linear relationship is restricted to small flexion angles. Obviously, definitions of non-linear bending potentials are required for large deformation scenarios. Bending force acting on bead k can be obtained as the derivate of the bending potential in Eq. (2.69) with respect to the position of bead k:

$$\mathbf{F}_i^{(\phi)} = -\frac{\partial \phi}{\partial \mathbf{r}_k} = \frac{K_b}{a}\sum_{i=2}^{n-1} \frac{\partial\left(\mathbf{u}_i \cdot \mathbf{u}_{i-1}\right)}{\partial \mathbf{r}_k} \tag{2.70}$$

To simplify the derivate on the right side of Eq. (2.70), next identity is employed [218]:

$$\frac{\partial}{\partial \mathbf{r}_k}\mathbf{u}_i = \frac{1}{a}\left(\delta_{k,i+1} - \delta_{k,i}\right)\left(\boldsymbol{\delta} - \mathbf{u}_i \otimes \mathbf{u}_i\right) \tag{2.71}$$

Brownian force acting on bead i, $\mathbf{F}_i^{(b)}$

As in all coarse-grained models, Brownian forces approach the change of momentum of a bead i coming from the thermal activity of the solvent molecules surrounding bead i. Accounting for faster processes than the coarse-grained model motion, Brownian forces are computed as an stochastic process. In a model without constraints (free particles, bead-spring chains), Brownian forces follow a normal distribution with first and second moments defined previously by Eqs. (2.25) and (2.26), respectively. However, as the generalized friction of the bead-rod system is modified by the presence of constraints, random forces must reflect the inextensibility of rods [217]. To show this, let us take the example of one single rigid-rod embedded into a solvent at temperature T, no external flow is imposed. Supposing an isotropic friction coefficient, force balances on the two mass-less beads write:

$$-\zeta\dot{\mathbf{r}}_1 - \mathbf{n}_{11}\lambda_1 + \mathbf{F}_1^{(b)} = m_1\ddot{\mathbf{r}}_1 = \mathbf{0} \tag{2.72}$$

$$-\zeta\dot{\mathbf{r}}_2 - \mathbf{n}_{21}\lambda_1 + \mathbf{F}_2^{(b)} = m_2\ddot{\mathbf{r}}_2 = \mathbf{0} \tag{2.73}$$

On the other hand, with the purpose of satisfy the inextensibility of the rigid-rod, next condition has to be imposed over the bead velocities:

$$0 = \sum_{i=1}^{2} \dot{\mathbf{r}}_i \cdot \mathbf{n}_{i1} = (\dot{\mathbf{r}}_2 - \dot{\mathbf{r}}_1) \cdot \mathbf{u}_1 \tag{2.74}$$

Placing the bead velocities from Eqs. (2.72) and (2.73) into Eq. (2.74) we obtain:

$$\frac{1}{\zeta}\left(-\lambda_1\mathbf{u}_1 + \mathbf{F}_2^{(b)} - \lambda_1\mathbf{u}_1 - \mathbf{F}_1^{(b)}\right) \cdot \mathbf{u}_1 = 0 \tag{2.75}$$

Equation 2.75 can be rewritten also as follows:

$$2\lambda_1 = \sum_{i=1}^{2} \mathbf{F}_i^{(b)} \cdot \mathbf{n}_{i1} = \left(\mathbf{F}_2^{(b)} - \mathbf{F}_1^{(b)}\right) \cdot \mathbf{u}_1 \tag{2.76}$$

Previous equation resumes the conditions imposed over the Brownian forces in order to satisfy the inextensibility condition. Two numerical algorithms dedicated to the random forces generation can be considered at this point. The first takes into account the contribution of random forces to the rod tensions and implies to calculate λ_1 at each time step from Eq. (2.76). In the second, contributions of random forces to the rod tension are neglected ($\lambda_1 = 0$) and unconstrained random forces have to be projected in order to satisfy $0 = \sum_{i=1}^{2} \mathbf{F}_i^{(b)} \cdot \mathbf{n}_{i1}$. Last supposition has no consequences on the rod kinematics because rod velocity depends exclusively on the orthogonal component of the Brownian forces with respect to the rod orientation-vector. In order to obtain projected random forces $\mathbf{F}_i^{(b)'}$, it is necessary to substrate the "hard" component of the unconstrained Brownian forces $\hat{\eta}_1$

along the rod direction as follows:

$$\mathbf{F}_i^{(b)'} = \mathbf{F}_i^{(b)} - \mathbf{n}_{i1}\hat{\eta}_1 \tag{2.77}$$

The "hard" component of the unconstrained Brownian forces can be obtained from the solution of the next equation:

$$\hat{G}\hat{\eta}_1 = \mathbf{F}_i^{(b)} \cdot \mathbf{n}_{i1} \tag{2.78}$$

where $\hat{G} = \mathbf{n}_{i1} \cdot \mathbf{n}_{i1} = 2$. From Eqs. (2.76) and (2.78) is easily inferred that $\hat{\eta}_1 = \lambda_1$. Hence, projected Brownian forces are $\mathbf{F}_1^{(b)'} = \mathbf{F}_1^{(b)} + \lambda_1\mathbf{u}_1$ and $\mathbf{F}_2^{(b)'} = \mathbf{F}_2^{(b)} - \lambda_1\mathbf{u}_1$. A graphic example of this projection in a bi-dimensional case is showed in Fig. 2.17. Extension of previous algorithm for a multi-bead-rod case is straightforward and has been detailed elsewhere [216, 217].

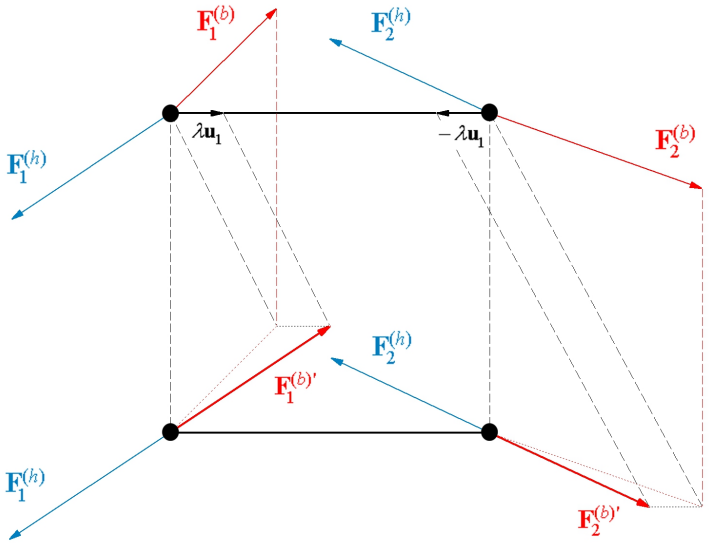

Figure 2.17: Example of the geometrical projection of Brownian forces in a quiescent bi-dimensional single rigid-rod (no external-flow). An isotropic friction coefficient is supposed. In the upper rod no geometrical projection has been carried out, hence tension force is considered. In the lower rod, geometrical projection of Brownian forces absorbs the rod tension; observe that hydrodynamic forces are not modified

Geometrical projection of random forces on multi-bead-rod chains is absolutely required when the multi-bead-spring statistics want to be mimicked (use of corrective potential forces) or an anisotropic friction tensor is considered [142].

External forces acting on bead i, $\mathbf{F}_i^{(e)}$

As mentioned before, gravitational and electromagnetic forces can be considered in function of the particular scenario of modelling. In this work, external forces are neglected.

Taking into account that inertia is neglected, forces balance on each bead i writes:

$$\mathbf{F}_i^{(h)} + \mathbf{F}_i^{(\lambda)} + \mathbf{F}_i^{(\phi)} + \mathbf{F}_i^{(b)'} + \mathbf{F}_i^{(e)} = \mathbf{0} \tag{2.79}$$

Given the definition of the hydrodynamic drag force, an explicit stochastic expression for the bead velocity can be obtained:

$$\frac{d\mathbf{r}_i}{dt} = [\boldsymbol{\kappa}(\mathbf{r}_i) \cdot \mathbf{r}_i] - \frac{1}{\zeta}\left\{\left(\sum_{j=1}^{n-1} \mathbf{n}_{ij}\lambda_j\right) - \mathbf{F}_i^{(\phi)} - \mathbf{F}_i^{(b)'} - \mathbf{F}_i^{(e)}\right\} \tag{2.80}$$

Geometrical projected random forces guarantee the inextensibility condition when no external fields are imposed. In other scenario, constraints on the rod lengths have to be considered. For instance, in a Cartesian coordinates system we have:

$$0 = \sum_{i=1}^{n} \dot{\mathbf{r}}_i \cdot \mathbf{n}_{ij} \qquad \text{for} \quad j = 1 : n-1 \tag{2.81}$$

Putting together Eqs. (2.80) and (2.81) a linear system of equations describing the kinematics of a non-freely-jointed multi-bead-rod model is constituted, where the unknown variables are n bead velocities $\dot{\mathbf{r}}_i$ and $n-1$ rod tensions λ_j.

2.5.2 Integration Schemes

Several numerical integration schemes have been proposed to integrate the differential stochastic equation equivalent to the FP equation given by Curtiss for the general multi-bead-rod chain in both generalized coordinate systems and Cartesian reference systems. In the case of generalized coordinates, the task is feasible if the number of degrees of freedom is small, otherwise the numerical complexity makes this option impractical [149]. Some simulations at equilibrium using a numerical integration in generalized coordinates were made by Pear and Weiner [212, 151]. The possibilities for integrating numerically in a Cartesian space are more varied and, in principle, the numerical methods employed for the bead-spring models are applicable, but additional controls are required for satisfying the constraints rigorously, specially in simulations for large time intervals [149].

Another integration numerical method for systems including constraints was given by Allison and McCammon under the name of SHAKE-HI algorithm [219]. In the general form of the algorithm, bead positions are calculated in two steps: an unconstrained step followed by a constrained one. It is the opinion of the author that two particular versions of the SHAKE-HI algorithm are the most cited numerical schemes employed to integrate the differential stochastic equation for a multi-bead-rod model in a Cartesian space: the mid-point stepping scheme proposed by Fixman [213, 216] and the predictor-corrector scheme developed by Liu [207, 193].

Mid-Point Algorithm

In 1978 Ermak and McCammon showed that the gradient of the diffusivity must to be incorporated into a BD algorithm when the bead diffusivity depends on the configuration of the Brownian system [220]. It has been shown that the diffusivity of a multi-bead-rod chain is variable because of the presence of rigid constraints and, also, as consequence of considering hydrodynamic interaction [216]. A clever way to counteract the wrong drift produced by the variable diffusivity in a BD algorithm was proposed by Fixman [213]. He suggested employing a second-order time step to integrate the stochastic differential equation. In fact, any higher order time step is able to handle correctly the variable diffusivity. In this numerical algorithm the use of potential metric forces $\mathbf{F}_i^{(m)}$ is required and has to be added to the left term of Eq. (2.79). From a global point of view, this algorithm is able to deal with hydrodynamic interaction and anisotropic friction tensors. Now, for the particular multi-bead-rod chain tackled in this work, the differential stochastic equation required for the mid-step scheme writes as follows:

$$\dot{\mathbf{r}}_i = \frac{1}{\zeta}\left(\mathbf{F}_i^{(\lambda)} + \mathbf{F}_i^{(uc)} + \mathbf{F}_i^{(b)'}\right) \tag{2.82}$$

where $\mathbf{F}_i^{(uc)} = \zeta\left[\boldsymbol{\kappa}\left(\mathbf{r}_i\right)\cdot\mathbf{r}_i\right] + \mathbf{F}_i^{(\phi)} + \mathbf{F}_i^{(e)} + \mathbf{F}_i^{(m)}$. Keeping in mind that hydrodynamic interaction is neglected and an isotropic friction tensor is supposed, then a single time step $[t,\, t+\Delta t]$ for the mid-step algorithm is constituted by the following sub-steps:

1. Generation of geometrical projected random forces at the beginning of the time step $\mathbf{F}_i^{(b)'}(t)$ following the complete algorithm describe by Hinch and co-workers [215, 216, 217].

2. Calculate the mid-step position as follows:

$$\mathbf{r}_i\left(t+\frac{\Delta t}{2}\right) = \mathbf{r}_i(t) + \dot{\mathbf{r}}_i(t)\,\frac{\Delta t}{2} \tag{2.83}$$

   where the initial-step velocity $\dot{\mathbf{r}}_i(t)$ is calculated neglecting the constraints on the rod lengths:

$$\dot{\mathbf{r}}_i(t) = \frac{1}{\zeta}\left(\mathbf{F}_i^{(uc)}(t) + \mathbf{F}_i^{(b)'}(t)\right) \tag{2.84}$$

3. Calculate the end-step position by using the next equation:

$$\mathbf{r}_i(t+\Delta t) = \mathbf{r}_i(t) + \dot{\mathbf{r}}_i(*)\,\Delta t \tag{2.85}$$

   where the mid-step velocity is obtained from the solution of the linear system:

$$\dot{\mathbf{r}}_i(*) = \frac{1}{\zeta}\left[\mathbf{F}_i^{(\lambda)}\left(t+\frac{\Delta t}{2}\right) + \mathbf{F}_i^{(uc)}\left(t+\frac{\Delta t}{2}\right) + \mathbf{F}_i^{(b)'}(t)\right] \tag{2.86}$$

$$0 = \sum_{i=1}^{n} \dot{\mathbf{r}}_i (*) \cdot \mathbf{n}_{ij} \left(t + \frac{\Delta t}{2} \right) \tag{2.87}$$

where $\dot{\mathbf{r}}_i (*)$ is the constrained bead velocity at the mid-step, but calculated with the random stochastic forces generated at the beginning of the time step. This procedure is coherent with the Stratonovich interpretation of the stochastic random forces [149, 221]. This algorithm does not guarantee an invariable rod length at the end of the time step, for that reason a truncation error is employed. Once the rod length at the end of a given time step exceeds certain tolerance, the inter-bead distances are reset to the constant value, conserving the rod orientations.

Predictor-Corrector Scheme

The predictor-corrector scheme is a singular and limiting case of the SHAKE-HI algorithm. One can say that is singular because it requires absolutely neglecting the hydrodynamic interaction and dealing with an isotropic friction tensor. On the other hand, this algorithm is limiting because the two-step procedure is merged in an iterative single-step. The predictor-corrector scheme was employed by Liu for simulating the dynamics of a Kramers chain submitted to steady potential flows [207]. Doyle demonstrated that both the predictor-corrector scheme and the Fixman's mid-step algorithm generate the same trajectories for a dilute Kramers bead-rod chain with an isotropic friction tensor and in absence of hydrodynamic interaction [221]. It is emphasized that neglecting the hydrodynamic interactions, supposing an isotropic friction tensor and employing this limiting case of the SHAKE-HI algorithm are necessary conditions for eliminating the metric potential forces from the differential stochastic equation in Cartesian coordinates without incurring in deviations from the FP equation for the multi-bead-rod model [149].

For a time step $[t, t + \Delta t]$, displacement of bead i is obtained in two stages. The first one, called predictor step, is given by an unconstrained movement:

$$\mathbf{r}_i^* (t + \Delta t) = \mathbf{r}_i (t) + \dot{\mathbf{r}}_i (t) \Delta t \tag{2.88}$$

where $\dot{\mathbf{r}}_i (t) = \frac{1}{\zeta} \left(\mathbf{F}_i^{(uc)} (t) + \mathbf{F}_i^{(b)'} (t) \right)$ and $\mathbf{F}_i^{(uc)} = \zeta \left[\boldsymbol{\kappa} (\mathbf{r}_i) \cdot \mathbf{r}_i \right] + \mathbf{F}_i^{(\phi)} + \mathbf{F}_i^{(e)}$. Subsequently, an iterative corrector step is required for taking into account the inextensibility of rods:

$$\mathbf{r}_i (t + \Delta t) = \mathbf{r}_i^* (t + \Delta t) + \frac{1}{\zeta} \mathbf{F}_i^{(\lambda)} \Delta t \tag{2.89}$$

where $\mathbf{F}_i^{(\lambda)}$ is given by Eq. (2.67). The Langrange multipliers (rod tensions) λ_j are calculated so that inter-bead distances are satisfied within a certain tolerance:

$$\left(\mathbf{r}_{i+1} (t + \Delta t) - \mathbf{r}_i (t + \Delta t) \right)^2 - a^2 = \varepsilon^2 \tag{2.90}$$

Combining Eqs. (2.89) and (2.90), a system of quadratic equations for λ_j is generated. This system has the general form:

$$\begin{aligned}&\frac{2\Delta t}{\zeta}\mathbf{b}_i \cdot \left(\lambda_{i-1}^{(n)}\mathbf{u}_{i-1} - 2\lambda_i^{(n)}\mathbf{u}_i + \lambda_{i+1}^{(n)}\mathbf{u}_{i+1}\right) = a^2 + \phi^2 - \\ &\mathbf{b}_i \cdot \mathbf{b}_i - \left(\frac{\Delta t}{\zeta}\right)^2 \left(\lambda_{i-1}^{(n-1)}\mathbf{u}_{i-1} - 2\lambda_i^{(n-1)}\mathbf{u}_i + \lambda_{i+1}^{(n-1)}\mathbf{u}_{i+1}\right)^2\end{aligned} \tag{2.91}$$

where $\mathbf{b}_i = \mathbf{r}_{i+1}^* - \mathbf{r}_i^*$. Previous set of non-linear equations can be resolved iteratively by a Picard's method by supposing the non-linear term (last term on the right-hand side) to be small in comparison with the linear terms (left-hand side). The iterative procedure is initiated with $\lambda_i^{(0)} = 0$ and is executed until the constraints are satisfied with regard to a certain truncation error ε^2. Once the iterative procedure has finished, the bead positions at the end of the time step are corrected using Eq. (2.89).

Additional to the Picard's method invoked to solve Eq. (2.91), an iterative Newton's method can converge faster than the Picard's one, but involving the calculation of a Jacobian matrix at each iteration [193].

2.5.3 Stress Tensor Calculation

From a formal point of view, deduction of a stress formula for bead-rod chains is not as straightforward as in the case of bead-spring models, where the physical configuration is an intimate reflect of the instantaneous mechanical state of the system. In the case of bead-rod chains, the pictorial arguments used for the bead-spring models are not enough and, in consequence, a deeper physical explanation is required.

There is a general consensus accepting that the modified Kramers expression (Eq. 2.45) accounts for the contribution to the total shear stress coming from a diluted model system whose total change in momentum can be discretized on certain points, as is the case for a general bead-rod-spring model. A detailed derivation of this stress tensor formula using a general *phase-space* kinetic theory can be examined in [141].

Care must be taken also when calculating numerically the stress tensor for systems containing constraints. Given the numerical singularities originated by the presence of constraints, one is particularly interested in the correct implementation of a stress tensor formula into the BD algorithm. It is found that a correct estimation of the stress tensor must to be closely linked to the integration scheme used in the simulation.

One can recognize two main contributions to the stress tensor coming from bead-rod chains: one given by the random forces and another one given by the viscous effects. In order to account rigorously for the Brownian contribution, the algorithm estimating the stress tensor must to consider the discontinuity of the Brownian forces during a given time step [217, 221], specially when no-flow conditions are being simulated. To do this, the modified Kramers formula has to be interpreted as an average in time. For a mid-step algorithm, for example, the average has to be carried out using the beginning and the end

of the time step [222]:

$$\boldsymbol{\tau}_p(t) = \frac{c}{2}\sum_{v=1}^{n}\left\langle \mathbf{R}_v(t)\otimes\mathbf{F}_v^{(h)}(t) + \mathbf{R}_v(t+\Delta t)\otimes\mathbf{F}_v^{(h)}(t+\Delta t)\right\rangle \tag{2.92}$$

Doyle demonstrated that two iterations of the predictor-corrector scheme producing an increment of Δt are equivalent to one time-step of the mid-step algorithm [221]. Based on the previous fact, it can be easily showed that Eq. (2.92) is also a correct interpretation of the virial tensor for the predictor-corrector algorithm.

An alternative way to correctly account for the Brownian contribution in a first order integration scheme (as the predictor-corrector algorithm), considering a "long-lasting" action of the random forces, can be envisaged using the next algorithm:

1. Update the bead-rod position by executing one explicit time step from t to $t+\Delta t$.
2. Using the same Brownian forces used at time t, recalculation of the hydrodynamic drag forces $\tilde{\mathbf{F}}_v^{(h)}(t+\Delta t)$ with the updated configuration at $t+\Delta t$.
3. Determination of the shear-stress tensor at time t by computing:

$$\boldsymbol{\tau}_p(t) = c\sum_{v}\left\langle \mathbf{R}_v(t+\Delta t)\otimes\tilde{\mathbf{F}}_v^{(h)}(t+\Delta t)\right\rangle \tag{2.93}$$

Giesekus formula for the stress tensor has also been recursively used in the BD simulations of multi-bead-rod models [207, 193]:

$$\boldsymbol{\tau}_p(t) = -\frac{c\zeta}{2}\sum_{v}\langle \mathbf{R}_v(t)\otimes\mathbf{R}_v(t)\rangle_{(1)} \tag{2.94}$$

where the quantity $\langle\ldots\rangle_{(1)}$ denotes the convected derivative defined as follows:

$$\mathbf{X}_{(1)} = \frac{d}{dt}\mathbf{X} - \left\{\boldsymbol{\kappa}^T\cdot\mathbf{X} + \mathbf{X}\cdot\boldsymbol{\kappa}\right\} \tag{2.95}$$

However, it has been showed that the usefulness of this expression is restricted to the equilibrium and steady-flow conditions [221, 193].

2.5.4 The *Trimer* Chain

In order to study the generalities of the BD simulations for multi-bead-rod models it was decided to use the freely-jointed (three-bead)-(two-rod) model, also known as the *trumbbell* or *trimer* system. This model is composed of three beads with isotropic friction coefficient ζ connected by two freely jointed rigid mass-less rods of length a. Hydrodynamic interaction is neglected.

Trimer chain is a better testing model than the rigid dumbbell because a more rigorously evaluation of the integration algorithms can be carried out given the presence of two adjacent constraints. On the other hand, an exact numerical expression for the dynamic

response of a dilute solution of *trimer* systems was obtained separately by Fixman and Hassager [223, 208]. This numerical solution is in coherence with the FP equation for a multi-bead-rod chain in polymer kinetic theory [197, 141], actually deviated from that one for multi-bead-spring chains [211]. In the Hassager's solution, dynamic modulus of the *trimer* system is described using four relaxation times of which the longest one writes:

$$\tau_1 = \frac{\zeta a^2}{5.4376 k_B T} \tag{2.96}$$

With the aim of compare properly with the BD predictions, time for the theoretical data is rescaled using the main relaxation time found by Hassager.

Given that hydrodynamic interaction is neglected and an isotropic friction tensor is supposed, a first-order integration scheme in coherence with the predictor-corrector algorithm is implemented and the shear-stress tensor contribution is estimated with the modified Kramers-Kirkwood expression using the "long-lasting" Brownian forces algorithm. In this context, metric potential forces are not required for maintaining the coherence with the FP equation for Kramers chains. A bi-dimensional modelling is used with the aim of reduce the computational cost. Distance between beads a is employed as the characteristic length of the problem. Time scale in the BD simulations is made dimensionless using the longest relaxation time (or rotational diffusion time) of an equal-length multi-bead rigid-rod system given by [141]:

$$\lambda_n = \frac{\zeta L^2 n\,(n+1)}{72\,(n-1)\,k_B T} \tag{2.97}$$

It means that for a *trimer* system, where $n = 3$, time is scaled using $\lambda_3 = \zeta a^2 / 3 k_B T$. Time step, instead, needs to be scaled with regard to the fastest relaxation time; in the case of bead-rod chains, the bead diffusion time is normally used, $\lambda_{bead} = \zeta a^2 / k_B T$.

As showed in the analysis of the Hookean-dumbbell model (§2.4.4), the BD considerations when estimating the equilibrium properties (in absence of flow) are analogues to those ones obtained under linear dynamic solicitation at the characteristic frequency, i.e. at $\omega_R = 1$. For that reason, no-flow properties are skipped and the linear dynamic response of the system is tackled directly.

BD simulations of the small-amplitude oscillatory deformation tests are carried out according to the algorithm explained in §2.3.1. First of all, the limit of the linear viscoelastic regime needs to be determined. In order to extract this information from the BD simulations, the norm of the complex modulus at the characteristic frequency is plotted in function of the maximal applied strain. In order to marginalize the numerical issues of the BD simulation, a population 10^4 chains and a time step equivalent to $\lambda_{bead}/10^5$ are employed.

Figure 2.18 shows that the limit of the linear viscoelastic regime for a dilute solution of *trimer* systems corresponds to a maximal deformation $\gamma_0 \approx 1.33a$. At lower values, dynamic moduli obtained by BD simulations are independent of the maximal deformation

imposed. On the other hand, Fig. 2.18 evidences that multi-bead-rod models exhibit a shear-thinning behaviour, contrary to the multi-bead-spring counterparts. Using a constant BD population (10^4 *trimers*) and a constant time step ($\lambda_{bead}/10^5$), computational time (2× Quad-Core AMD Opteron^{TM} 2376 (2300 MHz)) employed to predict the complex modulus at $\omega_R = 1$ was found 8.7 times longer than the computational time used at $\omega_R = 10^2$. This fact is explained by the longer analytical steps required at low frequencies for determining the maximal shear-stress and phase angle between the strain and stress signals.

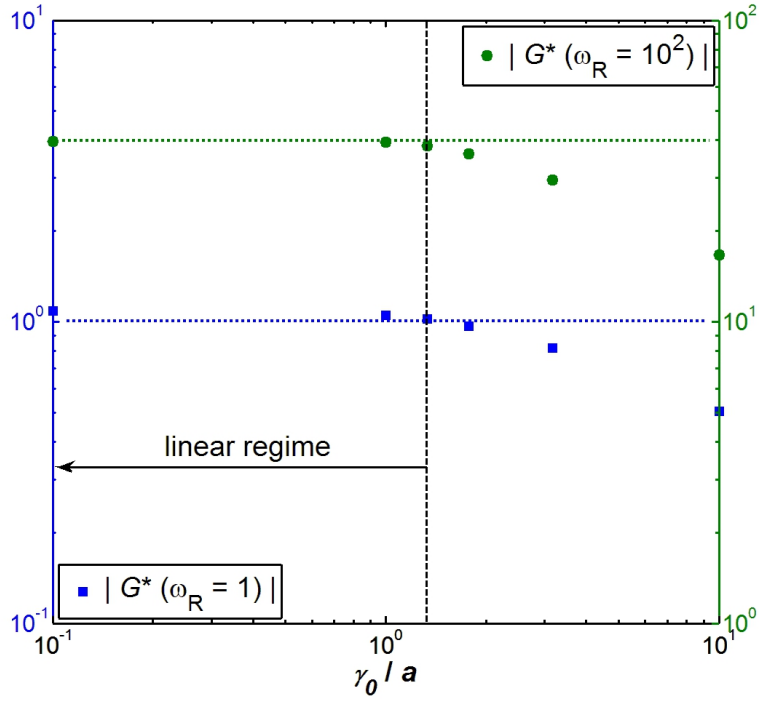

Figure 2.18: Identification of the limit of the linear viscoelastic regime for a dilute suspension of *trimers* by BD simulation. Absolute value of the complex modulus in function of the maximal deformation applied for two reduced frequencies: $\omega_R = 1$ (on the left y-axis) and $\omega_R = 10^2$ (on the right y-axis). Horizontal pointed lines correspond to the theoretical values calculated by Hassager. Dashed vertical line marks the limit of the linear viscoelastic regime

In the current BD approach, a first-order integration scheme was implemented and, therefore, time step strongly influences the convergence of the simulation towards the central values. In Fig. 2.19 the effect of the time step on the convergence of the BD simulation is presented (from now on, imposed maximal deformation is chosen inside the linear viscoelastic regime). 10^4 *trimers* were employed as BD system in order to reduce the distortions coming from the random number generation. Convergence of the BD simulation is tested in three different flow scenarios: $\omega_R = 1$, which is representative of the thermal-to-flow induced transition, $\omega_R = 10^2$, which is characteristic of the mild flow-induced regime, and, $\omega_R = 10^3$, which is typical of a strongly flow-induced regime.

In Fig. 2.19 is clearly observed the strong influence of the length of the time step in

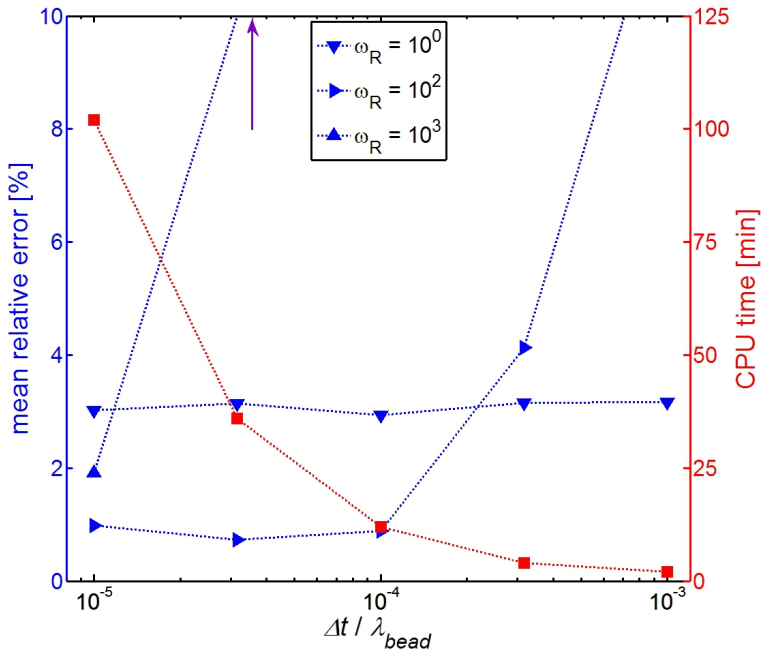

Figure 2.19: Mean relative error of the BD prediction for the complex modulus (left y-axis) and CPU time (right y-axis) in function of the time step. Mean relative error is the average of the relative errors for storage and loss modules. Relative error is defined as follows: $|(\log G'_{BD}(\omega_R) - \log G'_{th}(\omega_R)) / \log \Theta|$, where $\Theta = G''_{th}(\omega_R = 10^3) / G'_{th}(\omega_R = 1)$ is the maximal interval of complex modulus variation in the tested frequency interval. CPU time corresponds to the total simulation time required to predict the complex modulus for the three tested frequencies. A population of 10^4 *trimers* has been employed

the convergence of the explicit integration scheme at high frequencies. At low frequencies ($\omega_R = 1$), characteristic of the thermal-induced regime, BD performance (relative error $\sim 3\%$) is nearly independent of the length of the time step. In this regime, convergence of the integration scheme is guaranteed with a time step equal to $\lambda_{bead} \cdot 10^{-3}$. Error obtained at this flow regime is mainly coming from the random number generation algorithm; implementation of a more sophisticated generator is necessary to reduce this noise. When increasing the frequency, BD performance is progressively more affected by the integration scheme. As showed for the multi-bead-spring models, at higher frequencies than the characteristic one, the flow-induced forces control the kinematics of the system; for that reason, higher velocities require smaller time steps in order to guarantee a correct numerical integration. This fact is clearly captured in Fig. 2.19: in the mild flow-induced regime, i.e. $\omega_R = 10^2$, mean relative error of the BD prediction goes from 1% to 12% when the length of the time step is enlarged from $\lambda_{bead} \cdot 10^{-5}$ to $\lambda_{bead} \cdot 10^{-3}$. On the other hand, in the strong flow-induced regime, i.e. $\omega_R = 10^3$, mean relative error of the BD prediction explodes from 2% to more than 20% when the length of the time step is augmented just in one-half order of magnitude from $\lambda_{bead} \cdot 10^{-5}$. Simulation time is proportionally reduced as the length of the time step is enlarged. It is more valuable to mention that the computational time devoted for a given frequency strongly depends on the position inside the frequency spectra; for example, the relative contributions to the total simulation times in Fig. 2.19 are 61%, 8% and 31% for the predictions at the reduced frequencies of 1, 10^2 and 10^3 respectively. Simulation at the characteristic frequency has the biggest computational cost because it requires the longest analytical stage. On the other hand, simulation at the highest frequency is also time-consuming because the stabilization stage requires a refining of the nominal time step in order to guarantee a stable dynamic configuration before beginning the analytical step.

In what follows, an extended sweep test over 21 frequencies homogeneously distributed within an interval of reduced frequencies going from 10^{-2} to 10^3 was used to evaluate the global performance of the implemented BD simulation predicting the linear dynamic response of a *trimer* system in dilute solution. A time step equal to $\lambda_{bead} \cdot 10^{-5}$ has been employed with the purpose of guarantee the best convergence of the integration scheme inside the simulated frequency range. In Fig. 2.20 the Hassager's numerical solution is properly compared with the BD predictions for the frequency sweep test. Hassager's complex modulus is presented in a reduced frequency scale $\omega_R = \omega\tau_1$, and BD results are plotted in a reduced frequency scale $\omega_R = \omega\lambda_3$, where λ_3 is the rotational diffusion time for a (three-bead)-(rigid-rod) system of equal length.

It is observed in Fig. 2.20 that the BD algorithm yielded a complex modulus in good agreement with the Hassager's numerical solution of the *trimer* system. On the other hand, this large-sweep simulation demonstrated that the bi-dimensional modelling is coherent with the Hassager's results and, therefore, it was not necessary to implement the three-dimensional modelling, which would be more expensive in computational time. Two different regions are clearly differentiated in the dynamic response of a freely-jointed (three-

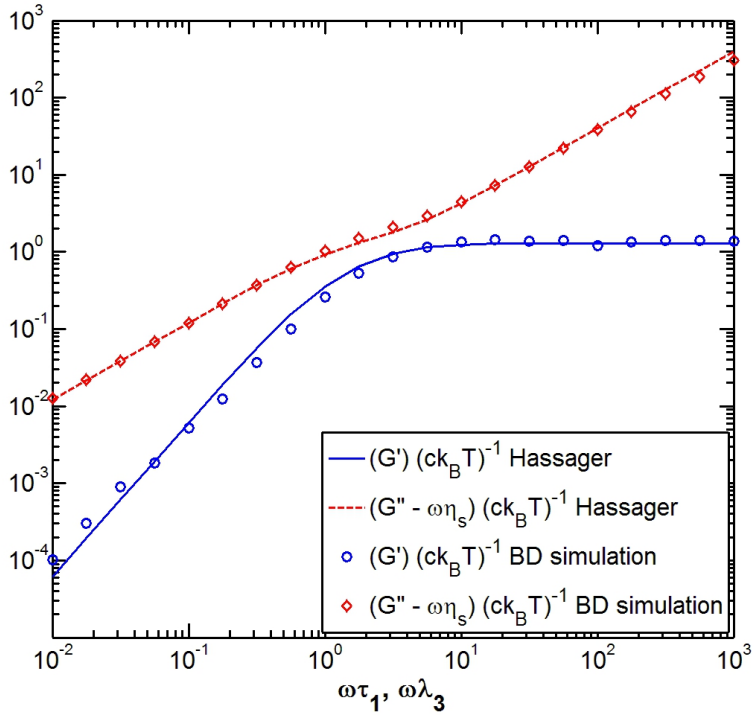

Figure 2.20: Dynamic modulus of a freely jointed (three-bead)-(two-rod) system in a proper reduced frequency scale: comparison between the Hassager's numerical solution and the current BD simulation. τ_1 is the main relaxation time in the Hassager's solution and λ_3 is the rotational diffusion time of a (three-bead)-(rigid-rod) system of equal length. $c = a = \zeta = 1$, $k_BT = 0.1$, and $K_b = 0$ are the BD parameters

bead)-(two-rod) system: a low frequency regime exhibiting a typical Maxwell terminal behaviour, where the thermal activity (or Brownian forces) drives the kinematic of the system; and a high frequency regime, where the domination of flow forces over the diffusivity terms produces a plateau for the storage modulus and a limiting constant viscosity $(G(\omega)/\omega) - \eta_s$ larger than zero. The existence of a non-zero limiting viscosity is physically more coherent than the classical responses of multi-bead-spring chains, where the model contribution to the dynamic viscosity disappears at high frequencies.

As already mentioned in the section devoted to the bead-spring models, the number of entities (or trajectories) plays a fundamental role in the performance of the BD simulations. Performance of the global simulation in function of the BD population is presented in Fig. 2.21. The performance of the BD simulation is measured in terms of the mean of the relative errors for 17 storage modulus values homogeneously distributed in an interval of reduced frequencies going from 10^{-2} to 10^{2}. Loss modulus signature was found practically insensitive to the BD population; mean relative error for the loss modulus signal was equal to 0.3%.

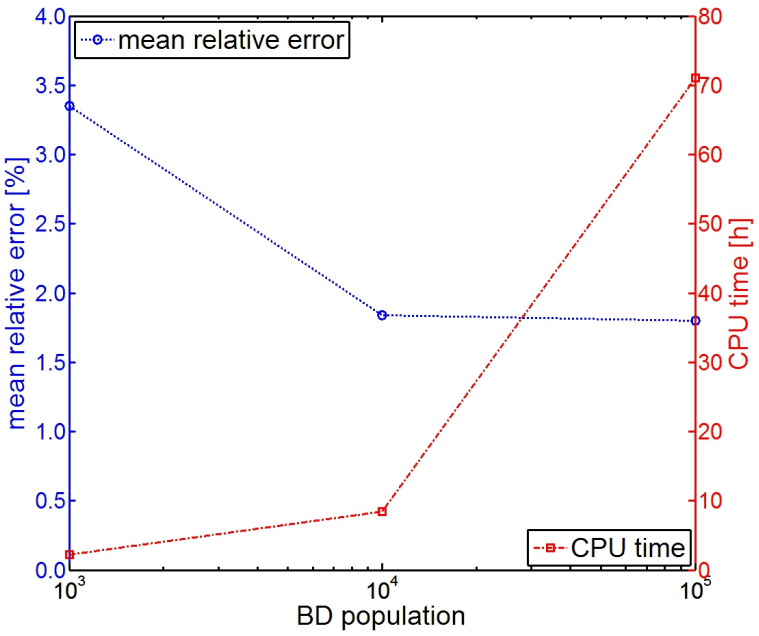

Figure 2.21: Mean relative error of the storage modulus prediction (for a *trimer* system) and total computational time in function of the BD population. Mean relative errors are calculated as the average of 17 points distributed homogenously in a reduced frequency range going from 10^{-2} to 10^{2}. Relative error is calculated as follows: $|(\log G'_{BD}(\omega_R) - \log G'_{th}(\omega_R))/\log\Theta|$, where $\Theta = G''_{th}(\omega_R = 10^2)/G'_{th}(\omega_R = 10^{-2})$ is the maximal interval of complex modulus variation in the tested frequency interval

As expected, a linear evolution of the computational time (2 × Quad-Core AMD Opteron^{TM} 2376 (2300 MHz)) in function of the number of *trimers* simulated is checked. It was corroborated that a population of 10^4 systems guarantees a good compromise between computational time and rheological prediction performance.

Chapter 3

BD on Linear Viscoelasticity of SWNT Suspensions

This chapter constitutes the meeting point of the two first ones. On the one hand, in Chapter 1 the necessity of enrich the physical description of the models employed at present for mimicking the mechanical structure of individual single-walled CNTs (SWNTs) in dilute solution was highlighted, given the lack of understanding for explaining the linear viscoelastic behaviour of dilute suspensions of treated SWNTs within a Newtonian solvent. On the other hand, in Chapter 2 the validation of a Brownian dynamics (BD) approach for simulating the linear viscoelastic response of a dilute suspensions of a given micro-mechanical model has prepared the modelling framework for evaluating a more realistic physical model of a functionalized SWNTs in dilute solution.

Hence, in the current chapter a coarse-grained model is formulated for a SWNT based mainly in two physical aspects: structural topological defects and bending flexibility; considered by the author as key factors controlling the dynamic response of an individual SWNT. Some details concerning the implementation of a BD simulation for this particular model are also exposed. Finally, a complete analysis of the BD-simulated linear viscoelastic response of diluted suspensions of treated SWNTs is deployed in two classical strain function scenarios: small-amplitude oscillatory deformation and relaxation after a shear-strain step.

3.1 A Coarse-Grained Model for a SWNT

SWNTs can contain naturally topological defects [224]. Several studies have showed the existence of those defects by using Fresnel projection microscopy [225], scanning tunnelling microscopy (STM) [226] and voltage-contrast scanning electron microscopy (VC-SEM) [227]. Most common topological defects in SWNTs are due to the existence of a non-hexagonal carbon ring (e.g. pentagon-heptagon defect) in middle of the classical honeycomb-like lattice structure of a CNT. Molecular dynamics (MD) is largely employed to identify the structural consequences of this kind of defects. For example, it has been

demonstrated that a bent structure is thermodynamically more stable than a straight one once a localized topological defect appears in the SWNT growth [228]. Additionally, it has been shown that a single pentagon-heptagon pair can bend the SWNT tubular structure forming a localized junction [229] with angles varying from 0° to 34° [230, 231], depending on the distance between the pentagon and heptagon pair defect [232].

Persistent length l_p considerations are necessary when modelling high aspect ratio systems that exhibit a very important resistance to tangential extension or compression [143, 144]. In absence of external forces (e.g. a flow field), persistent length is a characteristic length that relates the bending rigidity of the system to the thermal energy around it. In practice, this parameter determines a length scale over which the high aspect ratio system presents significant curvature due to the thermal interactions with the surroundings. In consequence, a system of total length L where $L/l_p << 1$ can be considered as a simple rigid rod and a system where $L/l_p >> 1$ can be considered as a flexible filament. Traditionally, individual SWNTs have been modelled as Brownian rigid-rods [14, 233, 171, 122].

Nevertheless, there are experimental results that lead to think that treated SWNTs can be considered as other than rigid-rod systems. Using a near-infrared fluorescence technique, thermal SWNT-shape fluctuations have been observed into a diluted SWNT aqueous suspension [234]. Additionally, the observed bending dynamics was accurately correlated with a semi-flexible filament model ($L \sim l_p$), where l_p scales with the d^3 (d: diameter of SWNT) [17].

If we are considering now the action of an external flow field and the natural existence of a bent structure in SWNTs, due to the presence of side-wall defects, the concept of persistent length requires a more precise definition. In any case, those new considerations can only reduce the length scale of observable bending relative to the thermal classical persistent length and, hence, in this work a semi-flexible filament is supposed to be a good equivalent micro-mechanical model for describing the dynamics of an individual SWNT submitted to a homogeneous external-flow field.

In this context, emphasis is made on considering that a SWNT contains naturally side-wall defects producing a deviation from the perfectly straight structure; i.e. the pristine SWNT has a slightly curved structure. This assumption is supported on two main facts:

1. Even if there is a large discussion about the influence of sample preparation on the observed structure of CNTs, there are numerous images taken by SEM, STM, atomic force microscopy (AFM) and transmission electron microscopy that reveal clearly a natural bent structure in some CNT samples [235, 226, 236, 237, 238, 227]. For example, in Fig. 3.1 an image taken by AFM of surface-treated SWNTs protruding from a photo-cured acrylic surface is presented; the bent structure of the SWNTs is easily appreciable.

2. The natural existence of topological defects that plays an important role in the mechanical and thermo-electrical properties of CNTs [24]. A clear relationship between those CNT structural instabilities (pentagon/heptagon defect, for example) and the

intrinsic curvature of CNT structures has been established [15, 16, 229, 230, 235, 232, 239, 231, 228].

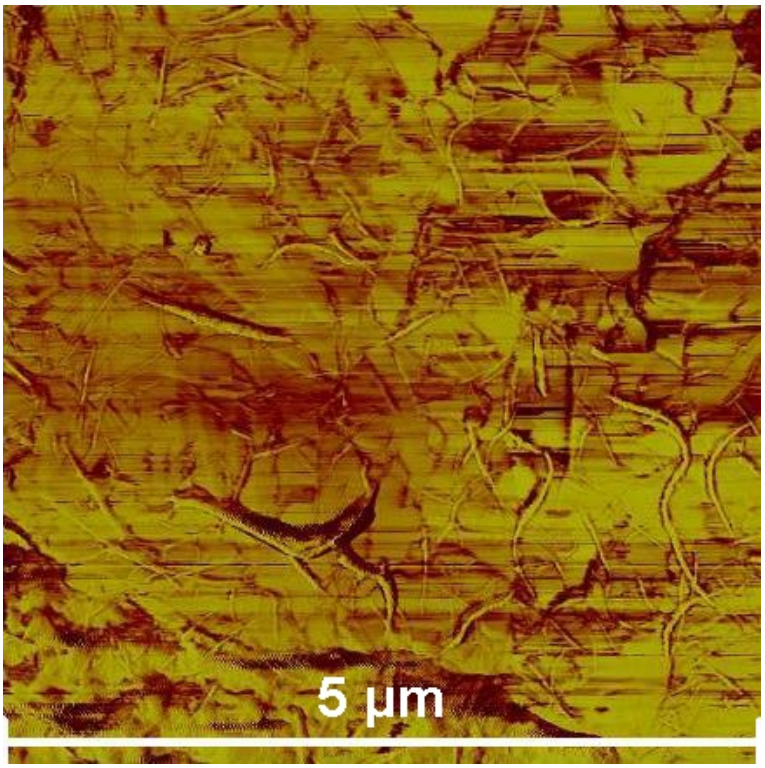

Figure 3.1: AFM image of SWNTs protruding from a photo-cured acrylic surface (Image area corresponds to a 5 μm-side square). Courtesy of Dr. Anson Ma (Rice University), Dr. Loren Picco (Bristol University) and Pr. Mervyn Miles (Bristol University)

In order to test the dynamic mechanical response of this physical model in a BD approach, the semi-flexible filament is discretized in a non-freely jointed multi-bead-rod model as showed in Fig. 3.2. This multi-bead-rod model is composed of n beads with positions $\mathbf{r}_i$, connected by $n-1$ rods of length a, where a approaches theoretically the persistence length under flow conditions of the system. The physical length of the SWNT is given by the total length of the multi-bead-rod model: $(n-1)a$. Beads are considered the centres of hydrodynamic resistance, as usual for all the mechanical models in *polymer* kinetic theory [141], and also mark the existence of a bent topological defect. On the other hand, rods are supposed infinitely rigid. The existence of an internal bending potential that mimics the SWNT bending flexibility is taken into account. Bending potential is given by the action of a hypothetical torsion spring between each pair of rods.

Given the stiffer bending rigidity of the CNT structure in comparison with the rigid rod-like polymers, which are mimicked by a similar micro-mechanical model, the modelling of a SWNT is supposed to be restricted to a low number of rods ($n < 10$). Current modelling approach supposes also an isotropic friction tensor.

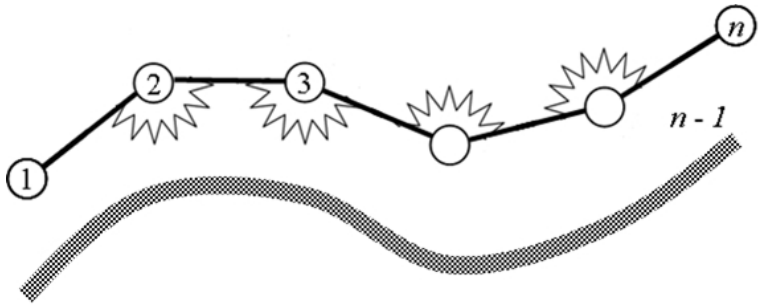

Figure 3.2: Non-freely jointed multi-bead rod model composed of n beads and $n-1$ rods of length a. Bending potential between rods in the multi-bead rod model is mimicked with a hypothetical torsion spring. An equivalent continuous semi-flexible filament is depicted below the discritized model

3.2 BD Issues of the Modelling of SWNT Suspensions

Simulation of the linear viscoelastic response for a dilute suspension of non-freely jointed multi-bead-rod chains is subjected to the next hypotheses:

- Rheological tests occur at constant temperature.
- Individual SWNTs are embedded into a Newtonian matrix of viscosity η_s.
- Suspension is supposed to be diluted, in consequence, no physical interaction between SWNTs is considered.
- Applied flow field is considered homogeneous at the scale of the multi-bead-rod chain, i.e. rate-of-strain tensor is supposed constant at length scales below twice the contour lenght of the chain.
- Due to the small deformations involved in the linear viscoelastic regime and the relative high bending stiffness of a SWNT, no hydrodynamic interaction is taken into account.
- No external forces (e.g. electrostatic, magnetic or gravitational) play a role in the dynamics of the suspension. For instance, electrostatic interactions between surface-treatment groups are neglected because it was demonstrated that those repulsion forces do not produce an increment of the storage modulus at high frequencies [126].

Formal kinematic formulation for this micro-mechanical model was already given in §2.5.1. The only precision required is concerning the internal bending-potential forces because a redefinition of the energy-potential is necessary for taking into account the natural bent configurations.

Bending potential defined in Eq. (2.69) is based on the worm-like chain continuous model. It this model, the equilibrium configuration corresponds to a perfectly straight

chain; in other words, the minimum value of bending potential energy is associated with a multi-bead-rod chain whose unitary rod vectors $\mathbf{u}_j$ are all the same. Bending potential force acting on bead k can be easily deduced as the derivative of the discrete bending potential with respect to the position of bead k (Eq. 2.70). Appendix A shows that the total bending force acting on bead k only depends on the local chain configuration and that this force can be interpreted as the sum of independent contributions coming from all the two-rod sub-sections containing bead k.

However, in the current modelling, a SWNT is supposed to be a finite-contour-length high-aspect-ratio systems with non-straight configurations at equilibrium and, therefore, a redefinition of the discrete bending potential taking into account a natural bent configuration is required. In this context, a suitable redefinition of the discrete bending potential for a multi-bead-rod model with a naturally bent configuration at equilibrium can be expressed in the next way:

$$\phi = -\frac{K_b}{a}\sum_{i=2}^{n-1}\mathbf{Z}_i\mathbf{u}_i\cdot\mathbf{u}_{i-1} = -\frac{K_b}{a}\sum_{i=2}^{n-1}\mathbf{u}'_i\cdot\mathbf{u}_{i-1} \tag{3.1}$$

where $\mathbf{Z}_i$ is a linear operator that counter-rotates vector $\mathbf{u_i}$ of $\Delta\theta^0_{i,i-1}$ (interior angle between $\mathbf{u_i}$ and $\mathbf{u_{i-1}}$ at the equilibrium configuration) and $\mathbf{u}'_i$ is the rotated vector $\mathbf{Z}_i\mathbf{u}_i$. In an analogous way with the straight case, bending force coming from the potential in Eq. (3.1) takes the next form:

$$\mathbf{F}^{\phi}_k = -\frac{\partial\phi}{\partial\mathbf{r}_k} = \frac{K_b}{a}\sum_{i=2}^{n-1}\frac{\partial\left(\mathbf{u}'_i\cdot\mathbf{u}_{i-1}\right)}{\partial\mathbf{r}_k} \tag{3.2}$$

Considering that the total bending force in Eq. (3.2) can also be interpreted as the sum of independent contributions coming from all the two-rod sub-sections containing bead k, as shown in Appendix A, the next algorithm is proposed for computing the total bending forces in coherence with the naturally bent configuration:

1. Decomposition of the multi-bead-rod (n beads) system into $n-2$ sub-section of two consecutive rods as shown in Fig. 3.3 (Note that sub-section p is composed by beads p, $p+1$ and $p+2$).

2. Calculation of the non-zero contributions to the bending forces over all beads composing each sub-section p as follows:

   - Bending force on bead p of sub-section p as:

$$\mathbf{F}^{(\phi)}_{p,p} = -\frac{K_b}{a^2}\left(\boldsymbol{\delta}-\mathbf{u}_p\otimes\mathbf{u}_p\right)\cdot\mathbf{u}'_{p+1} \tag{3.3}$$

   - Bending force on bead $p+2$ of sub-section p as:

$$\mathbf{F}^{(\phi)}_{p+2,p} = \mathbf{Z}^{-1}_{p+1}\cdot\left[\frac{K_b}{a^2}\left(\boldsymbol{\delta}-\mathbf{u}'_{p+1}\otimes\mathbf{u}'_{p+1}\right)\cdot\mathbf{u}_p\right] \tag{3.4}$$

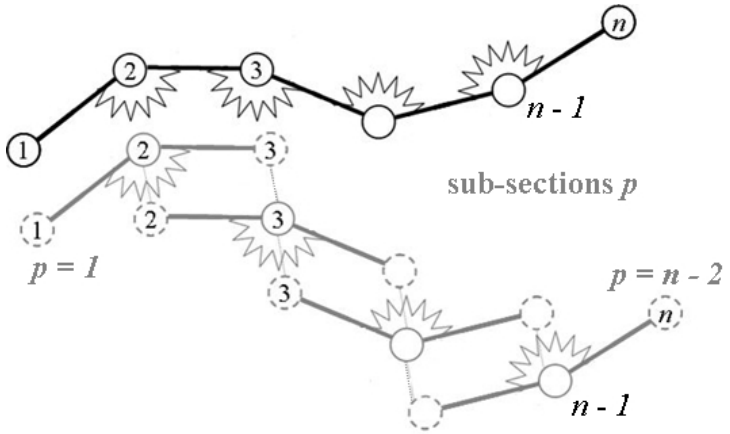

Figure 3.3: Multi bead-rod model of n beads (in black) decomposed in $n-2$ sub-sections p constituted by two consecutive rods (in gray)

Bending force on bead $p+2$ of sub-section p has been rotated back (operator $\mathbf{Z}_{p+1}^{-1}$) in order to correct the direction of the force, that must to be in coherence with the actual bent configuration.

- As the bending potential in each sub-section is locally independent of the adjacent sub-sections, it must to satisfy mechanical equilibrium and, hence, bending force on bead $p+1$ of sub-section p writes:

$$\mathbf{F}_{p+1,p}^{(\phi)} = -\mathbf{F}_{p,p}^{(\phi)} - \mathbf{F}_{p+2,p}^{(\phi)} \tag{3.5}$$

3. Finally, total bending force acting on bead k is calculated as follows:

$$\mathbf{F}_{k}^{(\phi)} = \sum_{p=1}^{n-2} \mathbf{F}_{k,p}^{(\phi)} \tag{3.6}$$

Given that hydrodynamic interaction is neglected and an isotropic friction tensor is supposed, BD simulation is implemented with a first-order integration scheme in coherence with the predictor-corrector algorithm. Shear-stress tensor contribution coming from the micro-mechanical model is calculated with the modified Kramers-Kirkwood expression using the "long-lasting" Brownian forces algorithm. A bi-dimensional modelling is used because it was previously validated in the case of a freely-jointed (three-bead)-(two-rod) chain model (see §2.5.4).

As in the BD simulations of general multi-bead-rod chain models, distance between beads a is employed as the characteristic length of the system. Time scale in the BD simulations is made dimensionless using the longest relaxation time (or rotational diffusion time) of an equal length multi-bead rigid-rod given before in Eq. (2.97).

In what follows, an analysis of the BD predictions is presented for the two simulated tests in linear viscoelasticity: small-amplitude osciallatory deformation and relaxation test

after a shear-strain step.

3.3 Small-Amplitude Oscillatory Deformation Test

BD simulation previously described was implemented in the general algorithm given in §2.3.1 for predicting the dynamic response of a non-freely jointed multi-bead-rod system with a natural bent configuration, which is the physical model intended to emulate the mechanical response under flow conditions of a SWNT that contains bendable junctions.

In the first stage, let us to analyze the simplest case, i.e. the (three-bead)-(two-rod) system. BD simulation for the freely-jointed version of this model (i.e. with $K_b = 0$) was presented in §2.5.4. In a general way, two different regions are clearly differentiated in the dynamic response of a freely-jointed (three-bead)-(two-rod) system: a low frequency regime exhibiting a typical Maxwell terminal behaviour, where the thermal activity (or Brownian forces) drives the kinematic of the system; and a high frequency regime, where the domination of flow forces over the diffusivity terms produces a plateau for the storage modulus and a limiting constant viscosity larger than zero.

Considering the existence of the bending potential, i.e. a non-freely jointed (three-bead)-(two-rod) system, a large range of dynamic responses is deployed in function of the equilibrium configuration and the bending rigidity constant. To explain this fact, in Fig. 3.4 the dynamic responses of a freely-jointed system, two non-freely jointed systems with natural straight configuration and a non-freely jointed system with a naturally bent configuration are compared. Rod misalignment (i.e. the natural bent SWNT configuration) is generated following the next formula:

$$\theta_i^0 = \theta_{i-1}^0 - \Delta\theta^{\max} + \mathrm{U}\,(0,1) \cdot 2\Delta\theta^{\max} \tag{3.7}$$

where θ_i^0 is the equilibrium director angle of rod i, $\Delta\theta^{\max}$ is the maximal misalignment between two consecutive rods and $\mathrm{U}\,(0,1)$ is a continuous uniform random distribution function defined between 0 and 1. In a general way, when the bending rigidity constant K_b is equal or greater than the thermal coefficient k_BT, the loss modulus is enhanced over the entire frequency range and the storage modulus is increased in the low frequency regime. Otherwise, if the bending rigidity constant is much lower than the thermal coefficient ($K_b << k_BT$), a dynamic response similar to that one of a freely jointed system is obtained, showing just one dominant relaxation time associated with the thermal-to-flow induced motion transition.

Additionally, in Fig. 3.4 the apparition of new relaxation processes when the bending rigidity constant is considerably greater than the thermal coefficient (i.e. $K_b >> k_BT$) is observed. For instance, the activation of a mild elasticity at intermediate frequencies is clearly noticed in the dynamic response of the non-freely jointed (three-bead)-(two-rod) system with bending rigidity constant $K_b = 10$. When comparing the straight configuration with the bent one, even though the loss modulus responses are similar, an interesting

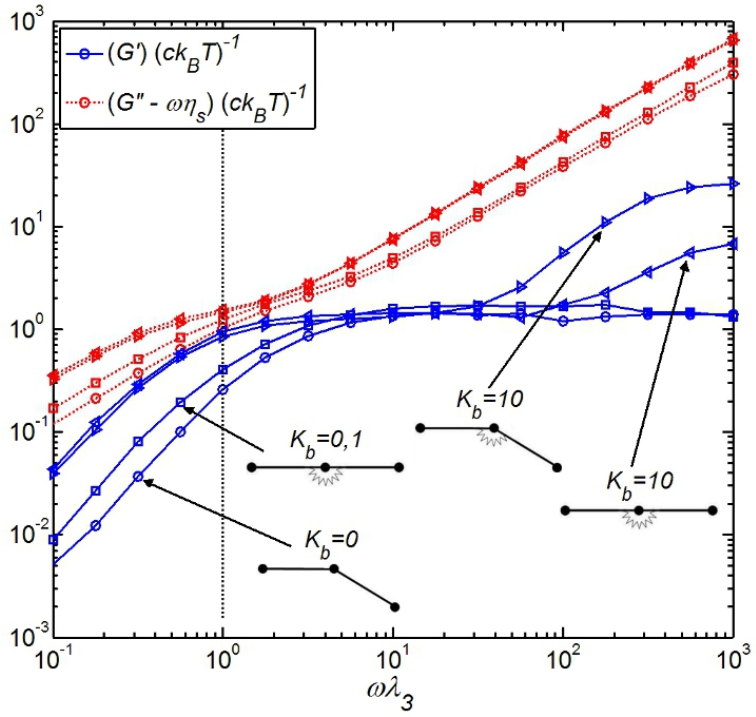

Figure 3.4: BD predicted complex modulus of different (three-bead)-(two-rod) systems: freely jointed, non-freely jointed with natural straight configuration ($K_b = 0.1$ and $K_b = 10$) and non-freely-jointed with natural bent configuration ($K_b = 10$ and $\Delta\theta^{\max} = 30°$). $n = 2$, $c = a = \zeta = 1$, and $k_BT = 0.1$ are the BD parameters. λ_3 is the rotational diffusion time of a (three-bead) rigid-rod system of equal length

difference in the storage modulus is appreciated. In fact, on the one hand the activation of the mild elasticity for the system with a natural bent configuration is observed at a lower characteristic frequency than the system with a straight configuration; on the other hand, a more steeped mild elasticity is noticed for the bent system in comparison with the straight one. In front of this qualitative feature the appropriateness of considering a natural bent configuration for a SWNTs is a priori justified when analyzing its dynamic response under flow.

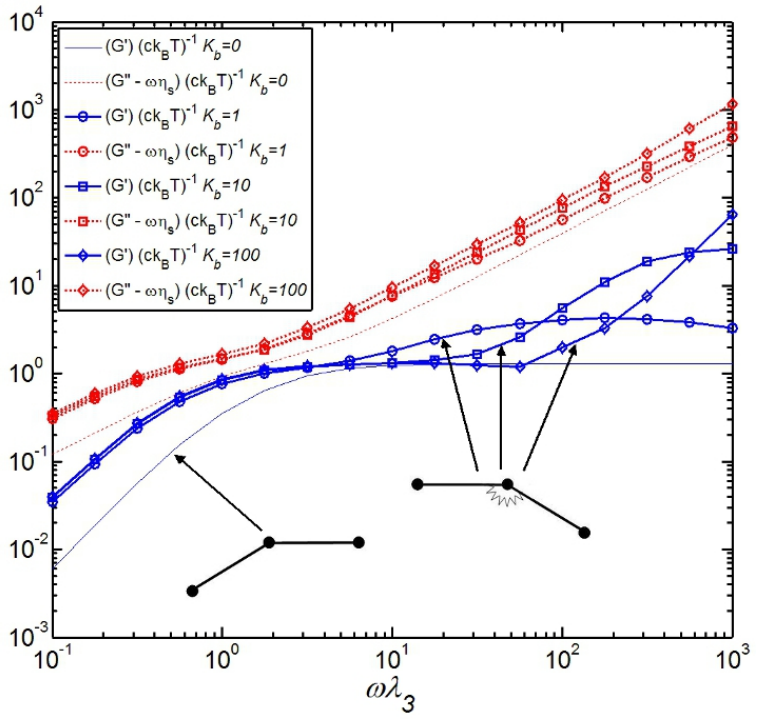

Figure 3.5: BD predicted complex modulus of a non-freely jointed (three-bead)-(two-rod) system with a natural bent configuration (maximal misalignment angle $\Delta\theta^{\max} = 30°$) for different values of the bending rigidity constant K_b. Freely-jointed system ($K_b = 0$) is presented as reference. $n = 2$, $c = a = \zeta = 1$, and $k_BT = 0.1$ are the BD parameters. λ_3 is the rotational diffusion time of a (three-bead) rigid-rod system of equal length

In Fig. 3.5 the BD predictions of the complex modulus for a non-freely jointed (three-bead)-(two-rod) system with a natural bent configuration for different values of the bending rigidity constant are presented. In Fig. 3.5 the typical thermal-to-flow induced relaxation process occurring around the rotational diffusion time λ_3 (as in the equivalent straight systems) is easily identifiable. Additionally, an interesting second relaxation process (as showed before) activating a mild elasticity at intermediate frequencies is again appreciated for the natural bent systems. BD simulations have showed that the characteristic frequency of this relaxation process and the magnitude of the storage modulus enhancement are function of the bending rigidity constant. The activation frequency of this mild elasticity is increased as the bending rigidity constant is increased as well. This feature is physically

coherent taking into account that a higher energy input (i.e. solicitation frequency) is required for activate the first bending mode of a stiffer system. On the other hand, it is also noticed that the storage modulus enhancement and the frequency range associated to those new relaxation processes also rises as the bending rigidity increases. This qualitative feature can be physically explained considering that the stored internal energy associated with a given bending mode is directly proportional to the bending rigidity constant.

Predictions of the storage modulus of non-freely jointed multi-bead-rod systems with a natural bent configuration for different number of rods ($n = 3$, $n = 5$ and $n = 10$) are showed in Fig. 3.6. As in a Kramers chain, in the present modelling the number of rods reflects the flexibility of the bead-rod system, but in addition it captures the density of bent defects in the SWNT structure. In other words, this parameter is directly related to the SWNT persistent length under flow conditions that, at the same time, is suggested to strongly depend on the presence of bent defects in the SWNT structure. For information, an example of the equilibrium internal angles ($\Delta\theta^0_{i,j} = \theta^0_i - \theta^0_j$) between consecutives rods used for the simulations in Figs. 3.6 and 3.7 is presented in Table 3.1. Differences in the dynamic responses are only appreciable in the flow-induced regime, i.e. at frequencies greater than the characteristic relaxation frequency of an equivalent rod system. In other words, different relaxation processes at intermediate frequencies are activated in function of the number of rods, leading invariably to different curves of the storage modulus. An enhancement of the elastic response when increasing the number of rods is observed and different slopes for the storage modulus in function of the frequency are obtained (from 0.5 for $n = 3$ to 1.2 for $n = 10$ at reduced frequencies between 10^1 and 10^2). This mild elasticity can be explained by the coupled contribution of the tension forces required for maintaining the inextensibility condition (as in the Kramers chain) and the forces coming from the torques activated by the bending of the system.

Table 3.1: Internal angles between consecutives rods ($\Delta\theta^0_{i,j} = \theta^0_i - \theta^0_j$) of the multi-bead-rod systems with natural bent configurations presented in Figs. 3.6 and 3.7

	$\Delta\theta^0_{2,1}$	$\Delta\theta^0_{3,2}$	$\Delta\theta^0_{4,3}$	$\Delta\theta^0_{5,4}$	$\Delta\theta^0_{6,5}$	$\Delta\theta^0_{7,6}$	$\Delta\theta^0_{8,7}$	$\Delta\theta^0_{9,8}$	$\Delta\theta^0_{10,9}$
3 rods	18.9	24.3							
5 rods	−22.4	24.8	7.9	−24.1					
10 rods	−13.3	2.8	27.4	27.9	−20.5	28.2	27.4	−0.9	18.0

On the other hand, in Fig. 3.7 the signatures of the reduced loss modulus for the same systems deployed on Fig. 3.6 are presented. In the low frequency regime the typical thermal motion response is observed for the three systems, i.e. a loss modulus evolving proportional with frequency. As in the storage modulus case, differences between the loss modulus responses for the three multi-bead-rod systems ($n = 3$, $n = 5$ and $n = 10$) are only appreciable in the high frequency range. Differences are quite less important than those found for the storage modulus because just light variations in the slopes were encountered (from 0.7 for $n = 3$ to 0.8 for $n = 10$ in the reduced frequency interval between 10^1 and 10^2).

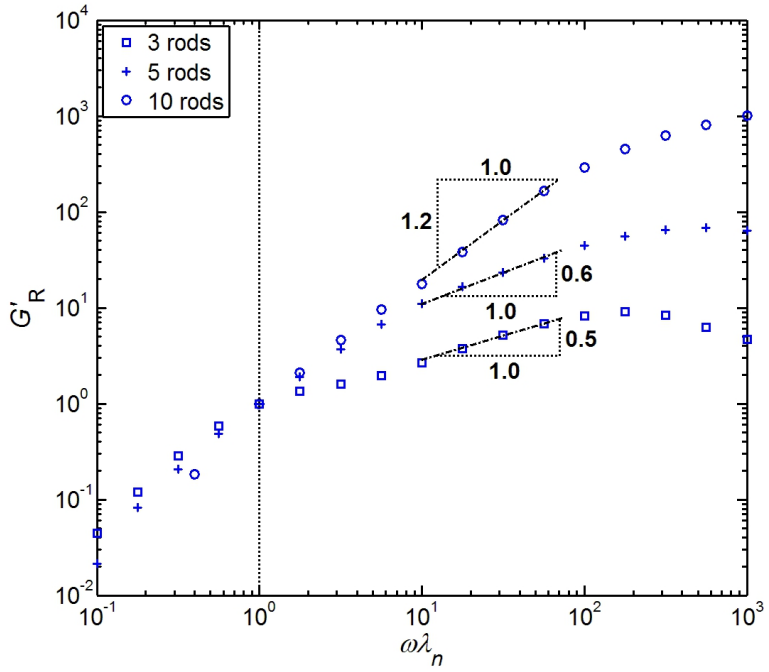

Figure 3.6: Predictions of the storage modulus of a non-freely jointed multi-bead-rod system with a natural bent configuration (maximal misalignment angle $\Delta\theta^{\max} = 30°$) for different number of rods n. $c = a = \zeta = K_b = 1$, and $k_BT = 0.1$ are the BD parameters. Storage modulus is scaled with the value of storage modulus at the unit reduced frequency. λ_n is the rotational diffusion time of a multi-bead rod system of equal length. Vertical pointed line represents the transition between the thermal-induced to the flow-induced regime

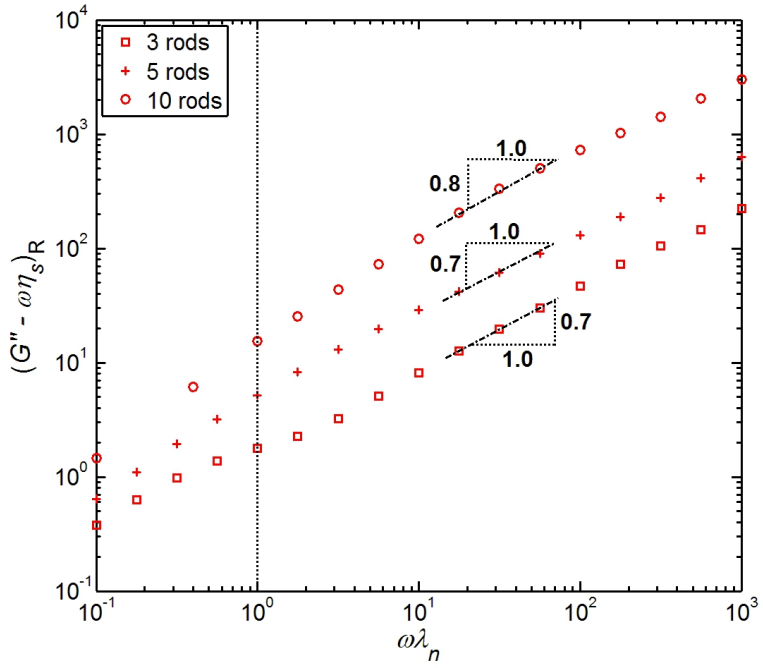

Figure 3.7: Predictions of the loss modulus of a non-freely jointed multi-bead-rod system with a natural bent configuration (maximal misalignment angle $\Delta\theta^{\max} = 30°$) for different number of rods n. $c = a = \zeta = K_b = 1$, and $k_BT = 0.1$ are the BD parameters. Loss modulus is scaled with the value of storage modulus at the unit reduced frequency. λ_n is the rotational diffusion time of a multi-bead rod system of equal length. Vertical pointed line represents the transition between the thermal-induced to the flow-induced regime

In order to properly compare the experimental results on Figs. 1.2 and 1.3 with the BD simulations, experimental data were rescaled using a dimensionless scale. To do so, an estimation of the equivalent rotational diffusion time for the actual surface-treated SWNT is needed. In the expression of the rotational diffusion time for a multi-bead rigid-rod (Eq. 2.97), the isotropic bead friction coefficient ζ is a simple discretization of the bulk friction coefficient $\zeta_{bulk} = n\zeta$. The bulk friction coefficient for a rigid rod system of length L and diameter d can be calculated following the next equation [171]:

$$\zeta_{bulk} = \frac{2\pi\eta_s L}{\log\left[L/d\right]} \tag{3.8}$$

Rheological tests presented in Figs. 1.2 and 1.3 were effectuated at 25° C using a suspension of HiPCO SWNTs (Nanocomposites, Houston, TX, USA) within an epoxy resin with a Newtonian viscosity of 10 Pa s. Length of HiPCO SWNTs largely depends on factors such as whether the tubes have been functionalized and how long they have been sonicated for. HiPCO SWNTs average lengths reported in the literature range from 400 nm to 700 nm and their diameters vary between 0.8 nm and 1.3 nm [120, 171, 17]. Using mean values for the physical dimensions of HiPCO SWNTs and employing Eqs. (2.97) and (3.8), equivalent rotational diffusion times for a SWNT were found ranging from 5.5 s for $n = 10$ to 9.0 s for $n = 3$.

In Fig. 3.8 the scaled experimental data of a 0.2 wt.% SWNT suspension are compared with the dynamical response of a naturally bent non-freely jointed multi-bead-rod system of 5 rods. It appears from Fig. 3.8 that the mild elasticity measured experimentally is a phenomenon occurring in the intermediate frequency range and that the BD simulation produces coherent magnitudes. Observe, for example, that the predicted ratio between G' and G" at intermediate frequencies is similar to that one encountered in experimental dynamical tests of SWNT diluted suspensions. A more precise model-fitting will require identifying experimentally the relaxation time spectra of an individual SWNT and the dynamical response of the diluted suspension in a higher frequency range. Emphasis at this point is made on the fact that a bent SWNT structure (due to presence of synthesis defects) can play an important role in the dynamical response of a SWNT dilute suspension and constitutes, in consequence, a physical parameter to take into account when modelling the mechanical behaviour of SWNTs.

3.4 Relaxation Test after a Shear-Strain Step

3.4.1 Validation of the BD Algorithm

With the aim of validate the algorithm proposed to simulate a relaxation test after a shear-strain step (see §2.3.2), a multi-bead-spring chain model was employed. Given the fact that an exact integral constitutive equation is known for the dilute solution of multi-bead-spring chains, the response for the studied solicitation can be derived analytically and compared directly with the BD simulation results. Let us to tackle the simplest case, i.e.

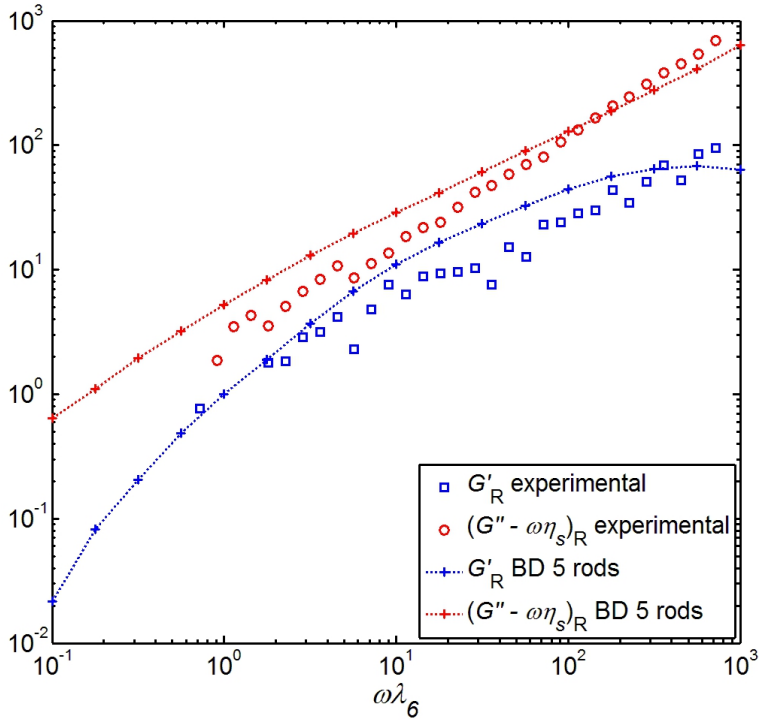

Figure 3.8: Comparison in a proper reduced scale of the experimental dynamic response of a 0.2 wt.% SWNT suspension (from Figs. 1.2 and 1.3) with the BD predicted complex modulus of a naturally bent non-freely jointed multi-bead-rod system of 5 rods (Figs. 3.6 and 3.7)

the Hookean-dumbbell model; integral constitutive equation for this model can be found elsewhere [141]:

$$\boldsymbol{\tau} - \eta_s \dot{\boldsymbol{\gamma}} = -\int_{-\infty}^{t} \left\{ \frac{c k_B T}{\lambda_H} e^{-(t-t')/\lambda_H} \right\} \boldsymbol{\gamma}_{[0]}\left(t, t'\right) dt' \tag{3.9}$$

where $\boldsymbol{\gamma}_{[0]}$ is a finite strain tensor defined in [141] and λ_H is the characteristic time of the Hookean-dumbbell. Signs in Eq. (3.9) are in coherence with the convention where τ_{ii} is negative in compression. In that context, when a quiescent dilute solution of Hookean-dumbbells is submitted to a constant shear-rate $\dot{\gamma}_0$ from $t = 0$ during a given charging time t_c, the contribution of the dumbbells to the shear stress has the next form:

$$\left[\boldsymbol{\tau} - \eta_s \dot{\boldsymbol{\gamma}}\right]_{xz}(t) = \frac{c k_B T}{\lambda_H} \dot{\gamma}_0 \left(t \lambda_H e^{-t/\lambda_H} + \lambda_H^2 - \lambda_H e^{-t/\lambda_H} \left(\lambda_H + t\right) \right) \tag{3.10}$$

Once the shearing step is over, the contribution of the Hookean-dumbbells to the shear stress is progressively diminished until complete relaxation following the next equation:

$$\left[\boldsymbol{\tau} - \eta_s \dot{\boldsymbol{\gamma}}\right]_{xz}(t) = \frac{c k_B T}{\lambda_H} \dot{\gamma}_0 \left(t_c \lambda_H e^{-t/\lambda_H} - \lambda_H e^{-t/\lambda_H} \left(-\lambda_H e^{-t_c/\lambda_H} + \lambda_H + t_c \right) \right) \tag{3.11}$$

Hence, comparison of the analytical solution given by Eqs. (3.10) and (3.11) with the results of an equivalent BD simulation makes possible to determine the validity of the algorithm given in §2.3.2. In this context, a three-dimensional simulation employing an explicit integration scheme was implemented to predict the shear-stress contribution of Hookean-dumbbells during a relaxation test after a shear-strain step. Shear-stress tensor was calculated using the classical Kramers expression (Eq. 2.41). A BD population of 5000 dumbbells was used in the simulation because this size of degrees of freedom was shown to exhibit a good compromise between statistical dispersion and computational cost (see §2.4.4). A time step $\Delta t = \lambda_H/100$ was employed during the relaxation stage given the fact that this length of time step was shown to guarantee convergence of the numerical integration algorithm in absence of external flow fields (see §2.4.4). Figure 3.9 shows the BD prediction of the shear-stress signature of the Hookean-dummbbel ($H = 1$ and $\lambda_H = 0.25$) suspended in a dilute solution that is submitted to a constant shear-rate and after is let to relax. Simulation results are plotted together with the analytical solution for comparison. Simulation presented in Fig. 3.9 was carried out in 6 min (Intel® Core™ T7300 2.00 GHz).

A good agreement between the BD simulation results and the analytical solution given by the Hookean-dumbbell constitutive equation is observed in Fig. 3.9. BD performance is confirmed in both the shearing step and the relaxation step; mean relative errors in linear scale of 1.2% and 2.1% were obtained in the simulation during the shearing step and the relaxation stage, respectively. Previous results confirm, therefore, that the BD algorithm proposed to mimic a relaxation test after a shear-strain step is consistent.

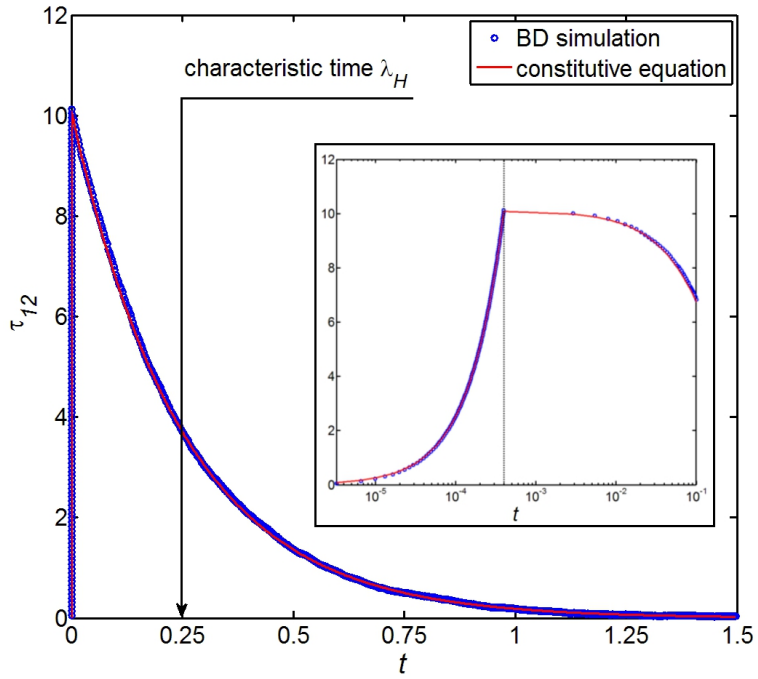

Figure 3.9: BD prediction of the shear-stress signature of a Hookean-dumbbell when its dilute solution is submitted to a constant shear-strain step and after let to relax. Analytical solution is represented by continuous red lines. A population of 5000 dumbbells and a time step $\Delta t = \lambda_H/100$ were employed in the BD simulation. A total shear-strain $\gamma_0 = 10$ was imposed. $H = \zeta = k_B T = c = 1$ are the BD parameters. Insert presents a zoom of the charging step and the early times of the relaxation in logarithmic scale; pointed line marks the end of the shearing step

3.4.2 Relaxation of SWNT Dilute Suspensions

The main purpose of this section is to predict the shear-stress relaxation of a non-freely jointed multi-bead-rod chain with a natural bent configuration and compare the simulation results with the experimental counterpart for treated SWNTs diluted within a Newtonian solvent.

Shear-stress relaxation tests in the linear regime are intended to proportionate detailed information about the whole spectra of relaxation times associated with the suspended particles. In fact, as the suspending matrix is a Newtonian liquid, it is supposed to relax almost instantaneously in a viscous fashion. Therefore, any visco-elastic character observed during the relaxation would be attributable exclusively to the dynamics of the suspended particles. Together with the shear-stress signal, it is also valuable to store the internal energy related to the bending potential. Evolution of the internal bending energy can be used to distinguish the different relaxation processes observed at intermediate frequencies in the BD simulations of small-amplitude oscillatory deformation tests and supposed to be associated with different bending modes. Internal bending energy is calculated using Eq. (3.1).

In order to guarantee a linear behaviour, total shear-strains γ_0 imposed in the current strain step simulations are within the linear regime determined for the simulations of small-amplitude oscillatory deformation tests. On the other hand, with the aim of closely mimic the rapid strain-rates imposed experimentally, the constant shear-rate implemented in the BD simulations is calculated using a shearing time equal to a quarter of the periodic oscillation associated with a reduced frequency of $\omega_R = 10^3$. More specifically, knowing that the reference frequency is given by $\omega\lambda_n = 10^3$ and that the period of the oscillation T related to a given frequency is $\mathrm{T} = 2\pi/\omega$, then shearing time is calculated as follows:

$$t_c = \frac{\pi\lambda_n}{2 \times 10^3} \tag{3.12}$$

where λ_n is the rotational diffusion time of an equivalent multi-bead rigid-rod model containing n beads. BD simulation of the shear-stress relaxation test was implemented in a bi-dimensional framework, which was previously proved to be consistent in the simulations of small-amplitude oscillatory deformation tests (§2.5.4). An explicit integration scheme was employed in the simulations; a time step $\Delta t = \lambda_{bead}/10^5$ was implemented for the sudden shearing step in order to guarantee convergence of the numerical integration algorithm (see Fig. 2.19) and a two-fold longer time step was used during the relaxation in order to guarantee a high time-resolution in the early stages of relaxation. Given the fact that the solicitation regime in a shear-strain step test is analogue with that one found in the strong flow-induced range in a dynamic test (i.e. $\omega_R >> 1$), a BD population of 5000 entities is enough to obtain convergence to the central values. Any reduction of the stochastic noise in the relaxation stage requires the implementation of a more sophisticated random number generator.

Now, let us to study first the relaxation behaviour of the simplest multi-bead-rod

model, i.e. the (three-bead)-(two-rod) system. Figure 3.10 presents the relaxation of the shear-modulus within the linear regime for the *trimer* system and two non-freely jointed (three-bead)-(two-rod) chains with natural straight and natural bent configuration.

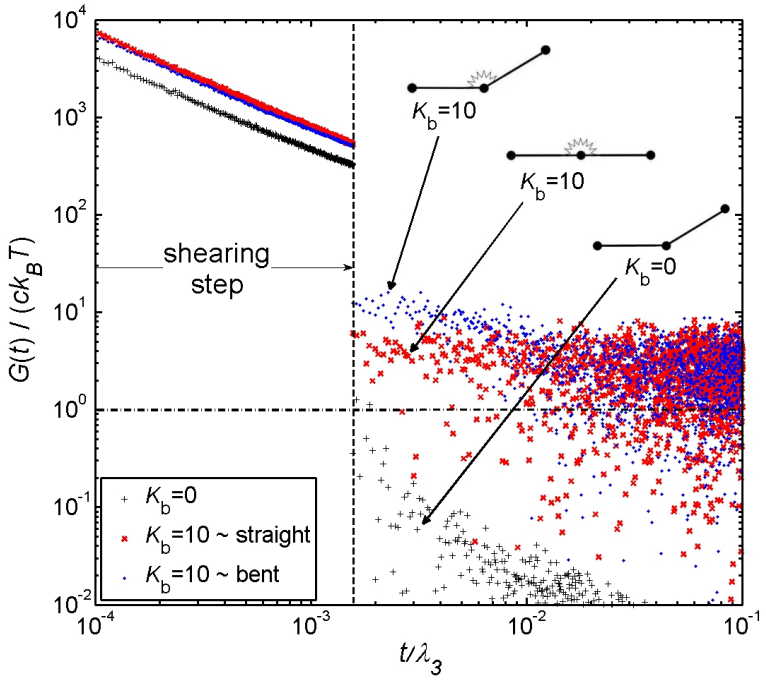

Figure 3.10: BD prediction of the shear-modulus relaxation for different (three-bead)-(two-rod) systems: freely jointed, non-freely jointed with natural straight configuration ($K_b = 10$) and non-freely jointed with natural bent configuration ($K_b = 10$ and $\Delta\theta^{\max} = 30°$). Dashed vertical line marks the end of the shearing step. A total shear-strain $\gamma_0 = 1$ was imposed. $n = 3$, $c = a = \zeta = 1$, $k_BT = 0.1$, and $K_b = 0$ are the parameters of the BD simulation. λ_3 is the rotational diffusion time of a (three-bead) rigid-rod system of equal length

BD simulations showed that independently of the bending rigidity constant (freely or non-freely jointed) and the quiescent configuration (natural straight or non-straight), the relaxation of the shear-modulus is practically instantaneous, like a perfect viscous liquid. A drop of the shear-modulus in almost three orders of magnitude is observed for the *trimer* system. On the other hand, non-freely jointed systems showed a smaller drop of approximately two orders of magnitude. At first sight, these results seem incoherent with the presumed existence of a relaxation spectrum for the shear-stress in bead-rod chains, especially when the bead-spring counterparts exhibit neat visco-elastic relaxation behaviour under the same conditions. However, testing conditions are precisely the key to understand the obtained BD results. In fact, as already mentioned the shearing step currently imposed is analogue with an oscillatory deformation in the high frequency range, particularly at $\omega_R = 10^3$. From Fig. 3.4 is noticed that at this solicitation frequency the loss modulus is quite larger than the storage modulus (in more than one order of magnitude) for all the systems simulated in Fig. 3.10. In other words, below the current

deformation conditions, the different (three-bead)-(two-rod) models have a preponderant viscous character, which is naturally manifested during the shear-strain step test by an quasi instantaneous shear-stress relaxation. In fact, in a viscous liquid shear-stress is proportional to the shear strain-rate, hence once the shearing is stopped (i.e. shear strain-rate goes instantaneously to zero) the shear-stress presents a dramatic discontinuity as well.

However, despite the extremely rapid relaxation of the shear-modulus, in Fig. 3.10 is noticed that the freely-jointed system behaves differently with respect to the non-freely jointed ones, especially in the relaxation stage. Moreover, in the very early relaxation times, a slight distinction can be made between the naturally straight and the naturally bent non-freely jointed (three-bead)-(two-rod) chains. Those differences in the relaxation spectra of the shear-modulus (blurred due to the stochastic nature of the simulation) can be attributed to the different contributions given by the internal bending-energy to the dynamics of the multi-bead-rod model, as conjectured in the BD simulations of dynamical tests. In fact, this hypothesis is supported also by the curves of stored bending-energy during the simulated shear-strain step tests, which offered more clear information than the shear-stress signal. Figure 3.11 compares the BD predicted stocked bending-energy during a shear-strain step test for the two non-freely jointed (three-bead)-(two-rod) chains simulated in Fig. 3.10: natural straight configuration versus natural bent configuration ($\Delta\theta^{\max} = 30°$).

A neat increment of the stored bending-energy is observed during the shearing step. At the end of the shearing step, the naturally bent system stocked 3.2 times more energy than the naturally straight system; a fact in coherence with the differences of storage modules found in the simulations of dynamic tests (see Fig. 3.4) and that confirms the hypothesis suggested to explain the activation of a mild elasticity in the intermediate frequency range. In Fig. 3.11 a difference in the time scale related to the relaxation of the stored bending-energy is also appreciable. The naturally bent system exhibits a relaxation time that is almost twofold that one of the natural straight model. That difference appears consistent with the larger values of shear-modulus exhibited by the naturally bent system in the early relaxation times. On the other hand, in both cases, relaxation of the stored bending-energy happens in time scales quite more shorter than the characteristic rotational diffusion time λ_3, which also explains why the new relaxation processes observed in the simulations of dynamic tests appear in the high frequency regime.

At this point, BD simulations demonstrate again that a naturally bent SWNT structure can exhibit a different bending dynamics in comparison with that one of a perfectly straight SWNT. This fact corroborates that defects and their structural consequences must be taken into account when explaining the dynamics of an individual SWNT.

In what follows, effect of the bending rigidity constant is tackled comparing the shear-strain step BD simulations of three non-freely jointed (three-bead)-(two-rod) chains with natural bent configurations for different values of bending rigidity constant. As expected, based on the different dynamical responses at $\omega_R = 10^3$ (Fig. 3.5), shear-modulus signature

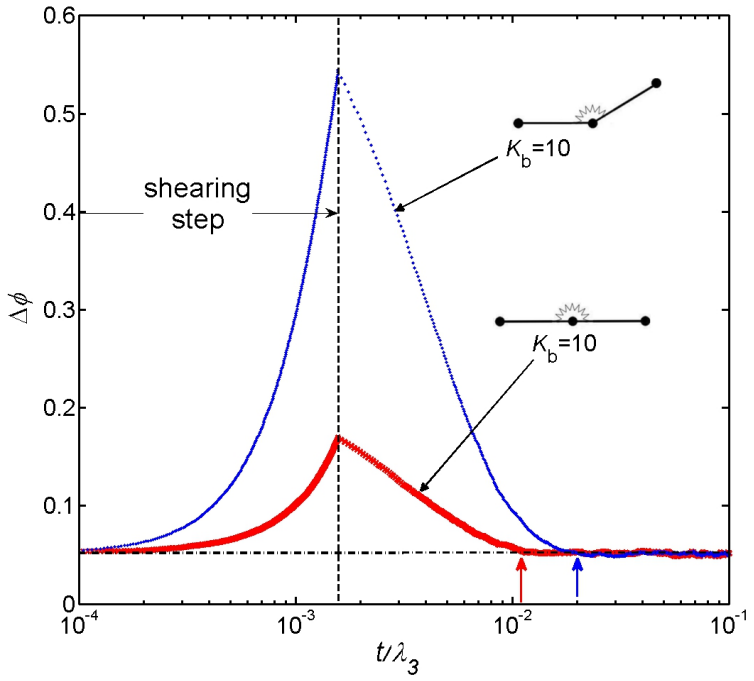

Figure 3.11: BD prediction of the stored bending-energy during a shear-strain step test for two different non freely jointed (three-bead)-(two-rod) systems: naturally straight configuration and naturally bent configuration ($\Delta\theta^{\max} = 30°$). Dashed vertical line marks the end of the shearing step. A total shear-strain $\gamma_0 = 1$ was imposed. $n = 3$, $c = a = \zeta = 1$, $k_BT = 0.1$, and $K_b = 0$ are the parameters of the BD simulation. Stored bending-energy is calculated as follows: $\Delta\phi = \phi - \phi_{\min}$, where $\phi_{\min}$ is the minimal value of the bending potential energy. λ_3 is the rotational diffusion time of a (three-bead) rigid-rod system of equal length

did not vary with respect to the scenario presented in Fig. 3.10; a practically instantaneous relaxation of the shear-stress is exhibited indistinctly of the value of the bending rigidity constant. On the other hand, the BD predicted evolution of the stored bending-energy during the shear-strain step test is presented in Fig. 3.12 and shows more exploitable results.

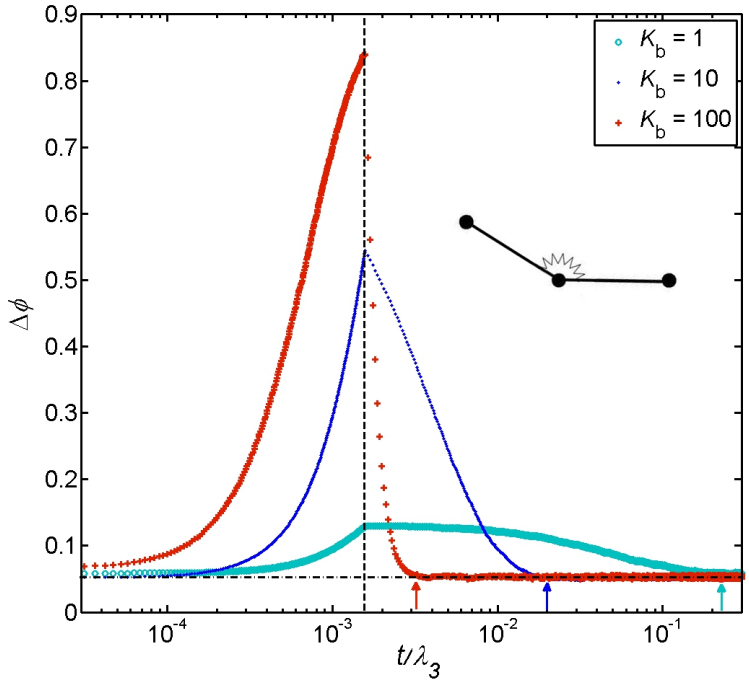

Figure 3.12: BD prediction of the stored bending-energy during a shear-strain step test for three non-freely jointed (three-bead)-(two-rod) chains naturally bent (maximal misalignement angle $\Delta\theta^{\max} = 30°$) with different values of bending rigidity constant. Dashed vertical line marks the end of the shearing step. A total shear-strain $\gamma_0 = 1$ was imposed. $n = 3$, $c = a = \zeta = 1$, $k_BT = 0.1$, and $K_b = 0$ are the parameters of the BD simulation. Stored bending-energy is calculated as follows: $\Delta\phi = \phi - \phi_{\min}$, where $\phi_{\min}$ is the minimal value of the bending potential energy. λ_3 is the rotational diffusion time of a (three-bead) rigid-rod system of equal length

It appears clear that the internal energy stored by the non-freely (three-bead)-(two-rod) model during the shearing step is related directly to the rigidity of the chain. This result is coherent with the increase of the storage modulus in the high frequency range when enhancing the bending rigidity constant K_b. On the other hand, it is found that as higher is the bending rigidity shorter is the relaxation time associated with the stored bending energy. This fact explains why higher solicitation frequencies are required for activating the mild elasticity in the small-amplitude oscillatory deformation tests when the bending rigidity of the multi-bead-rod chain is higher.

Signatures of the internal bending energy evolutions during a shear-strain step test for non-freely jointed multi-bead-rod chains with different number of rods are compared in Fig. 3.13. As already mentioned, the number of rods in the multi-bead-rod model is

related directly to the persistent length under flow conditions (for instance, the shearing step) and, in addition, is a rough approximation to the linear density of bent junctions in the SWNT structure.

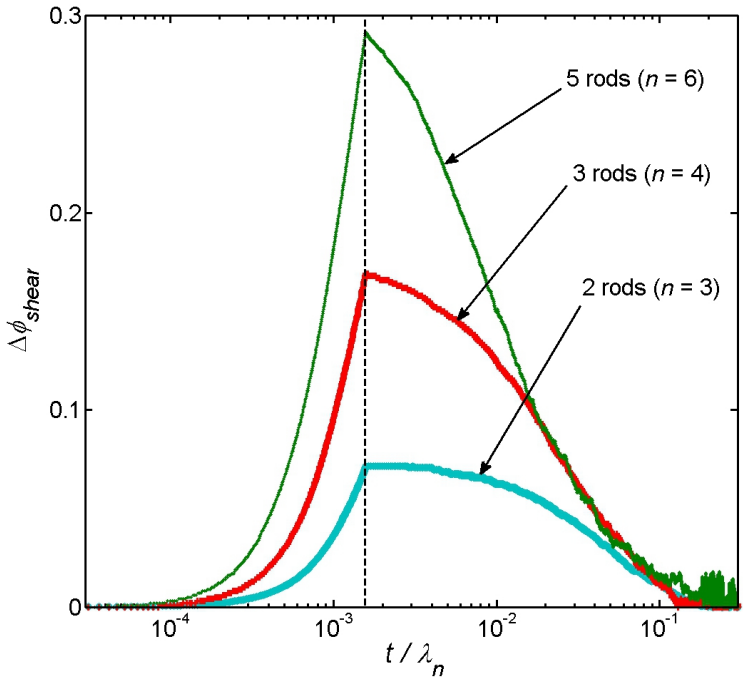

Figure 3.13: BD prediction of the stored bending-energy during a shear-strain step test for three non-freely jointed multi-bead-rod chains naturally bent (maximal misalignement angle $\Delta\theta^{\max} = 30°$) with different number of rods. Dashed vertical line marks the end of the shearing step. A total shear-strain $\gamma_0 = 1$ was imposed. $c = a = \zeta = K_b = 1$, and $k_BT = 0.1$ are the parameters of the BD simulation. Stored shear bending-energy is calculated as follows: $\Delta\phi_{shear} = \phi - \phi_{eq}$, where ϕ_{eq} is the bending-energy at equilibrium. λ_n is the rotational diffusion time of an equivalent multi-bead rigid-rod system of equal length

For a given value of the bending rigidity constant, an increase in the number of constitutive rods is traduced in an enhancement of the stored bending energy during the shearing step; an expectable result given the fact that the bending-energy stocking capacity is related directly to the number of torsion springs in the system. Which results more interesting from Fig. 3.13 are the different energy-relaxation spectra obtained in function of the number of rods; a fact in coherence with the different curves of storage modulus simulated in the high frequency regime for systems with different number of rods. On the other hand, Fig. 3.13 shows that the time scale of the different bending-relaxation modes is directly related to the number of constitutive rods in the model (note that Fig. 3.13 is plotted in a reduced time scale); a fact that could explain, under dynamic solicitation, the increase of the frequency range associated with a mild elastic response when larger number of constitutive rods are considered in the multi-bead-rod chain model.

Finally, once exposed a representative range of BD simulations of the linear shear-stress

relaxation for the non-freely multi-bead-rod model, which is intended to mimic the mechanical behaviour of an individual treated SWNT in dilute solution; a direct comparison with the experimental data of shear-strain step tests on dilute and semi-dilute suspensions of functionalized SWNTs (see Fig. 1.4) can be carried out. A proper comparison requires that time of simulation and experimental data are plotted in a suitable reduced scale. For instance, time in BD simulations is made dimensionless using the rotational diffusion time of a multi-bead rigid-rod model of equal length given by Eq. (2.97). Based on the physical parameters of the suspension used in the shear-strain step tests presented in Fig. 1.4 (HiPCO treated SWNTs dispersed into a Newtonian epoxy resin with an apparent viscosity of 10 Pa s), different equivalent rotational diffusion times in function of the number of centres of hydrodynamic resistance (number of beads n) can be obtained as showed in §3.3. Time in the experimental tests is rescaled then by employing a suitable physically-based rotational diffusion time.

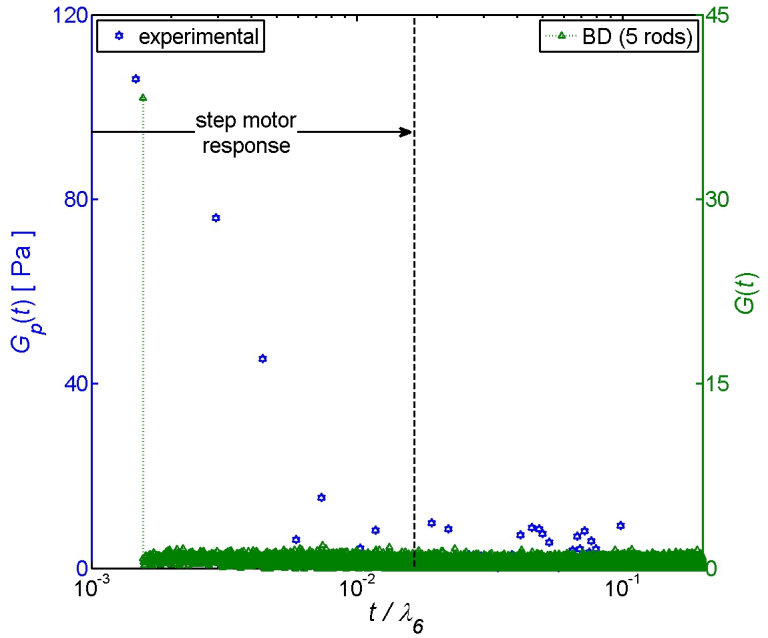

Figure 3.14: Comparison in a proper reduced time scale of the experimental relaxation of the shear-modulus exhibited by the SWNTs in a 0.2 wt.% suspensions within an epoxy resin with the BD predicted relaxation of the shear-modulus of a naturally bent non-freely jointed multi-bead-rod system of 5 rods

With the aim of correctly compare, experimental shear-modulus plotted in Fig. 3.14 corresponds only to the contribution coming from the suspended SWNTs, which is calculated by subtracting the solvent contribution to that one of a 0.2 wt.% SWNT suspension ($G_p = G - G_s$). Surprisingly, the end of the shearing step for the experimental and simulation data practically coincides to the same value in the reduced time scale, a fact that facilitates largely the analysis. Anyway, a direct comparison is only feasible after the step-motor response time (marked by a vertical dashed line in Fig. 3.14), which guarantees

no interference of the rheometer in the mechanical response measured for the suspension. In that context, the window of comparison is restricted to the data placed to the right of the vertical dashed line in Fig. 3.14; in both cases a relaxation of the shear modulus to $\sim 4-5\%$ of the maximal shear-modulus (at the end of the shearing step) is observed. In spite of that evidence, shear-stress signature is not as rich as the bending energy evolution during a shear-strain step test, as demonstrated by the BD results. The experimental relaxation of the shear-modulus that is available for comparison is consistent with the BD simulated response of a non-freely jointed multi-bead-rod model. The proposed physical model for mimicking the structure of a treated SWNT remains consistent, at least, within the regime of linear viscoelasticity.

Conclusion

Brownian dynamics (BD) algorithms for simulating a dynamic test in linear viscoelasticity (small-amplitude oscillatory deformation) and a relaxation test in linear viscoelasticity (after a shear-strain step) have been developed. The BD approach in linear viscoelasticity for the multi-bead-spring models was validated in front of the analytical solutions of the Rouse theory (freely-jointed multi-bead-Hookean-spring chains without hydrodynamic interaction) and Zimm theory (freely-jointed multi-bead-Hookean-spring chains with equilibrium-averaged hydrodynamic interaction), implementing an explicit time-integration scheme and using the Kramers expression for calculating the shear-stress tensor. On the other hand, the BD simulation in linear viscoelasticity for the multi-bead-rod models was validated in front of exact numerical solution for the freely-jointed (three-bead)-(two-rod) chain given by Hassager, implementing an explicit time-integration scheme and using the Kramers-Kirkwood expression coupled with the "long-lasting" Brownian forces algorithm for calculating the shear-stress tensor.

Individual functionalized single-walled carbon nanotubes (SWNTs) are modelled as semi-flexible filaments with an intrinsic bent configuration considering the natural existence of topological defects on the graphitic-like wall structure. Continuous semi-flexible filament model was discretized as a non-freely jointed multi-bead-rod system with a non-straight configuration at equilibrium with the purpose of simulate the linear visco-elastic response of their diluted suspensions within a Newtonian solvent using the validated BD approach. In this micro-mechanical model, intended to mimic the structure of a SWNT, the number of constitutive rods is supposed to be related to the persistent length under flow conditions and, also, to the linear density of topological defects forming bent junctions in the CNT structure. In terms of the numerical implementation of this model inside the BD simulation, a mechanically coherent re-definition of the discretized version of the bending potential, well-known for natural straight systems, was necessary in order to tackle properly the cases of bent configuration. An algorithm by decomposition of the multi-bead-rod chain in (three-bead)-(two-rod) sub-sections was developed with the aim of calculating the forces coming from the internal bending potential.

From both BD simulated tests in linear viscoelasticity, non-negligible differences in the rheological responses were found between the natural straight and the naturally bent models. This fact proved that bent junctions in the structure of a SWNT play an important role in its dynamic behaviour in dilute solution. On the other hand, this result exhorts

considering the effects of topological defects on the modelling of the mechanical properties of CNTs in all the scenarios of solicitation.

New relaxation processes in the dynamic mechanical response of a naturally bent system were observed in the BD simulations of the small-amplitude oscillatory deformation tests. Those processes are characterised by the activation of a mild elasticity at intermediate frequencies (revealed as an enhancement of the storage modulus signature). The level of enhancement of the storage modulus and the range of frequencies associated with those new relaxation processes are found to depend directly on the bending rigidity constant or, in other words, on the local structural stiffness of the SWNT junctions. Moreover, the simulated dynamic response of the non-freely jointed multi-bead-rod model is found function of the persistent length under flow conditions (i.e. number of rods in the discretized version); an augmentation of the storage modulus slope in the intermediate frequency range is observed when increasing the number of constitutive rods. Comparison with the experimental data for dilute suspensions of functionalized SWNTs within an epoxy resin reveals that the magnitudes and tendencies of the BD predicted complex modulus are coherent.

Responses in relaxation mode, given by the BD simulations of the shear-strain step tests, are consistent with the results obtained in dynamic mode. This fact proved the consistence of the non-freely jointed multi-bead-rod chain with naturally bent configuration in the framework of linear viscoelasticity. In all the simulations carried out, an instantaneous relaxation of the shear-stress is verified at the end of the shearing stage. This viscous-like response is coherent with the non-zero limiting viscosity found in the dynamic response at high frequencies. Stored bending-energy signatures during the simulations of shear-strain step tests are found consistent with the new relaxation processes observed in the dynamic response in the intermediate frequency range. Increment of the bending rigidity constant is traduced in an enhancement of the stored bending energy during the shearing step, a result that is in phase with the enhancement of the storage modulus at intermediate frequencies. Additionally, time of relaxation of the stored bending energy after a shear-strain step shortens as the bending rigidity constant increases. Last fact is in coherence with the BD simulations of dynamic tests, in which the solicitation frequency required to activate the mild elasticity increases as the bending rigidity constants increases as well. Finally, experimental shear-stress relaxation tests on dilute and semi-dilute suspensions of treated SWNTs within an epoxy resin exhibit a quasi-instantaneous response; a behaviour correctly predicted by the BD simulations carried out for non-freely jointed multi-bead-rod systems with a natural bent configuration diluted within a Newtonian solvent.

Computational results obtained in this work are useful to give richer explanations to the physical origins of the impressive stiffening effects coming from CNTs on the rheological behaviour of their dilute, semi-dilute and even concentrated suspensions.

The physical model proposed to mimic the mechanical structure of an individual SWNT in solution could be applied for simulating non linear regimes, but probably it should be necessary considering intra- and inter-tube interactions, which can be introduced via the hydrodynamic interaction hypothesis (as done in *polymer* kinetic theory) coupled with a

suitable BD strategy. The analysis of this extended model constitutes a perspective of this work.

Future modelling efforts should be pointed to include several issues not covered in this work: more realistic expressions for the bending potential, poly-dispersed CNT aspect ratio distributions, non-Newtonian suspending mediums, more realistic structural descriptions of the topological defects in CNTs and aggregation effects for the case of pristine CNTs.

In terms of experimental rheology in phase with the current modelling approach, future work should be driven towards the identification of the physical parameters considered in the model and the obtaining of an extended linear viscoelastic database, particularly in the high frequency regime of dynamic tests.

Bibliography

[1] Pan ZW, Xie SS, Chang BH, Wang CY, Lu L, Liu W, Zou WY, Li WZ, and Qian LX. Very long carbon nanotubes. *Nature*, 394:631–632, 1998.

[2] Ajayan PM. Nanotubes from carbon. *Chem Rev*, 99(7):1787–1799, 1999.

[3] Bahr JL and Tour JM. Highly functionalized carbon nanotubes using in situ generated diazonium compounds. *Chem Mater*, 13(11):3823–3824, 2001.

[4] Kharchenko SB, Douglas JF, Obrzut J, Grulke EA, and Migler KB. Flow-induced properties of nanotube-filled polymer materials. *Nat Mater*, 3:564–568, 2004.

[5] Moniruzzaman M and Winey KI. Polymer nanocomposites containing carbon nanotubes. *Macromolecules*, 39(16):5194–5205, 2006.

[6] Hobbie EK. Shear rheology of carbon nanotube suspensions. *Rheol Acta*, 49(4), 2010.

[7] Chico L, Crespi VH, Benedict LX, Louie SG, and Cohen ML. Pure carbon nanoscale devices: Nanotube heterojunctions. *Phys Rev Lett*, 76(6):971–974, 1996.

[8] McEuen PL. Single-wall carbon nanotubes. *Phys World*, 13(6):31–36, 2000.

[9] Vigolo B, Penicaud A, Coulon C, Sauder C, Pailler R, Journet C, Bernier P, and Poulin P. Macroscopic fibers and ribbons of oriented carbon nanotubes. *Science*, 290(5495):1331–1334, 2000.

[10] Wu Z, Chen Z, Du X, Logan JM, Sippel J, Nikolou M, Kamaras K, Reynolds JR, Tanner DB, Hebard AF, and Rinzler AG. Transparent, conductive carbon nanotube films. *Science*, 305(5688):1273–1276, 2004.

[11] Shim M, Kam NWS, Chen RJ, Li Y, and Dai H. Functionalization of carbon nanotubes for biocompatibility and biomolecular recognition. *Nano Lett*, 2(4):285–288, 2002.

[12] Kam NWS, Jessop TC, Wender PA, and Dai H. Nanotube molecular transporters: Internalization of carbon nanotube-protein conjugates into mammalian cells. *J Am Chem Soc*, 126(22):6850–6851, 2004.

[13] Ramesh S, Ericson LM, Davis VA, Saini RK, Kittrell C, Pasquali M, Billups WE, Adams WW, Hauge RH, and Smalley RE. Dissolution of pristine single walled carbon nanotubes in superacids by direct protonation. *J Phys Chem B*, 108(26):8794–8798, 2004.

[14] Davis VA, Ericson LM, Parra-Vasquez ANG, Fan H, Wang Y, Prieto V, Longoria JA, Ramesh S, Saini RK, Kittrell C, Billups WE, Adams WW, Hauge RH, Smalley RE, and Pasquali M. Phase behavior and rheology of swnts in superacids. *Macromolecules*, 37(1):154–160, 2004.

[15] Clinard C, Rouzaud JN, Delpeux S, Beguin F, and Conard J. Electron microscopy, growth and defects of carbon nanotubes. *J Phys Chem Solids*, 55(7):651–657, 1994.

[16] Dimitrakopulos GP, Dravid VP, Karakostas TH, and Pond RC. The defect character of carbon nanotubes and nanoparticles. *Acta Crystallograph A*, 53(3):341–351, 1997.

[17] Fakhri N, Tsyboulski DA, Cognet L, Bruce Weisman R, and Pasquali M. Diameter-dependent bending dynamics of single-walled carbon nanotubes in liquids. *P Natl Acad Sci USA*, 106(34):14219–14223, 2009.

[18] Champetier G, Buvet R, Néel J, and Sigwalt P. *Chimie Macromoléculaire I.* Hermann, 1970.

[19] Castignolles M. *Etudes de la synthèse et de la structure par microscopie électronique des nanotubes de carbone purs et dopés à l'azote.* PhD thesis, Université de Montpellier II, 2004.

[20] Evans EL, Thomas JM, Thrower PA, and Walker PL. Growth of filamentary carbon on metallic surfaces during the pyrolysis of methane and acetone. *Phys Rev B*, 11(5):441–442, 1973.

[21] Iijima S. Helical microtubules of graphitic carbon. *Nature*, 354:56–58, 1991.

[22] Iijima S and Ichihashi T. Single-shell carbon nanotubes of 1-nm diameter. *Nature*, 363:603–605, 1993.

[23] Bethune DS, Klang CH, de Vries MS, Gorman G, Savoy R, Vasquez J, and Beyers R. Cobalt-catalysed growth of carbon nanotubes with single-atomic-layer walls. *Nature*, 363:605–607, 1993.

[24] Ruoff RS, Qian D, and Liu WK. Mechanical properties of carbon nanotubes: theoretical predictions and experimental measurements. *Physique*, 4:903–1008, 2003.

[25] Yuh YH Allinger NL and Lii JH. Molecular mechanics - the mm3 force-field for hydrocarbons. *J Am Chem Soc*, 11(23):8551–8566, 1989.

[26] Tuzun RE, Noid DW, Sumpter RC, and Merkle RC. Dynamics of fluid flow inside carbon nanotubes. *Nanotechnology*, 7(3):241–246, 1996.

[27] Tersoff J. Empirical interatomic potential for carbon, with applications to amorphous carbon. *Phys Rev Lett*, 61(25):2879–2882, 1988.

[28] Brenner DW. Empirical potential for hydrocarbons for use in simulating the chemical vapor-deposition of diamond films. *Phys Rev B*, 42(15):9458–9471, 1990.

[29] Robertson DH, Brenner DW, and Mintmire JW. Energetics of nanoscale graphitic tubules. *Phys Rev B*, 45(21):12592–12595, 1992.

[30] Girifalco LA and Lad RA. Energy of cohesion, compressibility and the potential energy functions of the graphite system. *J Chem Phys*, 25(4):693–697, 1956.

[31] Girifalco LA. Molecular properties of c_{60} in the gas and solid phases. *J Phys Chem*, 96(2):858–861, 1992.

[32] Wang Y, Tomanek D, and Bertsch GF. Stiffness of a solid composed of c_{60} clusters. *Phys Rev B*, 44(12):6562–6565, 1991.

[33] Salvetat JP, Kulik AJ, Bonard JM, Briggs GAD, Stockli T, Metenier K, Bonnamy S, Beguin F, Burnham NA, and Forro L. Elastic modulus of ordered and disordered multiwalled carbon nanotubes. *Adv Mater*, 11(2):161–165, 1999.

[34] Lourie O and Wagner HD. Evaluation of young's modulus of carbon nanotubes by micro-raman spectroscopy. *J Mater Res*, 13(9):2418–2422, 1998.

[35] Yu MF, Files BS, Arepalli S, and Ruoff RS. Tensile loading of ropes of single wall carbon nanotubes and their mechanical properties. *Phys Rev Lett*, 84(24):5552–5555, 2000.

[36] Krishnan A, Dujardin E, Ebbesen TW, and Gibson JM. Young's modulus of single-walled carbon nanotubes. *Phys Rev B*, 58(20):14013–14019, 1998.

[37] Yu MF, Lourie O, Dyer MJ, Moloni K, Kelly TF, and Ruoff RS. Strength and breaking mechanism of multiwalled carbon nanotubes under tensile load. *Science*, 287(5453):637–640, 2000.

[38] Wagner HD, Lourie O, Feldman Y, and Tenne R. Stress-induced fragmentation of multiwall carbon nanotubes in a polymer matrix. *Appl Phys Lett*, 72(2):188–190, 1998.

[39] Li F, Cheng HM, Bai S, Su G, and Dresselhaus MS. Tensile strength of single-walled carbon nanotubes directly measured from their macroscopic ropes. *Appl Phys Lett*, 77(20):3161–3163, 2000.

[40] Pan ZW, Xie SS, Lu L, Chang BH, Sun LF, Zhou WY, Wang G, and Zhang DL. Tensile tests of ropes of very long aligned multiwall carbon nanotubes. *Appl Phys Lett*, 74(21):3152–3154, 1999.

[41] Yakobson BI, Brabec CJ, and Bernholc J. Nanomechanics of carbon tubes: Inestabilities beyond linear response. *Phys Rev Lett*, 76(14):2511–2514, 1996.

[42] Belytschko T, Xiao SP, Schartz GC, and Ruoff RS. Atomistic simulation of nanotube fracture. *Phys Rev B*, 65(235430), 2002.

[43] Wildoer J, Venema L, Rinzler A, Smalley R, and Dekker C. Electronic structure of atomically resolved carbon nanotubes. *Nature*, 391:59–62, 1998.

[44] Wei B, Vajtai R, and Ajayan P. Reliability and current carrying capacity of carbon nanotubes. *Appl Phys Lett*, 79:1172–1174, 2001.

[45] Hong S and Myung S. Nanotube electronics: A flexible approach to mobility. *Nat Nanotechnol*, 2(4):207–208, 2007.

[46] Bonard JM, Kind H, Stockli T, and Nilsson L. Field emission from carbon nanotubes: The first five years. *Solid-State Electronics*, 45:893–914, 2001.

[47] Pop E, Mann D, Wang Q, Goodson K, and Dai H. Thermal conductance of an individual single-wall carbon nanotube above room temperature. *Nano Lett*, 6(1):96–100, 2006.

[48] Saito S. Carbon nanotubes for next-generation electronics devices. *Science*, 278(5335):77–78, 1997.

[49] Fuhrer MS, Nygård J, Shih L, Forero M, Yoon Y, Mazzoni MSC, Choi HJ, Ihm J, Louie SG, Zettl A, and McEuen PL. Crossed nanotube junctions. *Science*, 288(5465):494–497, 2000.

[50] Postma HWC, Teepen T, Yao Z, Grifoni M, and Dekker C. Carbon nanotube single-electron transistors at room temperature. *Science*, 293(5527):76–79, 2001.

[51] Tans SJ, Verschueren ARM, and Dekker C. Room-temperature transistor based on a single carbon nanotube. *Nature*, 393(6680):49–52, 1998.

[52] Derycke V, Martel R, Appenzeller J, and Avouris Ph. Carbon nanotube inter- and intramolecular logic gates. *Nano Lett*, 1(9):453–456, 2001.

[53] Rueckes T, Kim K, Joselevich E, Tseng GY, Cheung C, and Lieber CM. Carbon nanotube-based nonvolatile random access memory for molecular computing. *Science*, 289(5476):94–97, 2000.

[54] Radosavljevic M, Freitag M, Thadani KV, and Johnson AT. Nonvolatile molecular memory elements based on ambipolar nanotube field effect transistors. *Nano Lett*, 2(7):761–764, 2002.

[55] Schmid H and Fink H. Carbon nanotubes are coherent electron sources. *Appl Phys Lett*, 70(20):2679–2680, 1997.

[56] Bonard J, Stöckli T, Noury O, and Châtelain A. Field emission from cylindrical carbon nanotube cathodes: Possibilities for luminescent tubes. *Appl Phys Lett*, 78(18):2775–2777, 2001.

[57] Wang QH, Setlur AA, Lauerhaas JM, Dai JY, Seelig EW, and Chang RPH. A nanotube-based field-emission flat panel display. *Appl Phys Lett*, 72(22):2912–2913, 1998.

[58] Yue GZ, Qiu Q, Gao B, Cheng Y, Zhang J, Shimoda H, Chang S, Lu JP, and Zhou O. Generation of continuous and pulsed diagnostic imaging x-ray radiation using a carbon-nanotube-based field-emission cathode. *Appl Phys Lett*, 81(2):355, 2002.

[59] Dai H, Hafner JH, Rinzler AG, Colbert DT, and Smalley RE. Nanotubes as nanoprobes in scanning probe microscopy. *Nature*, 384(6605):147–150, 1996.

[60] Kong J, Franklin NR, Zhou C, Chapline MG, Peng S, Cho K, and Dai H. Nanotube molecular wires as chemical sensors. *Science*, 287(5453):622–625, 2000.

[61] Wong YM, Kang WP, Davidson JL, Wisitsora-At A, and Soh KL. A novel microelectronic gas sensor utilizing carbon nanotubes for hydrogen gas detection. *Sensors and Actuators B*, 93(1-3):327–332, 2003.

[62] Singh R, Pantarotto D, McCarthy D, Chaloin O, Hoebeke J, Partidos CD, Briand J, Prato M, Bianco A, and Kostarelos K. Binding and condensation of plasmid dna onto functionalized carbon nanotubes: Toward the construction of nanotube-based gene delivery vectors. *J Am Chem Soc*, 127(12):4388–4396, 2005.

[63] Bianco A, Kostarelos K, and Prato M. Applications of carbon nanotubes in drug delivery. *Curr Opin Chem Biol*, 9(6):674–679, 2005.

[64] Zhao Y, Xing G, and Chai Z. Nanotoxicology: Are carbon nanotubes safe? *Nat Nanotechnol*, 3(4):191–192, 2008.

[65] Andrews R, Jacques D, Rao AM, Rantell T, Derbyshire F, Chen Y, Chen J, and Haddon RC. Nanotube composite carbon fibers. *Appl Phys Lett*, 75(9):1329–1331, 1999.

[66] Ericson LM, Fan H, Peng H, Davis VA, Zhou W, Sulpizio J, Wang Y, Booker R, Vavro J, Guthy C, Parra-Vasquez ANG, Kim MJ, Ramesh S, Saini RK, Kittrell

C, Lavin G, Schmidt H, Adams WW, Billups WE, Pasquali M, Hwang W, Hauge RH, Fischer JE, and Smalley RE. Macroscopic, neat, single-walled carbon nanotube fibers. *Science*, 305(5689):1447–1450, 2004.

[67] Jia Z, Wang Z, Xu C, Liang J, Wei B, Wu D, and Zhu S. Study on poly(methyl methacrylate)/carbon nanotube composites. *Mater Sci Eng A*, 271(1-2):395–400, 1999.

[68] Mitchell CA, Bahr JL, Arepalli S, Tour JM, and Krishnamoorti R. Dispersion of functionalized carbon nanotubes in polystyrene. *Macromolecules*, 35:8825–8830, 2002.

[69] Pötschke P, Fornes TD, and Paul DR. Rheological behavior of multiwalled carbon nanotube/polycarbonate composites. *Polymer*, 43:3247–3255, 2002.

[70] Abdel-Goad M and Potschke P. Rheological characterization of melt processed polycarbonate-multiwalled carbon nanotubes composites. *J Non-Newton Fluid*, 128:2–6, 2005.

[71] Satapathy BK, Weidisch R, Pötschke P, and Janke A. Tough-to-brittle transition in multiwalled carbon nanotube (mwnt)/polycarbonate nanocomposites. *Compos Sci Technol*, 67(5):867–879, 2007.

[72] Martin CA, Sandler JKW, Shaffer MSP, Schwarz M, Bauhofer W, Schulte K, and Windle AH. Formation of percolating networks in multi-wall carbon-nanotube-epoxy composites. *Compos Sci Technol*, 64(15 SPEC. ISS.):2309–2316, 2004.

[73] Kim JA, Seong DG, Kang TJ, and Youn JR. Effects of surface modification on rheological and mechanical properties of cnt/epoxy composites. *Carbon*, 44(10):1898–1905, 2006.

[74] Rahatekar SS, Koziol KKK, Butler SA, Elliott JA, Shaffer MSP, Mackley MR, and Windle AH. Optical microstructure and viscosity enhancement for an epoxy resin matrix containing multiwall carbon nanotubes. *J Rheol*, 50(5):599–610, 2006.

[75] Yuen S, Chen-Chi M, Wu H, Kuan H, Chen W, Liao S, Hsu C, and Wu H. Preparation and thermal, electrical, and morphological properties of multiwalled carbon nanotube and epoxy composites. *J Appl Polym Sci*, 103(2):1272–1278, 2007.

[76] Ogasawara T, Ishida Y, Ishikawa T, and Yokota R. Characterization of multi-walled carbon nanotube/phenylethynyl terminated polyimide composites. *Compos Part A-Appl S*, 35(1):67–74, 2004.

[77] Dalmas F, Chazeau L, Gauthier C, Masenelli-Varlot K, Dendievel R, Cavaillé JY, and Forró L. Multiwalled carbon nanotube/polymer nanocomposites: processing and properties. *J Polym Sci Pol Phys*, 43(10):1186–1197, 2005.

[78] Shi X, Hudson JL, Spicer PP, Tour JM, Krishnamoorti, and Mikos AG. Rheological behavior and mechanical characterisation of injectable poly(propylene fumarate)/single-walled carbon nanotube composites for bone tissue engineering. *Nanotechnology*, 16:531–538, 2005.

[79] Song YS. Rheological characterization of carbon nanotubes/poly(ethylene oxide) composites. *Rheol Acta*, 46:231–238, 2006.

[80] Licea-Jiménez L, Henrio P, Lund A, Laurie TM, Pérez-García SA, Nyborg L, Hassander H, Bertilsson H, and Rychwalski RW. Mwnt reinforced melamine-formaldehyde containing alpha-cellulose. *Compos Sci Technol*, 67(5):844–854, 2007.

[81] Liu T, Tong Y, and Zhang W. Preparation and characterization of carbon nanotube/polyetherimide nanocomposite films. *Compos Sci Technol*, 67(3-4):406–412, 2007.

[82] Peeterbroeck S, Laoutid F, Taulemesse J, Monteverde F, Lopez-Cuesta J, Nagy JB, Alexandre M, and Dubois P. Mechanical properties and flame-retardant behavior of ethylene vinyl acetate/high-density polyethylene coated carbon nanotube nanocomposites. *Adv Funct Mater*, 17(15):2787–2791, 2007.

[83] Baughman RH, Zakhidov AA, and de Heer WA. Carbon nanotubes - the route toward applications. *Science*, 297(5582):787–792, 2002.

[84] Schartel B, Pötschke P, Knoll U, and Abdel-Goad M. Fire behaviour of polyamide 6/multiwall carbon nanotube nanocomposites. *Eur Polym J*, 41(5):1061–1070, 2005.

[85] Girifalco LA, Hodak M, and Lee RS. Carbon nanotubes, buckyballs, ropes, and a universal graphitic potential. *Phys Rev B*, 62(19):13104–13110, 2000.

[86] Kim B, Park H, and Sigmund WM. Rheological behavior of multiwall carbon nanotubes with polyelectrolyte dispersants. *Colloid Surface A*, 256(2-3):123–127, 2005.

[87] Islam MF, Rojas E, Bergey DM, Johnson AT, and Yodh AG. High weight fraction surfactant solubilization of single-wall carbon nanotubes in water. *Nano Lett*, 3(2):269–273, 2003.

[88] Lordi V and Yao N. Molecular mechanics of binding in carbon-nanotubepolymer composites. *J Mater Res*, 15(12):2770–2779, 2000.

[89] Thostenson ET, Ren Z, and Chou T. Advances in the science and technology of carbon nanotubes and their composites: A review. *Compos Sci Technol*, 61(13):1899–1912, 2001.

[90] Singh C, Shaffer M, Kinloch I, and Windle A. Production of aligned carbon nanotubes by the cvd injection method. *Physica B*, 323(1-4):339–340, 2002.

[91] Singh C, Shaffer MSP, and Windle AH. Production of controlled architectures of aligned carbon nanotubes by an injection chemical vapour deposition method. *Carbon*, 41(2):359–368, 2003.

[92] Huang ZP, Xu JW, Ren ZF, Wang JH, Siegal MP, and Provencio PN. Growth of highly oriented carbon nanotubes by plasma-enhanced hot filament chemical vapor deposition. *Appl Phys Lett*, 73(26):3845–3847, 1998.

[93] Panagiotou T, Bernard JM, and Mesite SV. Deagglomeration and dispersion of carbon nanotubes using microfluidizer® high shear fluid processors. volume 1, pages 39–42, 2008.

[94] Lu KL, Lago RM, Chen YK, Green MLH, Harris PJF, and Tsang SC. Mechanical damage of carbon nanotubes by ultrasound. *Carbon*, 34(6):814–816, 1996.

[95] Badaire S, Poulin P, Maugey M, and Zakri C. In situ measurements of nanotube dimensions in suspensions by depolarized dynamic light scattering. *Langmuir*, 20(24):10367–10370, 2004.

[96] Shaffer MSP and Windle AH. Analogies between polymer solutions and carbon nanotube dispersions. *Macromolecules*, 32(20):6864–6866, 1999.

[97] Hong C, Lee J, Kalappa P, and Advani SG. Effects of oxidative conditions on properties of multi-walled carbon nanotubes in polymer nanocomposites. *Compos Sci Technol*, 67(6):1027–1034, 2007.

[98] Schaefer DW, Zhao J, Brown JM, Anderson DP, and Tomlin DW. Morphology of dispersed carbon single-walled nanotubes. *Chem Phys Lett*, 375(3-4):369–375, 2003.

[99] Zhou W, Islam MF, Wang H, Ho DL, Yodh AG, Winey KI, and Fischer JE. Small angle neutron scattering from single-wall carbon nanotube suspensions: Evidence for isolated rigid rods and rod networks. *Chem Phys Lett*, 384(1-3):185–189, 2004.

[100] Du F, Fischer JE, and Winey KI. Effect of nanotube alignment on percolation conductivity in carbon nanotube/polymer composites. *Phys Rev B*, 72(12):1–4, 2005.

[101] Doi M and Edwards SF. *The Theory of Polymer Dynamics*. clarendon Press, Oxford, 1987.

[102] Petrie CJS. The rheology of fibre suspensions. *J Non-Newton Fluid Mech*, 87(2-3):369–402, 1999.

[103] Landi BJ, Ruf HJ, Worman JJ, and Raffaelle RP. Effects of alkyl amide solvents on the dispersion of single-wall carbon nanotubes. *J Phys Chem B*, 108(44):17089–17095, 2004.

[104] Huang YY, Ahir SV, and Terentjev EM. Dispersion rheology of carbon nanotubes in a polymer matrix. *Phys Rev B*, 73(125422):1–9, 2006.

[105] Shaffer MSP, Fan X, and Windle AH. Dispersion and packing of carbon nanotubes. *Carbon*, 36:1603–1612, 1998.

[106] Georgakilas V, Kordatos K, Prato M, Guldi DM, Holzinger M, and Hirsch A. Organic functionalization of carbon nanotubes. *J Am Che Soc*, 124(5):760–761, 2002.

[107] Sun Y, Fu K, Lin Y, and Huang W. Functionalized carbon nanotubes: Properties and applications. *Acc Chem Res*, 35(12):1096–1104, 2002.

[108] Dyke CA and Tour JM. Unbundled and highly functionalized carbon nanotubes from aqueous reactions. *Nano Lett*, 3(9):1215–1218, 2003.

[109] Dyke CA and Tour JM. Overcoming the insolubility of carbon nanotubes through high degrees of sidewall functionalization. *Chem - Eur J*, 10(4):812–817, 2004.

[110] Liang F, Beach JM, Rai PK, Guo W, Hauge RH, Pasquali M, Smalley RE, and Billups WE. Highly exfoliated water-soluble single-walled carbon nanotubes. *Chem Mater*, 18(6):1520–1524, 2006.

[111] Du F, Scogna RC, Zhou W, Brand S, Fischer JE, and Winey KI. Nanotube networks in polymer nanocomposites: Rheology and electrical conductivity. *Macromolecules*, 37(24):9048–9055, 2004.

[112] Hough LA, Islam MF, Janmey PA, and Yodh AG. Viscoelasticity of single wall carbon nanotube suspensions. *Phys Rev Lett*, 93(16):168102–1–168102–4, 2004.

[113] Song YS and Youn JR. Influence of dispersion states of carbon nanotubes on physical properties of epoxy nanocomposites. *Carbon*, 43:1378–1385, 2005.

[114] Grady BP. The use of solution viscosity to characterize single-walled carbon nanotube dispersions. *Macromol Chem Physic*, 207(23):2167–2169, 2006.

[115] Fan Z and Advani SG. Rheology of carbon nanotube suspensions. *J Rheol*, 51(4), 2007.

[116] Obrzut J, Douglas JF, Kharchenko SB, and Migler KB. Shear-induced conductor-insulator transition in melt-mixed polypropylene-carbon nanotube dispersions. *Phys Rev B*, 76(19), 2007.

[117] Lin-Gibson S, Pathak JA, Grulke EA, Wang H, and Hobbie EK. Elastic flow instability in nanotube suspensions. *Phys Rev Lett*, 92(4):483021–483024, 2004.

[118] Ma AWK, Mackley MR, and Rahatekar SS. Experimental observation on the flow-induced assembly of carbon nanotube suspensions to form helical bands. *Rheol Acta*, 46(7):979–987, 2007.

[119] Ma AWK, Chinesta F, Tuladhar T, and Mackley MR. Filament stretching of carbon nanotube suspensions. *Rheol Acta*, 47(4):447–457, 2008.

[120] Parra-Vasquez ANG, Stepanek I, Davis VA, Moore VC, Haroz EH, Shaver J, Hauge RH, Smalley RE, and Pasquali M. Simple length determination of single-walled carbon nanotubes by viscosity measurements in dilute suspensions. *Macromolecules*, 40(11):4043–4047, 2007.

[121] Rai PK, Parra-Vasquez NG, Chattopadhyay J, Pinnick RA, Liang F, Sedana AK, Hauge RH, Billups WE, and Pasquali M. Dispersions of functionalized single-walles carbon nanotubes in strong acids: Solubility and rheology. *J Nanosci Nanotechno*, 7:3378–3385, 2007.

[122] Ma AWK, Chinesta F, and Mackley MR. The rheology and modeling of chemically treated carbon nanotubes suspensions. *J Rheol*, 53(3):547–573, 2009.

[123] Fan Z and Advani SG. Characterization of orientation state of carbon nanotubes in shear flow. *Polymer*, 46(14):5232–5240, 2005.

[124] Marceau S, Dubois P, Fulchiron R, and Cassagnau P. Viscoelasticity of brownian carbon nanotubes in pdms semidilute regime. *Macromolecules*, 42(5):1433–1438, 2009.

[125] Rahatekar SS, Koziol KK, Kline SR, Hobbie EK, Gilman JW, and Windle AH. Length-dependent mechanics of carbon-nanotube networks. *Adv Mater*, 21(8):874–878, 2009.

[126] Ma AWK, Chinesta F, and Mackley MR. The rheology of carbon nanotube (CNT) suspensions: Experiments and modelling. volume 1027, pages 752–754, 2008.

[127] Ma WKA, Chinesta F, Ammar A, and Mackley MR. Rheological modeling of carbon nanotube aggregate suspensions. *J Rheol*, 52(6):1311–1330, 2008.

[128] Fry D, Langhorst B, Wang H, Becker ML, Bauer BJ, Grulke EA, and Hobbie EK. Rheo-optical studies of carbon nanotube suspensions. *J Chem Phys*, 124(5):1–9, 2006.

[129] Hobbie EK and Fry DJ. Nonequilibrium phase diagram of sticky nanotube suspensions. *Phys Rev Lett*, 97(3), 2006.

[130] Song W, Kinloch IA, and Windle AH. Nematic liquid crystallinity of multiwall carbon nanotubes. *Science*, 302(5649):1363, 2003.

[131] Badaire S, Zakri C, Maugey M, Derre A, Barisci JN, Wallace G, and Paulin P. Liquid crystals of dna-stabilized carbon nanotubes. *Adv Mater*, 17(13):1673–1676, 2005.

[132] Asada T, Muramatsu H, Watanabe R, and Onogi S. Rheo-optical studies of racemic poly(?-benzyl glutamate) liquid crystals. *Macromolecules*, 13(4):867–871, 1980.

[133] Pasquali M. Polymer composites: Swell properties and swift processing. *Nat Mater*, 3(8):509–510, 2004.

[134] Ma WKA. *The Microstructure and Rheology of Carbon Nanotube Suspensions*. PhD thesis, University of Cambridge, Cambridge, UK, 2008.

[135] Hinch EJ and Leal LG. The effect of brownian motion on the rheological properties of a suspension of nonspherical particles. *J Fluid Mech*, 52:683–712, 1972.

[136] Sepehr M, Carreau PJ, Grmela M, Ausias G, and Lafleur PG. Comparison of rheological properties of fiber suspensions with model predictions. *J Polym Eng*, 24(6):579–610, 2004.

[137] Rajabian M, Dubois C, and Grmela M. Suspensions of semiflexible fibers in polymeric fluids: Rheology and thermodynamics. *Rheol Acta*, 44(5):521–535, 2005.

[138] Folgar F and Tucker III CL. Orientation behavior of fibers in concentrated suspensions. *J Reinf Plast Comp*, 3(2):98–119, 1984.

[139] Larson RG. *The Structure and Rheology of Complex Fluids*. Oxford University Press, 1999.

[140] Xu J, Chatterjee S, Koelling KW, Wang Y, and Bechtel SE. Shear and extensional rheology of carbon nanofiber suspensions. *Rheol Acta*, 44(6):537–562, 2005.

[141] Bird RB, Curtiss CF, Amstrong RC, and Hassager O. *Dynamics of polymer liquids*, volume 2 Kinetic Theory. Wyley-Interscience, second edition, 1987.

[142] Montesi A, Morse DC, and Pasquali M. Brownian dynamics algorithm for bead-rod semiflexible chain with anisotropic friction. *J Chem Phys*, 122(084903), 2005.

[143] Morse DC. Viscoelasticity of concentrated isotropic solutions of semiflexible polymers. 1. model and stress tensor. *Macromolecules*, 31(20):7030–7043, 1998.

[144] Shankar V, Pasquali M, and Morse DC. Theory of linear viscoelasticity of semiflexible rods in dilute solution. *J Rheol*, 46(5):1111–1154, 2002.

[145] Flory PJ. *Statistical mechanics of chain molecules*. Wiley-Interscience, New York, 1969.

[146] Kirkwood JG. *Macromolecules, J. G. Kirkwood Collected Works*. Gordon and Breach, New York, 1967.

[147] Kröger M. *Models for Polymeric and Anisotropic Liquids*. Springer, Berlin Heidelberg, 2005.

[148] Langevin P. Sur la théorie du mouvement brownien. *Comptes Rendus*, 146:530, 1908.

[149] Ottinger HC. *Stochastic Processes in Polymeric Fluids*. Springer, Berlin Heidelberg, 1996.

[150] Ermak DL and McCammon JA. Brownian dynamics with hydrodynamic interactions. *J Chem Phys*, 69(4):1352–1360, 1978.

[151] Pear MR and Weiner JH. Brownian dynamics study of a polymer chain of linked rigid bodies. ii. results for longer chains. *J Chem Phys*, 72(7):3939–3947, 1980.

[152] Hatzikiriakos SG and Vlassopoulos D. Brownian dynamics simulations of shear-thickening in dilute polymer solutions. *Rheo Acta*, 35(3):274–287, 1996.

[153] Agarwal US, Bhargava R, and Mashelkar RA. Brownian dynamics simulation of a polymer molecule in solution under elongational flow. *J Chem Phys*, 108(4):1610–1617, 1998.

[154] Cass MJ, Heyes DM, and English RJ. Brownian dynamics simulations of associating diblock copolymers. *Langmuir*, 23(12):6576–6587, 2007.

[155] Jin S and Collins LR. Dynamics of dissolved polymer chains in isotropic turbulence. *New J Phys*, 9, 2007.

[156] Venkataramani V, Sureshkumar R, and Khomami B. Coarse-grained modeling of macromolecular solutions using a configuration-based approach. *J Rheol*, 52(5):1143–1177, 2008.

[157] Dwyer JD and Bloomfield VA. Brownian dynamics simulations of probe and self-diffusion in concentrated protein and dna solutions. *Biophys J*, 65(5):1810–1816, 1993.

[158] Merlitz H, Rippe K, Kienin KV, and Langowski J. Looping dynamics of linear dna molecules and the effect of dna curvature: A study by brownian dynamics simulation. *Biophys J*, 74(2I):773–779, 1998.

[159] García de la Torre J, Pérez Sánchez HE, Ortega A, Hernández JG, Fernandes MX, and Díaz FG. Calculation of the solution properties of flexible macromolecules: Methods and applications. *Eur Biophys J*, 32(5):477–486, 2003.

[160] Kenward M and Dorfman KD. Coarse-grained brownian dynamics simulations of the 10-23 dnazyme. *Biophys J*, 97(10):2785–2793, 2009.

[161] Ansell GC and Dickinson E. Brownian dynamics simulation of the fragmentation of a large colloidal floc in simple shear flow. *J Colloid Interf Sci*, 110(1):73–81, 1986.

[162] Xue W and Grest GS. Brownian dynamics simulations for interacting colloids in the presence of a shear flow. *Phys Rev A*, 40(3):1709–1712, 1989.

[163] Heyes DM and Branka AC. Brownian dynamics simulations of self-diffusion and shear viscosity of near-hard-sphere colloids. *Phys Rev E*, 50(3):2377–2380, 1994.

[164] Bijsterbosch BH, Bos MTA, Dickinson E, Van Opheusden JHJ, and Walstra P. Brownian dynamics simulation of particle gel formation: From argon to yoghurt. *Faraday Discuss*, 101:51–64, 1995.

[165] Tokuyama M. Effective diffusion model on brownian dynamics of hard-sphere colloidal suspensions. *Physica A*, 265(3):333–340, 1999.

[166] Miyahara M, Watanabe S, and Higashitani K. Modeling adsorption and order formation by colloidal particles on a solid surface: A brownian dynamics study. *Chem Eng Sci*, 61(7):2142–2149, 2006.

[167] Schmidt M, Patrick Royall C, Van Blaaderen A, and Dzubiella J. Non-equilibrium sedimentation of colloids: Confocal microscopy and brownian dynamics simulations. *J Phys-Condens Mat*, 20(49), 2008.

[168] Mori N, Fujioka H, Semura R, and Nakamura K. Brownian dynamics simulations for suspension of ellipsoids in liquid crystalline phase under simple shear flows. *Rheol Acta*, 42(1):102–109, 2003.

[169] Siettos CI, Graham MD, and Kevrekidis IG. Coarse brownian dynamics for nematic liquid crystals: Bifurcation, projective integration, and control via stochastic simulation. *J Chem Phys*, 118(22):10149–10156, 2003.

[170] Song YS and Youn JR. Modeling of rheological behavior of nanocomposites by brownian dynamics simulation. *Korea-Aust Rheol J*, 16(4):201–212, 2004.

[171] Mendes MJ, Schmidt HK, and Pasquali M. Brownian dynamics simulations of single-wall carbon nanotube separation by type using dielectrophoresis. *J Phys Chem B*, 112(25):7467–7477, 2008.

[172] Nayac R. *Molecular simulation of liquid crystal polymer flow: a wavelet- finite element analysis*. PhD thesis, MIT, Cambridge, MA, USA, 1998.

[173] Lozinski A and Chauviere C. A fast solver for fokker-planck equation applied to viscoelastic flows calculations: 2d fene model. *J Comput Phys*, 189(2):607–625, 2003.

[174] Lozinski A, Chauviere C, Fang J, and Owens RG. Fokker-planck simulations of fast flows of melts and concentrated polymer solutions in complex geometries. *J Rheol*, 47(2):535–561, 2003.

[175] Chauviere C, Fang J, Lozinski A, and Owens RG. On the numerical simulation of flows of polymer solutions using high-order methods based on the fokker-planck equation. *Int J Mod Phys B*, 17(1-2):9–14, 2003.

[176] Chauviere C and Lozinski A. Simulation of dilute polymer solutions using a fokker-planck equation. *Comput Fluids*, 33(5-6):687–696, 2004.

[177] Suen JK, Nayak R, Armstrong RC, and Brown RA. A wavelet-galerkin method for simulating the doi model with orientation-dependent rotational diffusivity. *J Non-Newton Fluid*, 114(2-3):197–228, 2003.

[178] Ammar A, Ryckelynck D, Chinesta F, and Keunings R. On the reduction of kinetic theory models related to finitely extensible dumbbells. *J Non-Newton Fluid*, 134(1-3 SPEC. ISS.):136–147, 2006.

[179] Ammar A, Mokdad B, Chinesta F, and Keunings R. A new family of solvers for some classes of multidimensional partial differential equations encountered in kinetic theory modeling of complex fluids. *J Non-Newton Fluid*, 139(3):153–176, 2006.

[180] Laso M and Öttinger HC. Calculation of viscoelastic flow using molecular models: the connffessit approach. *J Non-Newton Fluid*, 47(C):1–20, 1993.

[181] Feigl K, Laso M, and Öttinger HC. Connffessit approach for solving a two-dimensional viscoelastic fluid problem. *Macromolecules*, 28(9):3261–3274, 1995.

[182] Hua CC and Schieber JD. Application of kinetic theory models in spatiotemporal flows for polymer solutions, liquid crystals and polymer melts using the connffessit approach. *Chem Eng Sci*, 51(9):1473–1485, 1996.

[183] Laso M, Picasso M, and Öttinger HC. 2-D time-dependent viscoelastic flow calculations using CONNFFESSIT. *AICHE J*, 43(4):877–892, 1997.

[184] Hua CC and Schieber JD. Viscoelastic flow through fibrous media using the connffessit approach. *J Rheol*, 42(3):477–491, 1998.

[185] Cormenzana J, Ledda A, Laso M, and Debbaut B. Calculation of free surface flows using connffessit. *J Rheol*, 45(1):237–258, 2001.

[186] Keunings R. *Micro-Macro Methods for the Multiscale Simulation of Viscoelastic Flow using Molecular Models of Kinetic Theory*, pages 67–98. British Society of Rheology, 2004.

[187] Ammar A, Chinesta F, Cueto E, and Phillips T. Review on discretization techniques for complex fluid flow models: Past, present and future. volume 907, pages 1336–1341, 2007.

[188] Rouse PE. A theory of the linear viscoelastic properties of dilute solutions of coiling polymers. *J Chem Phys*, 21(7):1272–1280, 1953.

[189] Warner HR. Kinetic theory and rheology of dilute suspensions of finitly extendible dumbbells. *Ind Eng Chem Fundamen*, 11(3), 1972.

[190] Treloar LRG. *The physics of rubber elasticity.* Oxford University Press, London, 1975.

[191] Marko JF and Siggia ED. Stretching dna. *Macromolecules*, 28(26), 1995.

[192] Higham DJ. An algorithmic introduction to numerical simulation of stochastic differential equations. *SIAM Review*, 43(3):525–546, 2001.

[193] Somasi M, Khomami B, Woo NJ, Hur JS, and Shaqfeh ESG. Brownian dynamics simulations of bead-rod and bead-spring chains: Numerical algorithms and coarse-graining issues. *J Non-Newton Fluid*, 108(1-3):227–255, 2002.

[194] Atkinson J, Goh CJ, and Phan-Thien N. Bead-spring models for an adsorbed polymer molecule in a shear flow. *J Chem Phys*, 80(12):6305–6317, 1983.

[195] Fetsko SW and Cummings PT. Brownian dynamics simulation of bead-spring chain models for dilute polymer solutions in elongational flow. *J Rheol*, 39(2):285–299, 1995.

[196] Fixman M. Implicit algorithm for brownian dynamics of polymers. *Macromolecules*, 19(4):1195–1204, 1986.

[197] Kramers HA. The behavior of macromolecules in inhomogeneous flow. *J Chem Phys*, 14(7):415–424, 1946.

[198] Bird RB, Warner HR, and Evans DC. *Advances in Polymer Science*, volume 8. Springer, Berlin Heidelberg, 1971.

[199] Macosko CW. *Rheology. Principles, measurements and applications.* VCH, 1994.

[200] Vattulainen I, Ala-Nissila T, and Kankaala K. Physical tests for random numbers in simulations. *Phys Rev Lett*, 73(19):2513–2516, 1994.

[201] Kirkwood JG and Riseman J. The intrinsic viscosities and diffusion constants of flexible macromolecules in solution. *J Chem Phys*, 16(6):465–573, 1948.

[202] Zimm B. Dynamics of polymer molecules in dilute solution: viscoelasticity, flow birefringence and dielectric loss. *J Chem Phys*, 24(2):269–278, 1956.

[203] Thurston GB and Peterlin A. Influence of finite number of chain segments, hydrodynamic interaction, and internal viscosity on intrinsic birefringence and viscosity of polymer solutions in an oscillating laminar flow field. *J Chem Phys*, 46(12):4881–4885, 1967.

[204] Osaki K, Schrag JL, and Ferry JD. Infinite-dilution viscoelastic properties of poly(α-methylstyrene). applications of zimm theory with exact eigenvalues. *Macromolecules*, 5(2):144–147, 1972.

[205] Fixman M. Construction of langevin forces in the simulation of ydrodynamic interaction. *Macromolecules*, 19(4):1204–1207, 1986.

[206] Ferry JD. *Viscoelastic properties of polymers*. John Wiley & Sons, New Jersey, second edition, 1970.

[207] Liu TW. Flexible polymer chain dynamics and rheological properties in steady flows. *J Chem Phys*, 90(10):5826–5842, 1989.

[208] Hassager O. Kinetic theory and rheology of bead-rod models for macromolecular solutions. *J Chem Phys*, 60(5):2111–2124, 1974.

[209] Fan XJ and Liu TW. Equilibrium and steady-state flow properties of a suspension of freely rotating chains. *J Non-Newton Fluid*, 19(3):303–321, 1986.

[210] Fixman M. Simulation of polymer dynamics. ii. relaxation rates and dynamic viscosity. *J Chem Phys*, 69(4):1538–1545, 1978.

[211] Gottlieb M and Bird RB. A molecular dynamics calculation to confirm the incorrectness of the random-walk distribution for describing the kramers freely jointed bead-rod chain. *J Chem Phys*, 65(6):2467–2468, 1976.

[212] Pear MR and Weiner JH. Brownian dynamics study of a polymer chain of linked rigid bodies. *J Chem Phys*, 71(1):212–224, 1979.

[213] Fixman M. Simulation of polymer dynamics. i. general theory. *J Chem Phys*, 69(4):1527–1537, 1978.

[214] Helfand E. Flexible vs rigid constraints in statistical mechanics. *J Chem Phys*, 71(12):5000–5007, 1979.

[215] Hinch EJ. Brownian motion with stiff bonds and rigid constraints. *J Fluid Mech*, 271:219–234, 1994.

[216] Grassia PS, Hinch EJ, and Nitsche LC. Computer simulations of brownian motion of complex systems. *J Fluid Mech*, 282:373–403, 1995.

[217] Grassia P and Hinch EJ. Computer simulations of polymer chain relaxation via brownian motion. *J Fluid Mech*, 308:255–288, 1996.

[218] Pasquali M and Morse DC. An efficient algorithm for metric correction forces in simulations of linear polymers with constrained bond lengths. *J Chem Phys*, 116(5):1834–1838, 2002.

[219] Allison SA and McCammon JA. Multistep brownian dynamics: application to short wormlike chains. *Biopolymers*, 23(2):363–375, 1984.

[220] Ermak DL and McCammon JA. Brownian dynamics with hydrodynamic interactions. *J Chem Phys*, 69(4):1352–1360, 1978.

[221] Doyle PS, Shaqfeh ESG, and Gast AP. Dynamic simulation of freely draining flexible polymers in steady linear flows. *J Fluid Mech*, 334:251–291, 1997.

[222] Morse DC. Theory of constrained brownian motion. *Adv Chem Phys*, 128:65–189, 2004.

[223] Fixman M and Kovac J. Dynamics of stiff chains. ii. freely jointed chain. *J Chem Phys*, pages 4950–4955, 1974.

[224] Lijima S, Ichihashi T, and Ando Y. Pentagons, heptagons and negative curvature in graphite microtubule growth. *Nature*, 356(6372):776–778, 1992.

[225] Binh VT, Vincent P, Feschet F, and Bonard J. Local analysis of the morphological properties of single-wall carbon nanotubes by fresnel projection microscopy. *J Appl Phys*, 88(6):3385–3391, 2000.

[226] Ouyang M, Huang J, Cheung CL, and Lieber CM. Atomically resolved single-walled carbon nanotube intramolecular junctions. *Science*, 291(5501):97–100, 2001.

[227] Vijayaraghavan A, Marquardt CW, Dehm S, Hennrich F, and Krupke R. Imaging defects and junctions in single-walled carbon nanotubes by voltage-contrast scanning electron microscopy. *Carbon*, 48(2), 2010.

[228] Xue B, Shao X, and Cai W. Comparison of the properties of bent and straight single-walled carbon nanotube intramolecular junctions. *J Chem Theory Comput*, 5(6):1554–1559, 2009.

[229] Ajayan PM, Ravikumar V, and Charlier J. Surface reconstructions and dimensional changes in single-walled carbon nanotubes. *Phys Rev Lett*, 81(7):1437–1440, 1998.

[230] Han J, Anantram MP, Jaffe RL, Kong J, and Dai H. Observation and modeling of single-wall carbon nanotube bend junctions. *Phys Rev B*, 57(23):14983–14989, 1998.

[231] Wako K, Oda T, Tachibana M, and Kojima K. Bending deformation of single-walled carbon nanotubes caused by 5-7 pair couple defect. *Jpn J Appl Phys 1*, 47(8), 2008.

[232] Lambin PH and Meunier V. Structural properties of junctions between two carbon nanotubes. *Appl Phys A*, 68(3):263–266, 1999.

[233] Duggal R and Pasquali M. Dynamics of individual single-walled carbon nanotubes in water by real-time visualization. *Phys Rev Lett*, 96(24), 2006.

[234] Tsyboulski DA, Bachilo SM, and Weisman RB. Versatile visualization of individual single-walled carbon nanotubes with near-infrared fluorescence microscopy. *Nano Lett*, 5(5):975–979, 2005.

[235] Clauss W. Scanning tunneling microscopy of carbon nanotubes. *Appl Phys A-Mater*, 69(3):275–281, 1999.

[236] Kinloch IA, Roberts SA, and Windle AH. A rheological study of concentrated aqueous nanotube dispersions. *Polymer*, 43(26):7483–7491, 2002.

[237] Loos J, Alexeev A, Grossiord N, Koning CE, and Regev O. Visualization of single-wall carbon nanotube (swnt) networks in conductive polystyrene nanocomposites by charge contrast imaging. *Ultramicroscopy*, 104(2):160–167, 2005.

[238] Lamprecht C, Danzberger J, Lukanov P, Tîlmaciu C, Galibert A, Soula B, Flahaut E, Gruber HJ, Hinterdorfer P, Ebner A, and Kienberger F. Afm imaging of functionalized double-walled carbon nanotubes. *Ultramicroscopy*, 109(8):899–906, 2009.

[239] Huang J and Choi W. Controlled growth and electrical characterization of bent single-walled carbon nanotubes. *Nanotechnology*, 19(50), 2008.

Appendix A

Bending Forces in a Multi-Bead-Rod Chain

Total bending force in a multi-bead-rod system writes:

$$\mathbf{F}_k^{(\phi)} = -\frac{\partial \phi}{\partial \mathbf{r}_k} = \frac{K_b}{a} \sum_{i=2}^{n-1} \frac{\partial \left(\mathbf{u}_i \cdot \mathbf{u}_{i-1} \right)}{\partial \mathbf{r}_k} \tag{A.1}$$

Expanding Eq. (A.1):

$$\mathbf{F}_k^{(\phi)} = \frac{K_b}{a} \left(\begin{array}{l} \frac{\partial (\mathbf{u}_2 \cdot \mathbf{u}_1)}{\partial \mathbf{r}_k} + ... + \frac{\partial (\mathbf{u}_{k-1} \cdot \mathbf{u}_{k-2})}{\partial \mathbf{r}_k} + \frac{\partial (\mathbf{u}_k \cdot \mathbf{u}_{k-1})}{\partial \mathbf{r}_k} + \\ \frac{\partial (\mathbf{u}_{k+1} \cdot \mathbf{u}_k)}{\partial \mathbf{r}_k} + ... + \frac{\partial (\mathbf{u}_{n-1} \cdot \mathbf{u}_{n-2})}{\partial \mathbf{r}_k} \end{array} \right) \tag{A.2}$$

$$\mathbf{F}_k^{(\phi)} = \frac{K_b}{a} \left(\begin{array}{l} \frac{\partial \mathbf{u}_2}{\partial \mathbf{r}_k} \mathbf{u}_1 + \frac{\partial \mathbf{u}_1}{\partial \mathbf{r}_k} \mathbf{u}_2 ... + \frac{\partial \mathbf{u}_{k-1}}{\partial \mathbf{r}_k} \mathbf{u}_{k-2} + \frac{\partial \mathbf{u}_{k-2}}{\partial \mathbf{r}_k} \mathbf{u}_{k-1} + \frac{\partial \mathbf{u}_k}{\partial \mathbf{r}_k} \mathbf{u}_{k-1} + \\ \frac{\partial \mathbf{u}_{k-1}}{\partial \mathbf{r}_k} \mathbf{u}_k + \frac{\partial \mathbf{u}_{k+1}}{\partial \mathbf{r}_k} \mathbf{u}_k + \frac{\partial \mathbf{u}_k}{\partial \mathbf{r}_k} \mathbf{u}_{k+1} + ... + \frac{\partial \mathbf{u}_{n-1}}{\partial \mathbf{r}_k} \mathbf{u}_{n-2} + \frac{\partial \mathbf{u}_{n-2}}{\partial \mathbf{r}_k} \mathbf{u}_{n-1} \end{array} \right) \tag{A.3}$$

Equation (A.3) can be evaluated using the identity:

$$\frac{\partial}{\partial \mathbf{r}_k} \mathbf{u}_i = \frac{1}{a} \left(\delta_{k,i+1} - \delta_{k,i} \right) \left(\boldsymbol{\delta} - \mathbf{u}_i \otimes \mathbf{u}_i \right) \tag{A.4}$$

Observing identity (A.4) is clear that the derivative $\frac{\partial}{\partial \mathbf{r}_k} \mathbf{u}_i$ takes a non-zero value only when i is $k-1$ or k. Hence, considering a bead k in the middle of an infinite chain, Eq. (A.3) becomes:

$$\mathbf{F}_k^{(\phi)} = \frac{K_b}{a} \left(\frac{\partial \mathbf{u}_{k-1}}{\partial \mathbf{r}_k} \mathbf{u}_{k-2} \right) + \frac{K_b}{a} \left(\frac{\partial \mathbf{u}_k}{\partial \mathbf{r}_k} \mathbf{u}_{k-1} + \frac{\partial \mathbf{u}_{k-1}}{\partial \mathbf{r}_k} \mathbf{u}_k \right) + \frac{K_b}{a} \left(\frac{\partial \mathbf{u}_k}{\partial \mathbf{r}_k} \mathbf{u}_{k+1} \right) \tag{A.5}$$

Total bending force on bead k, as given in the previous equation, can be interpreted as the sum of three independent contributions. In order to explain the origin of those contributions consider a multi-bead-rod system containing n beads decomposed into $n-2$ independent sub-sections of two consecutive rods as showed in Fig. 3.3. Taking each

of those sub-sections as an independent system, the expressions for the bending forces associated to each sub-section are given by Eq. A.1. For example, sub-section p (composed by beads p, $p+1$ and $p+2$) has the associated bending forces $\mathbf{F}^{(\phi)}_{p,p}$, $\mathbf{F}^{(\phi)}_{p+1,p}$ and $\mathbf{F}^{(\phi)}_{p+2,p}$, where first sub-index refers to the bead and second sub-index refers to the sub-section. Mathematically, those bending forces write:

$$\mathbf{F}^{(\phi)}_{p,p} = \frac{K_b}{a}\frac{\partial\left(\mathbf{u}_{p+1}\cdot\mathbf{u}_p\right)}{\partial\mathbf{r}_p} = \frac{K_b}{a}\frac{\partial\mathbf{u}_p}{\partial\mathbf{r}_p}\mathbf{u}_{p+1} \tag{A.6}$$

$$\mathbf{F}^{(\phi)}_{p+1,p} = \frac{K_b}{a}\frac{\partial\left(\mathbf{u}_{p+1}\cdot\mathbf{u}_p\right)}{\partial\mathbf{r}_{p+1}} = \frac{K_b}{a}\frac{\partial\mathbf{u}_{p+1}}{\partial\mathbf{r}_{p+1}}\mathbf{u}_p + \frac{K_b}{a}\frac{\partial\mathbf{u}_p}{\partial\mathbf{r}_{p+1}}\mathbf{u}_{p+1} \tag{A.7}$$

$$\mathbf{F}^{(\phi)}_{p+2,p} = \frac{K_b}{a}\frac{\partial\left(\mathbf{u}_{p+1}\cdot\mathbf{u}_p\right)}{\partial\mathbf{r}_{p+2}} = \frac{K_b}{a}\frac{\partial\mathbf{u}_{p+1}}{\partial\mathbf{r}_{p+2}}\mathbf{u}_p \tag{A.8}$$

Applying identity (A.4) to the three previous equations we have:

$$\mathbf{F}^{(\phi)}_{p,p} = -\frac{K_b}{a^2}\left(\boldsymbol{\delta} - \mathbf{u}_p\otimes\mathbf{u}_p\right)\mathbf{u}_{p+1} \tag{A.9}$$

$$\mathbf{F}^{(\phi)}_{p+1,p} = -\frac{K_b}{a^2}\left(\boldsymbol{\delta} - \mathbf{u}_{p+1}\otimes\mathbf{u}_{p+1}\right)\mathbf{u}_p + \frac{K_b}{a^2}\left(\boldsymbol{\delta} - \mathbf{u}_p\otimes\mathbf{u}_p\right)\mathbf{u}_{p+1} \tag{A.10}$$

$$\mathbf{F}^{(\phi)}_{p+2,p} = \frac{K_b}{a^2}\left(\boldsymbol{\delta} - \mathbf{u}_{p+1}\otimes\mathbf{u}_{p+1}\right)\mathbf{u}_p \tag{A.11}$$

From the previous equations it results clear that bending forces are in mechanical equilibrium. For this reason:

$$\mathbf{F}^{(\phi)}_{p+1,p} = -\mathbf{F}^{(\phi)}_{p,p} - \mathbf{F}^{(\phi)}_{p+2,p} \tag{A.12}$$

Now, using the previous results about the decomposition of a multi bead-rod system is easy to explain the origin of different contributions in Eq. (A.5) as follows:

$$\mathbf{F}^{(\phi)}_{k} = \mathbf{F}^{(\phi)}_{k,k-2} + \mathbf{F}^{(\phi)}_{k,k-1} + \mathbf{F}^{(\phi)}_{k,k} \tag{A.13}$$

In other words, total bending force on bead k can be interpreted as the sum of all the independent bending forces coming from sub-sections containing bead k.

Appendix B

Modélisation Rhéologique des Suspensions de NTC

B.1 Introduction

Les nanotechnologies sont au cœur de la recherche dans le monde d'aujourd'hui. L'importance des developpements à cette échelle nanométrique a été donnée en quelques mots par Horst Störmer, Prix Nobel de Physique en 1998 : « l'échelle nanométrique constitue le premier échelon à partir duquel nous pouvons commencer à assembler quelque chose d'utile ». Les nanotubes de carbone (NTC) en sont une illustration, tout comme le graphène découvert plus récemment et récompensé par les prix Nobel de physique en 2010.

La structure basique des NTC est une maille hexagonale qui se répète périodiquement dans l'espace. Cette maille de graphène est la structure périodique des feuillets enroulés sur eux mêmes qui forment les tubes. Leur diamètre varie entre 0.4 nm (pour les NTC mono-paroi) et 5 nm (pour les NTC multi-parois). Leur longueur est normalement de l'ordre du micromètre, mais ils peuvent atteindre quelques fractions de millimètre [1]. Leur caractère électrique (conducteur ou semi-conducteur) est déterminé par l'hélicité du pavé graphitique, associée à la direction du vecteur d'enroulement du feuillet de graphène. Au niveau structurel, on se trouve, pour la première fois dans l'histoire, face à un matériau aux dimensions nanométriques et au caractère quasiment unidimensionnel, car son rapport de forme est élevé.

Les NTC exhibent des performances mécaniques très intéressantes, leurs modules élastiques et leurs résistances à la traction sont comparables avec celles de l'acier. De plus, leurs propriétés de conduction thermique et électrique sont comparables avec celles du cuivre. Leurs propriétés à émission de champ attirent aussi l'attention des chercheurs en physique de champs proches. Les excellentes propriétés des NTC ont poussé à imaginer une large gamme d'applications technologiques : des composites à haute performance mécanique, des composants électromécaniques à taille réduite, des fibres à haute résistance et des écrans flexibles.

Les NTC purs exhibent des forces très importantes du type Van der Waals qui entraî-

nent leur agrégation. En conséquence, la dispersion des NTC en tant que tubes individuels est difficile et représente le principal obstacle au développement de leurs applications industrielles [2]. Pour résoudre ce problème, la modification chimique de la paroi extérieure du NTC est une des approches les plus employés pour augmenter leur dispersion [3].

Une large part d'applications des NTC requiert leur mise en forme en phase liquide. C'est la raison pour laquelle, on fait souvent appel aux suspensions de ces NTC dans une matrice newtonienne ou viscoélastique (polymère fondu). Les propriétés des suspensions de NTC dépendent, d'une part, des facteurs intrinsèques aux NTC (nombre de parois, longueur, diamètre, traitement surfacique, hélicité, pureté) et au milieu de suspension, et, d'une autre part, des interactions physico-chimiques entre les NTC et le milieu de suspension.

La maîtrise, et ultérieurement l'optimisation, des procédés de mise en forme basées sur l'écoulement de ces suspensions nécessitent une compréhension fine de leur rhéologie [4]. D'autre part, la caractérisation des suspensions de NTC, qui est souvent complexe due à la grande variabilité des facteurs déterminant leurs propriétés physiques, est largement basée sur leur comportement rhéologique [5]. Donc, l'approfondissement de l'étude de la rhéologie des suspensions de NTC est plus qu'impératif afin d'aboutir à un développement réel des applications technologiques des NTC. Cependant, récemment il a été signalé que les connaissances actuelles sur la rhéologie des suspensions de NTC ne semblent pas consolidées [6]. Cette thèse cherche à combler certaines lacunes dans la compréhension des phénomènes physiques gouvernant le comportement rhéologique des suspensions de NTC.

L'étendue des données expérimentales sur la rhéologie des suspensions de NTC est très vaste, une gamme de phénomènes très variés a été observée dans tous les régimes de concentration. Cependant, due à la nature très diversifiée des NTC (longueurs, diamètres, hélicités, impuretés, défauts, traitements superficielles) et à la grande variété des paramètres contrôlant leurs interactions avec un solvant donné, les données rhéologiques sont difficilement reproductibles et des résultats contradictoires peuvent se trouver dans la littérature [5]. En conséquence, la recherche des bases physiques expliquant le comportement rhéologique des suspensions de NTC est un défi complexe. Dans ce contexte, la rhéologie numérique apparaît comme un outil puissant pour, premièrement, filtrer la base de données croissante sur le comportement rhéologique des suspensions de NTC, et deuxièmement, valider les hypothèses physiques cherchant à expliquer le comportement dynamique des NTC en suspensions. Ce travail se base sur une approche en Dynamique Brownienne, afin d'établir une base physique pour décrire le comportement dynamique d'un NTC immergé dans un solvant, et pour laquelle les explications ne sont aujourd'hui pas encore très claires.

La modélisation abordée dans cette thèse est consacrée au comportement en viscoélasticité linéaire des suspensions diluées des NTC mono-parois (SWNT)[1] fonctionnalisés dans un solvant newtonien. Ce cadre n'est pas restrictif, au contraire, il a pour but d'aborder

[1] *Single-Walled carbon NanoTube*

directement le comportement mécanique intrinsèque de la structure d'un NTC, qui parallèlement constitue une base naturelle pour comprendre les comportements rhéologiques de suspensions de NTC plus complexes. D'autre part, ce cadre de modélisation n'est pas fortuit, en fait, il est profondément inspiré de la théorie cinétique de polymères, dont les modèles fondamentaux ont été développés initialement pour expliquer le comportement dynamique des polymères linéaires en solution diluée.

L'intérêt particulier pour la rhéologie des suspensions de SWNT n'est pas anodin. Les SWNT sont considérés comme le matériau modèle pour obtenir des composants électromécaniques légers et rigides à partir de nano-filaments [7, 8], de fibres de carbones [9] et de films transparents [10]. En plus, les NTC ont un énorme potentiel biomédical en tant que systèmes de transport et d'inoculation de gènes et médicaments à travers des membranes cellulaires [11, 12].

Ce résumé du document de thèse est organisé en trois parties, en faisant un parallèle avec le document principal en langue anglaise. La première partie présente une introduction du cadre de ce travail de recherche (voir §B.2). Un balayage des facteurs clefs contrôlant les propriétés physiques des suspensions de NTC est fait afin d'établir clairement une base sur laquelle analyser l'état de l'art du comportement rhéologique des suspensions de NTC. L'accent est mis sur la caractérisation expérimentale et les diverses approches de modélisation du comportement rhéologique des suspensions diluées de SWNT fonctionnalisés dans une matrice newtonienne, qui constitue le cadre précis de cette recherche. Une attention particulière est apportée au comportement en viscoélasticité linéaire lors de sollicitations dynamiques oscillatoires et d'essais transitoires de relaxation, étant donné qu'il n'existe, actuellement, pas de consensus pour expliquer l'origine physique des réponses rhéologiques observées. En d'autres termes, la recherche d'une base physique unifiée qui soit capable d'expliquer les réponses rhéologiques obtenues lors d'un cisaillement oscillatoire en petite déformation et pendant la relaxation de contraintes après un échelon de cisaillement constitue la motivation principale de cette thèse.

Une fois la portée de la recherche bien établie, la deuxième partie (voir §B.3) présente une illustration de l'approche de modélisation par Dynamique Brownienne (DB), qui correspond au cadre de modélisation utilisé dans ce travail. Le choix de l'approche par DB est en phase avec les analogies récurrentes faites entre le comportement rhéologique des suspensions de NTC et celui de solutions de polymères représentés sous la forme de barres rigides [13, 14]. Les simulations en DB ont démontré être très utiles pour enrichir les modèles micromécaniques proposés pour décrire la structure des macromolécules dans le cadre de la théorie cinétique. Pour cette raison, l'approche par DB est tout à fait valable pour déterminer le comportement dynamique d'un modèle micromécanique censé simuler la structure d'un SWNT individuel. Cette partie illustre l'étroite relation entre la théorie cinétique, établie pour expliquer la rhéologie de fluides complexes, et l'approche stochastique. L'implémentation des simulations en DB dans le cadre de viscoélasticité linéaire est abordée en utilisant les modèles classiques de bille-barre-ressort rencontrés couramment en rhéologie numérique: les théories de Rouse et de Zimm, les modèles bille-barre en flexion

libre et le modèle de filament semi-flexible. La simulation en DB implémentée est, d'une part, validée grâce aux solutions analytiques ou numériquement exactes pour les modèles fondamentaux en théorie cinétique de polymères.

Finalement, la troisième partie (voir §B.4) constitue le point de convergence des deux premières. Basé sur une analyse méticuleuse de la structure des SWNT et des évidences expérimentales révélant leur comportement dynamique en suspension, un modèle micromécanique censé simuler la réponse rhéologique d'un SWNT en suspension est proposé. Ce modèle est fondé sur deux faits : l'existence de défauts topologiques dans le pavé de graphène des parois d'un NTC, qui sont intrinsèquement associés avec quelques instabilités de structure courbée [15, 16], et la nature flexible des NTC, qui joue un rôle prépondérant dans leur dynamique en solution [17]. Enfin, dans le but d'évaluer la cohérence du modèle physique proposé, l'approche en DB validée dans la deuxième partie est employée afin de simuler la réponse en viscoélasticité linéaire d'un SWNT en suspension diluée lorsqu'il est soumis à des fonctions de sollicitation dynamique et de relaxation. Les comparaisons avec les données expérimentales des suspensions diluées de SWNT fonctionnalisés sont satisfaisantes et très prometteuses.

Les conclusions, les défis rémanents et les perspectives futures de ce travail de recherche sont résumés en conclusion (§B.5).

B.2 Rhéologie des Suspensions de NTC

Entre les paramètres clefs qui jouent un rôle prépondérant dans les propriétés rhéologiques d'une suspension de NTC on trouve : le milieu de suspension, le rapport de forme, la concentration, l'état de dispersion et le traitement chimique des NTCs.

La base de données rhéologiques sur les suspensions de NTC est très vaste, mais un manque de principes physiques unifiés qui l'explique a été souvent relevé. Notons, d'une part, que la caractérisation rhéologique des suspensions de NTC est difficilement reproductible, d'autre part, la rhéologie théorique dans le domaine des suspensions de NTC est en retard par rapport aux mesures et descriptions phénoménologiques de la rhéologie de ces suspensions. Un exemple concret de cette image est le cas de suspensions diluées de SWNT fonctionnalisés dans une matrice Newtonienne.

Les courbes expérimentales de la viscosité apparente en fonction du taux de cisaillement pour des suspensions diluées de SWNT fonctionnalisés à l'intérieur d'une résine époxy exhibent un comportement rhéo-fluidifiant (voir Fig. B.1).

Ce comportement classique rhéo-fluidifiant a été expliqué comme le résultat de deux phénomènes : l'orientation des SWNTs dans la direction de l'écoulement et l'alignement aléatoire dû à l'action des forces Browniennes (interaction thermique avec le solvant). Un modèle d'orientation du type Fokker-Planck a permis de modéliser correctement ce comportement [122].

Cependant, lorsque la suspension de SWNTs fonctionnalisés est soumise à une déformation oscillatoire de petite amplitude, une réponse élastique non négligeable est observée

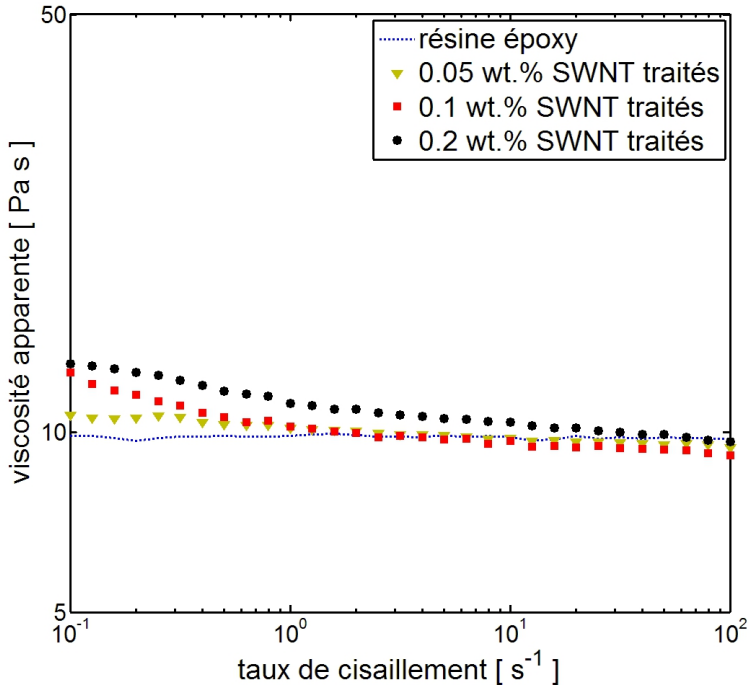

Figure B.1: Viscosité apparente d'une résine époxy et de trois suspensions diluées de SWNT fonctionnalisés dans une résine époxy. Essais isothermes réalisés à 25°. Remerciements au Dr. A. Ma (Rice University) pour la cession des droits de reproduction

à des fréquences intermédiaires (voir Fig. B.2).

Cette réponse rhéologique a pu être modélisée avec le modèle d'orientation Fokker-Planck, mais en utilisant une relation empirique pour le coefficient de diffusion qui dépend de la fréquence appliquée. Il apparaît donc nécessaire d'enrichir le modèle physique. Même si quelques hypothèses existent pour expliquer cette phénoménologie, tels que l'existence d'un faible réseau de SWNT [112], l'interaction électrostatique entre SWNT fonctionnalisés [122] et la nature flexible des SWNT [142] ; l'origine physique de cette contribution élastique est encore en discussion.

Les essais de relaxation obtenus après application d'un échelon de cisaillement ont été réalisés afin de valider l'hypothèse de la présence d'un faible réseau élastique de SWNT à l'intérieur de la suspension ; la mesure d'une contrainte résiduelle en aurait été la preuve. Cependant, les résultats expérimentaux ont montré une relaxation quasi-instantanée, même masquée par le temps de réaction du moteur du rhéomètre (voir Fig. B.3). La courbe du module de relaxation est très proche de la courbe mesurée pour le solvant seul, qui coïncide avec la réponse typique d'un fluide considéré comme parfaitement visqueux.

B.3 Validation de l'Approche en Dynamique Brownienne

Les analogies entre NTC et polymères sont, principalement, établies pour les similarités observées dans leurs comportements rhéologiques en suspension. Par exemple, pour les NTC

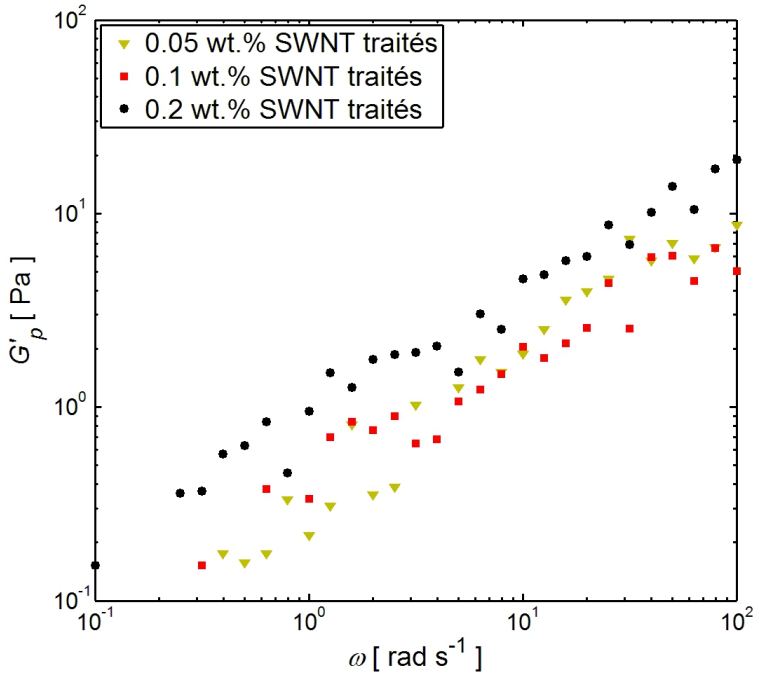

Figure B.2: Contributions des SWNT fonctionnalisés aux modules élastiques de trois différentes suspensions diluées et semi-diluées dans une résine époxy. Essais dynamiques réalisés à 25°. La résine époxy est supposée Newtonienne, donc $G'_s \sim 0$. Remerciements au Dr. A. Ma (Rice University) pour la cession des droits de reproduction

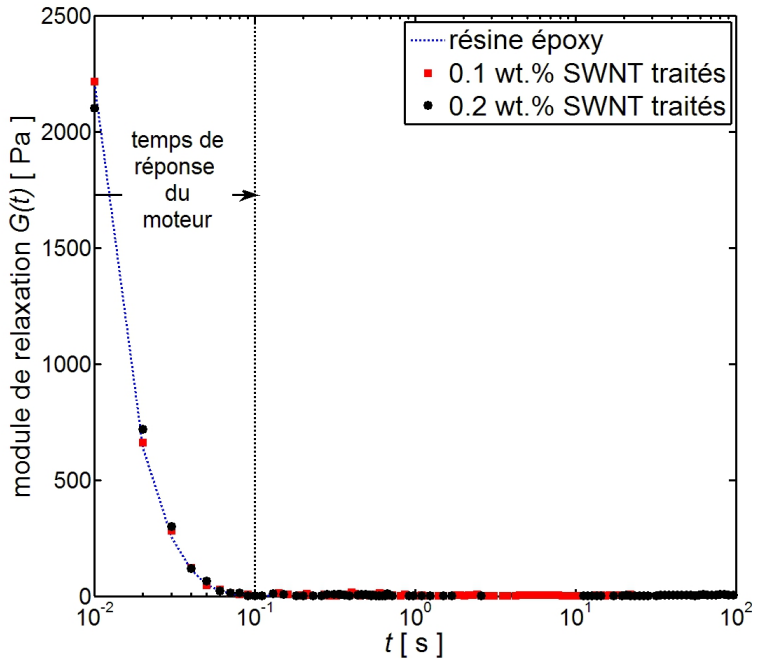

Figure B.3: Relaxation du module de cisaillement pour une résine époxy et deux différentes suspensions diluées de SWNT fonctionnalisés dans une résine époxy. Réponse obtenue après l'application d'un échelon de cisaillement de 1%. Essais réalisés à 25°. Remerciements au Dr. A. Ma (Rice University) pour la cession des droits de reproduction

et les polymères représentés sous la forme de barres rigides, une augmentation abrupte de la viscosité en fonction de la concentration est le reflet d'une transition vers un état fortement enchevêtré [105, 96]. En fait, en termes de modélisation mécanique, un SWNT peut être assimilé, à une échelle mésoscopique, à un ensemble de barres rigides avec une longueur de persistance plus grande [14]. Dans ce contexte, afin de prédire le comportement rhéologique de suspensions de NTC, il apparait cohérent d'utiliser les approches de modélisation largement développées dans le cadre de la science de polymères.

La théorie cinétique des polymères est définie dans un cadre mathématique dans lequel on cherche à déterminer de lois de comportement pour ces fluides complexes, en se basant sur la structure moléculaire du polymère en écoulement. Les modèles physiques en théorie cinétique sont des représentations simplifiés de la structure moléculaire qui prétend mettre en valeur les caractéristiques mécaniques plus importantes lors de l'écoulement. Les modèles basiques en théorie cinétique représentent la structure d'un polymère en utilisant des billes, des ressorts et des barres comme éléments constitutives.

Les équations de comportement de ces modèles micromécaniques ne peuvent être dérivées analytiquement que pour les cas les plus simples comme par exemple le modèle bille-ressort de Rouse et de Zimm. Pour les modèles micromécaniques plus complexes ont fait souvent appel à une approche stochastique afin de connaître leur comportement rhéologique. La DB fait partie de ces approches stochastiques amplement utilisées dans le cadre de la rhéologie computationnelle de fluides complexes.

En DB, les interactions thermiques du système micromécanique avec le solvant sont traités comme une force de type Brownienne, d'où son caractère stochastique. Dans ce travail, on propose d'utiliser une approche en DB pour simuler le comportement en viscoélasticité linéaire de suspensions diluées de SWNT, fonctionnalisés, dans une résine newtonienne. Plus spécifiquement, on souhaite simuler deux essais classiques de la rhéométrie linéaire : le cisaillement oscillatoire en petites déformations et la relaxation après un échelon de cisaillement. La validation des formalismes algorithmiques et mathématiques de ces simulations en DB a été faite en utilisant quelques modèles micromécaniques classiques de la théorie cinétique, dont l'équation constitutive a une solution analytique exacte. Ces modèles sont : la chaine multi-bille-ressort de Hooke en absence d'interaction hydrodynamique (théorie de Rouse), la chaine multi-bille-ressort de Hooke avec interaction hydrodynamique moyennée à l'équilibre (théorie de Zimm) et le système (trois-billes) (deux-barres) en flexion libre, aussi connu comme *trimer*.

La Fig. B.4 présente les modules de conservation prédits en DB pour trois différentes chaines de Rouse et les compare avec la solution analytique (en ligne continue). Les inexactitudes à basses fréquences peuvent être atténuées en implémentant un algorithme plus sophistiqué de génération de nombres aléatoires. En tout cas, l'ensemble de la simulation en DB exhibe une bonne performance. En effet, elle est capable de prédire l'apparition de nouveaux processus de relaxation (traduit par une augmentation du module élastique à des fréquences intermédiaires) en augmentant le nombre de ressorts dans le modèle.

De la même façon, l'approche en DB a été validée dans les cas où les interactions

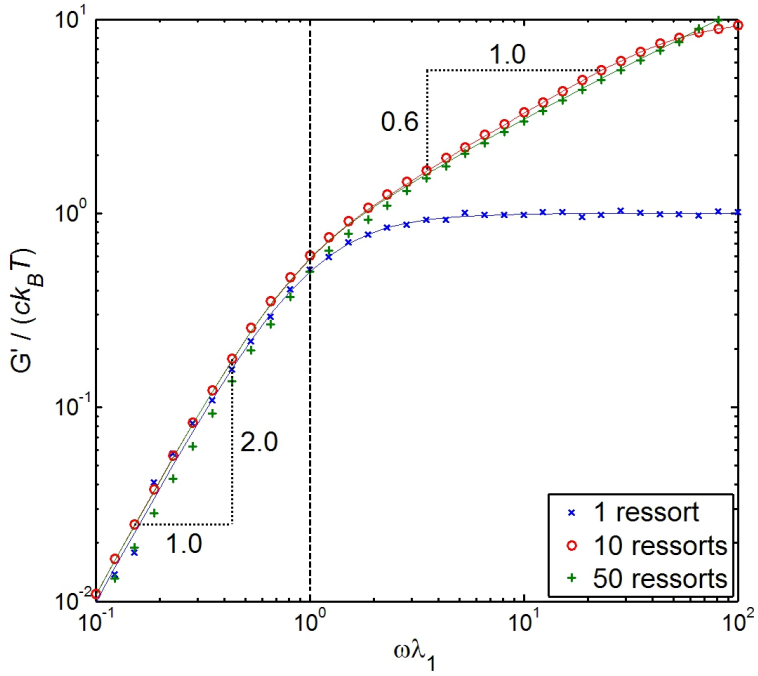

Figure B.4: Module de conservation pour trois chaines de Rouse avec différent nombre de ressorts constitutifs : 1 ressort ou *Hookean dumbbell*, 10 ressorts et 50 ressorts. Comparaison entre la simulation en DB et la solution analytique de la théorie de Rouse

hydrodynamiques (interactions entre billes d'un même ensemble) ne sont pas négligées. Sur la Fig. B.5, une bonne qualité de prédiction est vérifié dans l'intervalle des hautes fréquences pour deux chaines de Zimm à 50 ressorts avec des paramètres d'interaction hydrodynamique limites (très basse interaction, $h^* = 0.003$, et interaction très élevé, $h^* = 0.303$).

Finalement, l'approche en DB pour les modèles contenant des restrictions physiques (c'est-à-dire, des barres infiniment rigides), est aussi validée dans le cadre du comportement dynamique du *trimer*. L'implémentation d'une simulation en DB pour des modèles avec des barres est beaucoup plus délicate que celle des modèles à ressorts car la présence de restrictions physiques oblige à formuler différemment les forces Browniennes dans le système et à considérer des schémas d'intégration temporelle cohérents avec cette nouvelle définition mathématique du potentiel stochastique. Sur la Fig. B.6, nous constatons que l'approche en DB a prédit un module complexe en cohérence avec la solution numériquement exacte donné par Hassager pour le modèle *trimer*. Ce résultat a validé, d'une part, la formulation bidimensionnelle utilisée dans cette thèse pour les modèles à barres et, d'une autre part, le schéma d'intégration temporelle de premier ordre couplé avec un algorithme de forces Browniennes de « longue durée » pour l'estimation du tenseur de contraintes.

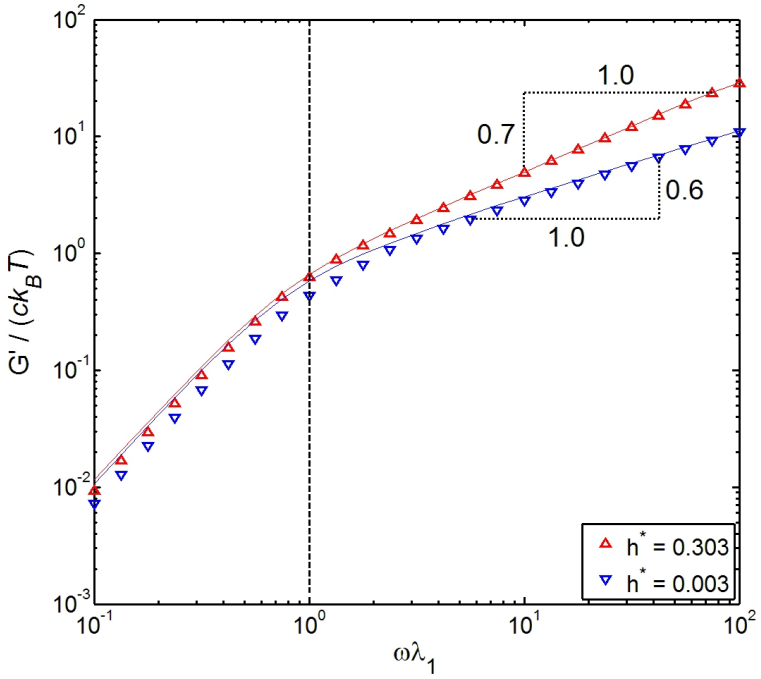

Figure B.5: Module de conservation pour deux chaines de Zimm à 50 ressorts avec différents paramètres d'interaction hydrodynamique : basse interaction $h^* = 0.003$ et interaction très importante, $h^* = 0.303$. Comparaison entre la simulation en DB et la solution analytique de la théorie de Zimm

B.4 Approche en DB aux Suspensions Diluées de SWNT

Une fois la méthode numérique validée, on peut proposer un modèle micromécanique pour représenter la structure d'un SWNT fonctionnalisé, et ainsi simuler la réponse de leurs suspensions diluées en viscoélasticité linéaire. La formulation d'un modèle physique de SWNT a été basée sur deux faits expérimentaux :

1. l'observation directe de la flexion des NTC fonctionnalisés par action thermique à l'intérieur d'une suspension aqueuse [17], et

2. l'observation fréquente des tortuosités sur les images de NTC prises par différents microscopes à champ proche, qui sont explicables par l'existence naturelle des défauts topologiques dans la structure des NTC [24, 15, 231, 228].

De cette manière, nous proposons un modèle de filament semi-flexible avec une configuration d'équilibre non-rectiligne pour représenter les SWNT fonctionnalisés. Pour étudier la réponse de ce modèle physique en DB, le filament semi-flexible a été discrétisé en un système multi-barre composé de n billes à la position $\mathbf{r_i}$, connectées par $n-1$ barres rigides de longueur a. Les billes sont considérées comme les points de résistance hydrodynamique, à l'image de la plupart des modèles mécaniques en théorie cinétique de polymères. Les barres sont supposées infiniment rigides. Un potentiel de flexion inter-barre tient compte de la raideur en flexion des NTC.

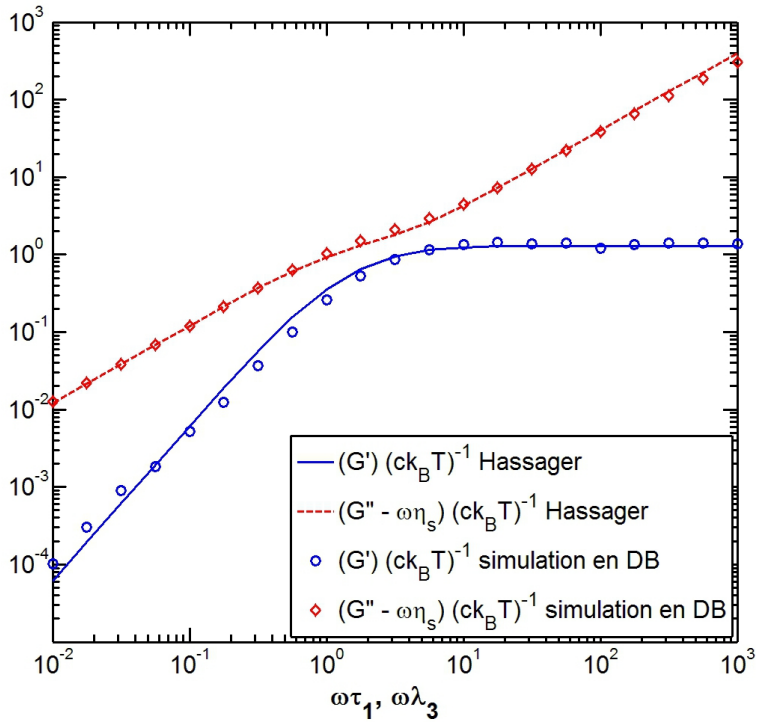

Figure B.6: Module complexe pour un système (trois-bille)-(deux-barre) en flexion libre en fonction d'une fréquence réduite. Comparaison entre la simulation en DB et la solution numériquement exacte donnée par Hassager

Les contraintes cinématiques du système à billes, traduisant l'inextensibilité des $n-1$ barres s'écrivent :

$$(\dot{\mathbf{r}}_i - \dot{\mathbf{r}}_{i+1}) \cdot \mathbf{u}_i = 0 \tag{B.1}$$

où $\dot{\mathbf{r}}_i$ est la vitesse instantanée de la bille i et $\mathbf{u}_i$ est un vecteur colinéaire à la barre qui connecte les billes i et $i+1$:

$$\mathbf{u}_j = (\mathbf{r}_{j+1} - \mathbf{r}_j)/a \tag{B.2}$$

L'évolution cinématique du modèle multi-barre est donnée par la solution des n bilans de forces établis sur chacune des n billes du système :

$$\mathbf{F}_i^{(h)} + \mathbf{F}_i^{(b)} + \mathbf{F}_i^{(\phi)} - \mathbf{n}_{ij}\lambda_j = \mathbf{0} \tag{B.3}$$

où $\mathbf{F}_i^{(h)}$ est la force hydrodynamique dans la bille i, $\mathbf{F}_i^{(b)}$ est la force Brownienne dans la bille i, $\mathbf{F}_i^{(\phi)}$ est la force du potentiel de flexion dans la bille i et λ_j est une force de tension associée à la barre qui connecte les billes j et $j+1$. L'operateur $\mathbf{n}_{ij}$ est défini par :

$$\mathbf{n}_{ij} = \mathbf{u}_j (\delta_{i,j+1} - \delta_{i,j}) \tag{B.4}$$

La force hydrodynamique $\mathbf{F}_i^{(h)}$ est donné par :

$$\mathbf{F}_i^{(h)} = \zeta (\boldsymbol{\kappa} \cdot \mathbf{r}_i - \dot{\mathbf{r}}_i) \tag{B.5}$$

où ζ est le coefficient local de friction et $\boldsymbol{\kappa}$ est le tenseur gradient de vitesses. L'ensemble de forces stochastiques suit une distribution Gaussienne, définie par les moments suivants :

$$\left\langle \mathbf{F}_i^{(b)}(t) \right\rangle = \mathbf{0} \tag{B.6}$$

$$\left\langle \mathbf{F}_i^{(b)}(t) \otimes \mathbf{F}_j^{(b)}(t') \right\rangle = \frac{2\zeta k_B T}{\Delta t}\boldsymbol{\delta} \tag{B.7}$$

La présence de restrictions dans les directions des barres rigides requiert une projection géométrique des forces générées de façon aléatoire (Eqs. B.6 et B.7) et données par [216, 217] :

$$0 = \mathbf{F}_i^{(b)} \cdot \mathbf{n}_{ij} \tag{B.8}$$

Le potentiel de flexion pour une configuration d'équilibre non-rectiligne présente la forme suivante :

$$\phi = -\frac{K_b}{a}\sum_{i=2}^{n-1} \mathbf{Z}_i \mathbf{u}_i \cdot \mathbf{u}_{i-1} = -\frac{K_b}{a}\sum_{i=2}^{n-1} \mathbf{u}_i' \cdot \mathbf{u}_{i-1} \tag{B.9}$$

où K_b est une constante de rigidité, $\mathbf{Z}_i$ est un opérateur linéaire de rotation qui aligne les vecteurs des barres dans la configuration d'équilibre et $\mathbf{u}'_i$ est le vecteur ayant subi la rotation $\mathbf{Z}_i\mathbf{u}_i$. En conséquence, l'expression de la force de flexion devient :

$$\mathbf{F}_k^{(\phi)} = -\frac{\partial \phi}{\partial \mathbf{r}_k} = \frac{K_b}{a}\sum_{i=2}^{n-1}\frac{\partial\left(\mathbf{u}'_i \cdot \mathbf{u}_{i-1}\right)}{\partial \mathbf{r}_k} \tag{B.10}$$

Un schéma d'intégration explicite, validé précédemment pour le modèles bille-barre en flexion libre, est implémenté pour obtenir l'évolution cinématique du modèle multi-barre en flexion non-libre. La contribution des SWNT au tenseur de contraintes est faite en utilisant l'expression de Kramers-Kirkwood couplée avec un schéma semi-implicite de forces Browniennes de « longue durée » :

$$\boldsymbol{\tau}_p\left(t\right) = c\sum_v \left\langle \mathbf{R}_v\left(t+\Delta t\right) \otimes \tilde{\mathbf{F}}_v^{(h)}\left(t+\Delta t\right)\right\rangle \tag{B.11}$$

où c est le nombre de SWNT par volume et $\mathbf{R}_v = \mathbf{r}_v - \mathbf{r}_c$ est la position relative de la bille v par rapport au centre de masse $\mathbf{r}_c$ de la chaine.

Une large gamme de réponses rhéologiques en viscoélasticité linéaire peut être observée dans les simulations en DB, en variant les configurations à l'équilibre, les valeurs de la constante de rigidité et le nombre de barres constituant le modèle. Dans le cas d'un modèle à deux barres, les réponses dynamiques d'un système en libre rotation, en rotation non-libre rectiligne (à l'équilibre) et en flexion non-libre non-rectiligne (à l'équilibre) sont comparées dans la Fig. B.7. On constate l'apparition de nouveaux processus de relaxation aux fréquences intermédiaires quand la constante de rigidité est plus importante que le coefficient thermique ($K_b > k_BT$). Par ailleurs, on observe que l'évolution du module de conservation varie de façon substantielle en fonction de la fréquence selon que la configuration est rectiligne, ou pas, à l'équilibre. Ce comportement est cohérent avec la relaxation de l'énergie interne de flexion dans les simulations en régime transitoire après l'application d'un échelon de cisaillement (voir Fig. B.8).

Les simulations en DB ont montré que la fréquence caractéristique, à laquelle l'élasticité intermédiaire est activée, augmente avec l'augmentation de la constante de rigidité. D'autre part, l'intensité de l'élasticité activée et l'intervalle de fréquences associé varient aussi de façon directe avec la constante de rigidité. Ces réponses dynamiques sont cohérentes avec les résultats en relaxation qui montrent une augmentation de l'énergie stockée avec l'augmentation de la constante de rigidité, pendant l'échelon de cisaillement.

Finalement, nous avons trouvé que le nombre de barres dans le modèle (qui dépend de la flexibilité et de la densité linéaire de défauts dans la structure du SWNT) modifie significativement la réponse dynamique du système, notamment le module de conservation. Pour un nombre plus important de barres, un incrément plus important de G' et une pente supérieure de G' en fonction de la fréquence sont obtenus. Une comparaison, en échelle adimensionnelle, entre les données expérimentales et une prédiction par DB (modèle à 5 barres avec configuration non-rectiligne à l'équilibre), est présentée dans la Fig. B.9.

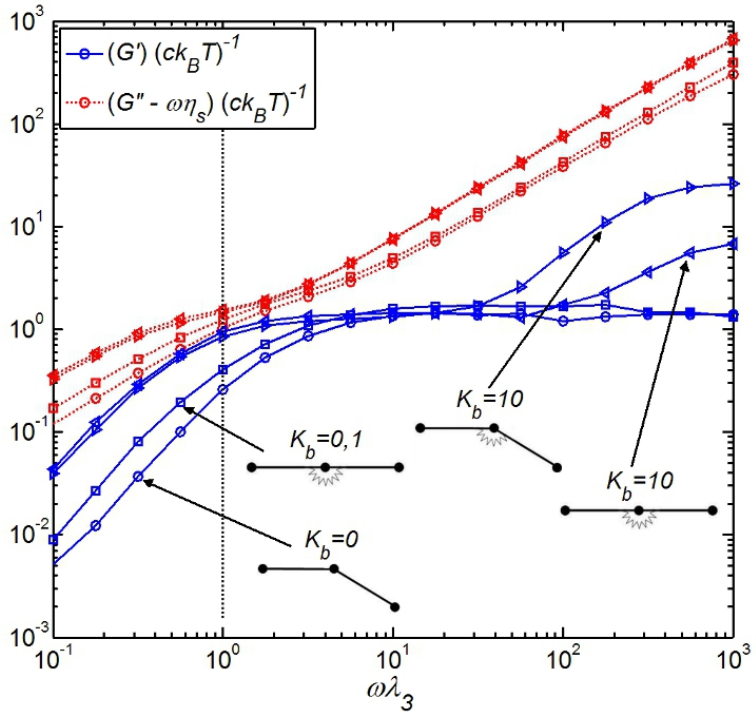

Figure B.7: Prédictions en DB du module de conservation et de perte en fonction de la fréquence pour des systèmes à deux barres : en flexion libre, en flexion non libre rectiligne ($K_b = 0.1$ et $K_b = 10$) et en flexion non libre non rectiligne ($K_b = 10$). Paramètres en DB : $k_BT = 0.1$, $\zeta = 1$, $a = 1$, $c = 1$, $\gamma_0 = 1$

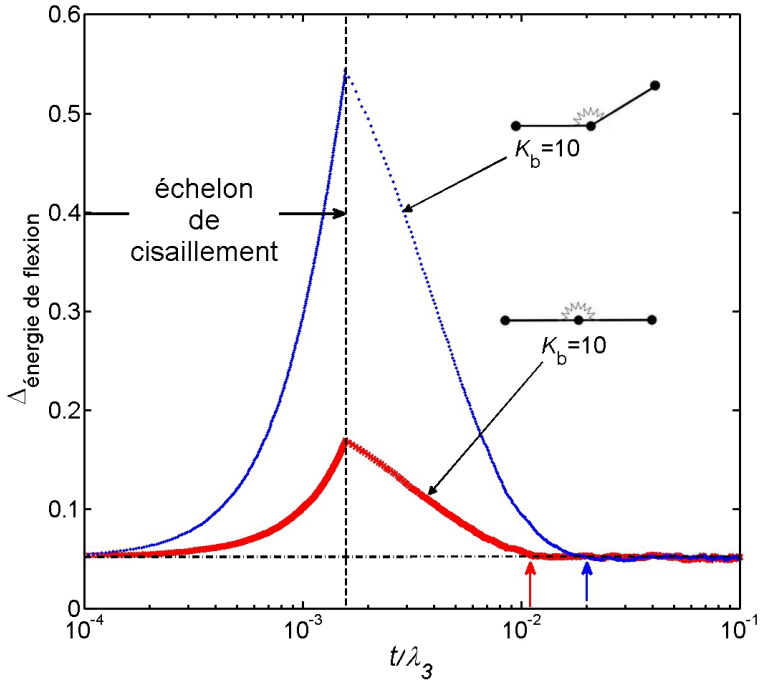

Figure B.8: Prédiction en DB de l'évolution de l'énergie interne de flexion lors d'un essai de relaxation par application d'un échelon de cisaillement sur des systèmes à deux barres en flexion non-libre ($K_b = 10$) avec deux configurations à l'équilibre: droite et non-rectiligne

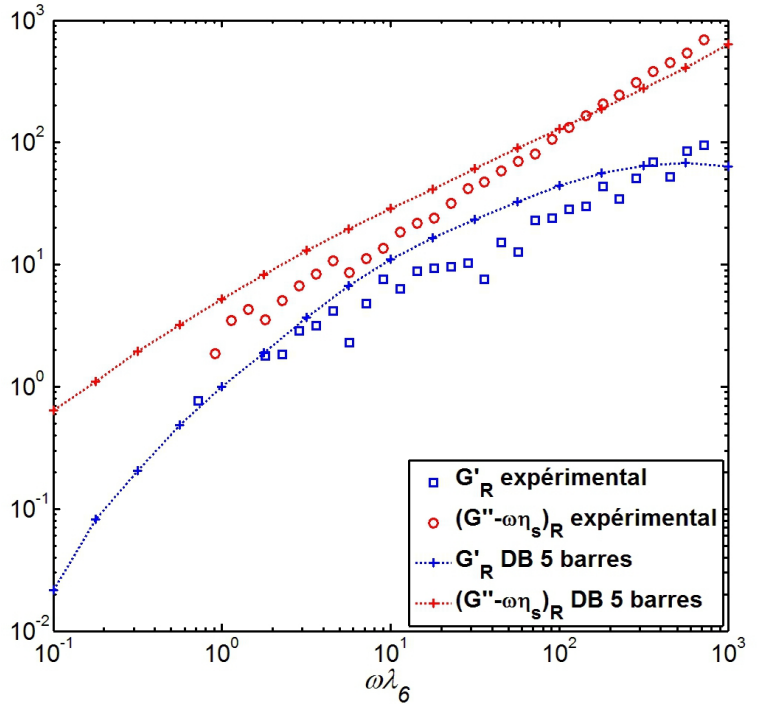

Figure B.9: Comparaison entre la réponse dynamique expérimentale (0.2 wt.% SWNT) et celle prédite par DB pour un système à 5 barres en configuration non-rectiligne à l'équilibre

B.5 Conclusion

Des algorithmes en DB pour la simulation des essais en viscoélasticité linéaire en mode dynamique (déformation oscillatoire en petites déformations) et en mode de relaxation (après un échelon de cisaillement) ont été développés. L'approche par DB en viscoélasticité linéaire a été validée pour les modèles bille-ressort en comparant les résultats aux solutions analytiques du modèle de Rouse (chaîne bille-ressort de Hooke en l'absence d'interaction hydrodynamique) et du modèle de Zimm (chaîne bille-ressort de Hooke avec interaction hydrodynamique moyennée à l'équilibre), en implémentant un schéma d'intégration explicite et l'expression de Kramers pour le calcul du tenseur de contraintes. D'autre part, la simulation de DB en viscoélasticité linéaire pour les modèles bille-barre a été validée en prenant comme référence la solution numériquement exacte de Hassager pour l'équation constitutive du système (trois-billes) (deux-barres) en flexion libre ; l'implémentation numérique est basé sur un schéma d'intégration explicite de premier ordre et l'expression de Kramers-Kirkwood couplée avec l'algorithme de « longue durée » des forces Browniennes pour l'estimation du tenseur de contraintes.

Les SWNT fonctionnalisés ont été modélisés par des filaments semi-flexibles ayant une configuration courbée à l'équilibre ; en considérant l'existence naturelle de défauts topologiques sur les parois graphitiques d'un NTC. Le modèle continu semi-flexible a été discrétisé en un système multi-bille-barre en flexion non-libre avec une configuration non-droite à l'équilibre ayant pour but de simuler la réponse en viscoélasticité linéaire de leurs suspensions diluées dans un solvant Newtonien en utilisant l'approche validée en DB. Dans ce modèle micromécanique imitant la structure d'un SWNT, le nombre de barres constitutifs est supposé être relié directement à la longueur de persistance en conditions d'écoulement ainsi qu'à la densité linéaire de défauts topologiques dans la structure d'un NTC. En termes d'implémentation numérique de ce modèle particulier dans l'approche en DB, une redéfinition mécaniquement cohérente du potentiel de flexion discrète fut nécessaire afin de tenir compte des cas de configurations non-droites à l'équilibre. Un algorithme par décomposition du modèle multi bille-barre en sous-sections (trois-billes) (deux-barres) a été développé dans le but de calculer les forces provenant du potentiel interne de flexion.

A partir de la simulation en DB des essais en viscoélasticité linéaire, des différences non-négligeables dans les réponses rhéologiques ont été identifiées entre les modèles droits et non-droits à l'équilibre. Ce résultat a prouvé que les défauts à l'intérieur de la structure d'un NTC jouent un rôle très important dans leur comportement dynamique en solution diluée. En conséquence, les effets de la présence de défauts topologiques des NTC devront être considérés dans tous les scénarios de modélisation mécanique.

De nouveaux processus de relaxation dans la réponse dynamique des systèmes naturellement non-droits ont été observés lors des simulations en DB des essais de cisaillement oscillatoire en petites déformations. Ces processus sont caractérisés par l'activation d'une élasticité modérée à des fréquences intermédiaires (révélée par une augmentation du mo-

dule de conservation). Le taux d'augmentation du module de conservation et l'intervalle de fréquences associés avec ces nouveaux processus de relaxation sont trouvés dépendants de la constante de rigidité du potentiel de flexion ou, en d'autres termes, de la rigidité structurale des instabilités courbées dans le SWNT. De plus, la réponse dynamique du système multi bille-barre en flexion non-libre dépend de la longueur de persistance en conditions d'écoulement (c'est-à-dire, du nombre de barres dans le modèle). L'augmentation de la pente du module de conservation dans l'intervalle de fréquences intermédiaires est remarquée lorsque le nombre de barres constitutives augmente aussi. La comparaison avec les données expérimentales pour suspensions diluées de SWNT fonctionnalisés dans une résine époxy a montré que les amplitudes et les tendances prédites des modules de conservation et de perte sont cohérentes.

Les réponses rhéologiques en relaxation, données par les simulations en DB des essais de relaxation après un échelon de cisaillement, sont cohérentes avec les résultats de simulations en mode dynamique. Face à cette convergence des résultats de simulation, la cohérence du modèle physique multi bille-barre en flexion non-libre avec une configuration non-droite à l'équilibre a été vérifiée dans le cadre de viscoélasticité linéaire. Dans toutes les simulations réalisées en mode transitoire, une relaxation instantanée de la contrainte de cisaillement a été observée à la fin de l'échelon de cisaillement. Cette réponse du type visqueux est en phase avec la viscosité limite non-nulle trouvée dans la réponse dynamique aux hautes fréquences de sollicitation. Les évolutions de l'énergie interne de flexion pendant les simulations des essais de relaxation sont cohérentes avec les processus de relaxation observés dans les réponses dynamiques à des fréquences intermédiaires. Une augmentation de la constante du potentiel de flexion est traduite par une augmentation de l'énergie interne de flexion lors de l'application de l'échelon de cisaillement, un résultat qui est en phase avec l'augmentation du module de conservation à des fréquences intermédiaires. Par ailleurs, le temps de relaxation de l'énergie stockée pendant l'application de l'échelon de cisaillement diminue lorsque la constante du potentiel de flexion augmente. Ce dernier résultat est cohérent avec les simulations en DB des essais dynamiques, dans lesquelles la fréquence de sollicitation requise pour activer le nouvel apport élastique augmente lorsque la constante du potentiel de flexion augmente aussi. Finalement, les essais expérimentaux de relaxation sur des suspensions diluées et semi-diluées de SWNT fonctionnalisés dans une résine époxy montrent une relaxation quasi-instantanée ; un comportement prédit effectivement par les simulations en DB pour les suspensions diluées de systèmes multi bille-barre en flexion non-libre avec une configuration non-droite à l'équilibre.

Les résultats de rhéologie numérique obtenus dans cette thèse sont très utiles pour enrichir les bases physiques expliquant l'impressionnant effet de renforcement apporté par les NTC dans le comportement rhéologique de leurs suspensions diluées, semi-diluées et, même encore, concentrées.

Le modèle physique proposé pour simuler la réponse mécanique d'un SWNT en solution diluée peut être utilisé dans le cadre de simulations en régime non-linéaire ou en solution semi-diluée, mais il sera probablement nécessaire de considérer les interactions

intra et inter-tubes, qui peuvent être introduites au travers de l'hypothèse d'interaction hydrodynamique (comme dans le cadre de théorie cinétique de polymères) couplée avec une approche de simulation en DB adaptée. L'analyse de ce modèle étendu constitue une perspective de cette recherche.

L'amélioration du modèle actuel passe par une expression plus raffinée du potentiel de flexion, des populations poly-dispersées en longueurs de NTC, des matrices non-Newtoniennes, ainsi que par des descriptions plus réelles des défauts topologiques dans la structure d'un NTC et des effets d'agrégation dans le cadre de NTC non fonctionnalisés.

En termes de rhéologie expérimentale en phase avec les approches de modélisation, le travail futur devra être dirigé vers l'identification des paramètres physiques dans le modèle et la validation des données en viscoélasticité linéaire dynamique dans le régime des hautes fréquences de sollicitation.

MODELLING OF RHEOLOGICAL PROPERTIES OF CARBON NANOTUBE SUSPENSIONS

ABSTRACT: Single-walled carbon nanotubes (SWNTs) are frequently diluted in solvents with the aim of purify, functionalize and transform them. Control and optimization of those processes in liquid phase require a deep understanding of the rheology of SWNT suspensions. However, there is no consensus about the physical origin of some rheological signatures exhibited by the SWNT suspensions. This thesis is intended to elucidate this question by modelling the linear viscoelastic behaviour of SWNT dilute suspensions by using a Brownian Dynamics (BD) approach. Individual treated SWNT are modelled as semi-flexible filaments with a naturally curved structure due to the existence of side-wall defects. Continuous semi-flexible filament model is discretized as a non-freely jointed multi-bead-rod system with a non-straight configuration at equilibrium. A mechanical coherent re-definition of the discrete bending potential is proposed in order to tackle the naturally bent configurations. The linear viscolastic response of the SWNT-coarse-grained model in dilute suspension is BD-simulated under dynamic and relaxation functions. New relaxation processes, characterised by the activation of a mild elasticity at intermediate frequencies, are observed in the dynamic test mode. On the other hand, a quasi-instantaneous shear-modulus relaxation is obtained after the application of a shear-strain step. Bending-energy relaxation spectra are consistent with the range of dynamic responses proving the consistence of the model in the linear viscoelastic regime. The non-negligeble differences found with respect to the rheological behaviour of naturally straight systems demonstrates that the bending flexibility coupled with the presence of structural bent defects plays an important role on the dynamics of individual SWNTs in suspension.

Keywords: carbon nanotubes, topological defects, suspension rheology, linear viscoelasticity, Brownian Dynamics, semi-flexible filament

MODELISATION DES PROPRIETES RHEOLOGIQUES DES SUSPENSIONS DE NANOTUBES DE CARBONE

RESUME : Les nanotubes de carbone mono-paroi (*SWNT*) sont souvent dilués dans un solvant afin de les purifier, les fonctionnaliser ou les transformer. Le contrôle de ces processus requiert une compréhension profonde de la rhéologie de leurs suspensions. Cependant, les bases physiques de leur comportement rhéologique ne sont pas absolument claires. Cette thèse a permis d'apporter des réponses au travers de la modélisation de la viscoélasticité linéaire des suspensions diluées de *SWNT*s en utilisant une approche par la Dynamique Brownienne (DB). Les *SWNT*s sont modélisés par des filaments semi-flexibles dont la configuration est naturellement courbée due à la présence de défauts structuraux. Le modèle continu de filament semi-flexible est discrétisé en un système multibarre en flexion non-libre ayant une configuration non-droite à l'équilibre. Une redéfinition du potentiel de flexion est effectuée afin de prendre en compte les cas des configurations non-rectilignes. Le comportement en viscoélasticité linéaire de leurs suspensions diluées a été modélisé par DB en mode dynamique et de relaxation. Des nouveaux processus de relaxation caractérisés par l'activation d'une élasticité à fréquences intermédiaires sont constatés en dynamique. D'autre part, une relaxation quasi-instantanée du module de relaxation est obtenue lors de l'application d'un échelon de cisaillement. Les spectres de relaxation de l'énergie de flexion sont en accord avec les réponses dynamiques, ce qui prouve la cohérence du modèle en viscoélasticité linéaire. Les différences non négligeables par rapport au comportement rhéologique des systèmes multibarre droits à l'équilibre démontrent que la flexibilité couplée avec la présence de défauts structuraux de courbure joue un rôle important dans la dynamique d'un *SWNT* en suspension.

Mot clés : nanotubes de carbone, défauts topologiques, rhéologie des suspensions, viscoélasticité linéaire, Dynamique Brownienne, filament semi-flexible

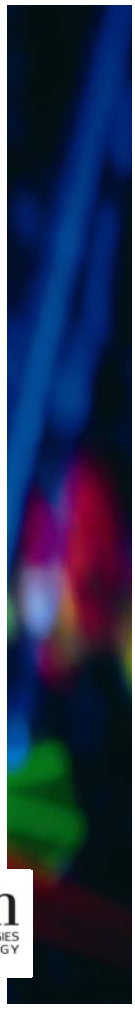

ARTS ET MÉTIERS ParisTech

ParisTech
INSTITUT DES SCIENCES ET TECHNOLOGIES
PARIS INSTITUTE OF TECHNOLOGY